Transverse Schottky Spectra and Beam Transfer Functions of Coasting Ion Beams with Space Charge

Vom Fachbereich Elektrotechnik und Informationstechnik
der Technischen Universität Darmstadt
zur Erlangung des akademischen Grades eines
Doktor rerum naturalium (Dr. rer. nat.) genehmigte

Dissertation

von

Dipl.-Phys. Stefan Paret

geboren am 30. Mai 1980 in Darmstadt

Referent:	Prof. Dr.-Ing. T. Weiland
1. Korreferent:	Prof. Dr. rer. nat. O. Boine-Frankenheim
2. Korreferent:	Prof. Dr. rer. nat. N. A. Pietralla

Datum der Einreichung: 08.12.2009
Datum der Verteidigung: 22.02.2010

D17
Darmstadt 2010

Abstract

A study of the transverse dynamics of coasting ion beams with moderate space charge is presented in this work. From the dispersion relation with linear space charge, an analytic model describing the impact of space charge on transverse beam transfer functions (BTFs) and the stability limits of a beam is derived. The dielectric function obtained in this way is employed to describe the transverse Schottky spectra with linear space charge as well. The difference between the action of space charge and impedances is highlighted.

The setup and the results of an experiment performed in the heavy ion synchrotron SIS-18 at GSI to detect space-charge effects at different beam intensities are explicated. The measured transverse Schottky spectra and BTFs are compared with the linear space-charge model. The stability diagrams constructed from the BTFs are presented. The space-charge parameters evaluated from the Schottky and BTF measurements are compared with estimations based on measured beam parameters.

The impact of collective effects on the Schottky and BTF diagnostics is also investigated through numerical simulations. For this purpose the self-field of beams with linear and non-linear transverse density-distributions is computed on a two-dimensional grid. The noise of the random particle distribution causes fluctuations of the dipole moment of the beam which produce the Schottky spectrum. BTFs are simulated by exciting the beam with transverse kicks. The simulation results are used to verify the space-charge model.

Zusammenfassung

Im Rahmen dieser Arbeit wird die transversale Dynamik gleichförmiger Ionenstrahlen mit moderater Raumladung untersucht. Ausgehend von der Dispersionsrelation mit linearer Raumladung wird ein analytisches Modell zur Beschreibung der Wirkung der Raumladung auf transversale Strahl-Transferfunktionen (nach der engl. Abk.: BTFs) und die Stabilitätsgrenzen des Strahls entwickelt. Die dabei verwendete dielektrische Funktion wird auch eingesetzt, um transversale Schottkyspektren mit linearer Raumladung zu beschreiben. Der Unterschied zwischen der Wirkung von Raumladung und Impedanzen auf den Strahl wird hervorgehoben.

Der Aufbau und die Ergebnisse eines Experiments, durchgeführt im Schwerionensynchrotron SIS-18 bei der GSI zum Nachweis von Raumladungseffekten bei unterschiedlichen Strahlintensitäten, werden erläutert. Die gemessenen transversalen Schottkyspektren und BTFs werden mit dem linearen Raumladungsmodell verglichen. Stabilitätsdiagramme, die mit Hilfe der BTFs konstruiert wurden, werden gezeigt.

Der Einfluss kollektiver Effekte auf die Schottky- und BTF-Diagnose wird darüber hinaus in numerischen Simulationen untersucht. Zu diesem Zweck wird das Eigenfeld von Strahlen mit konstanter und nichtlinearer transversaler Teilchendichte auf einem zweidimensionalen Gitter berechnet. Das Rauschen der zufallsverteilten Teilchen verursacht Fluktuationen des Dipolmoments des Strahls welches das Schottkyspektrum erzeugt. Durch die Anregung des Strahls mit transversalen Kicks wird die BTF simuliert. Mit Hilfe der Simulationsergebnisse wird das Raumladungsmodell verifiziert.

Contents

List of Figures

List of Tables

Chapter 1

Introduction

Charged particle accelerators have been used as a versatile tool for fundamental and applied science during the past decades. Particle beams have been utilized to induce nuclear reactions, to produce exotic nuclei, elementary particles or extreme dense and hot plasmas, to investigate material properties, and even for medical applications. The performance of accelerators has increased by orders of magnitude measured, for instance, by beam energy or intensity [1, 2] since the development of the first proton accelerator of Cockroft and Walton in 1932 [3]. However, the demand of the scientific community for better beams has not ceased to grow. Further advances in the mentioned fields of research rely on a supply of beams with unprecedented intensity and quality.

GSI is a research facility providing beams from light to heavy ions for experiments in various research areas. Here the preparation for the construction of the **F**acility for **A**ntiproton and **I**on **R**easearch (FAIR) has started with the goal to match the needs of the scientific community. The increase of the beam intensity and quality has to cope with many technological and physical challenges concerning the planned machines as well as the existing ones. GSI's linear accelerator and the '**S**chwer**i**onen**s**ynchrotron' (heavy ion synchrotron) SIS-18 will serve as boosters for FAIR's new synchrotrons. For this reason, efforts are taken to upgrade the present accelerators for the operation with high-intensity beams.

One limiting factor for the beam intensity are collective effects occurring in beams with a high phase-space density because of the interaction between the particles [4, 5, 6]. The effects originating from the beam's electromagnetic self-field are studied in this work. In the case that the self-field is negligibly influenced by the materials around the beam, the consequences of the interaction between the beam particles and the field is referred to as space-charge effects [7, 4]. The space-charge field depends on the transverse particle distribution, and each particle experiences an individual force depending on its own position with respect to the beam center. Therefore the space-charge force is incoherent. As internal force it does not affect the barycenter of the beam and has no dissipative component.

In an accelerator, however, the beam environment modifies the self-field of a beam. The fields arising from boundary conditions imposed by the material surrounding the beam are modeled by means of (coupling) impedances [5, 4, 6]. Impedances have a

real part, associated with the dissipation of energy, and an imaginary part. In this work only transverse impedances, which deflect the particles, are considered. Dipolar impedances give rise to a coherent force, which can be described by a force acting on the barycenter of the beam. Higher order impedances are related to incoherent forces. These are negligible, though, in space-charge dominated beams. For this reason, only the coherent dipolar component is discussed in this work.

Already in the 1960's the electrical resistivity of the beam pipe was held responsible for transverse beam instabilities and a dispersion relation was applied to calculate stability limits [8]. It was shown that Landau damping, which was predicted by L. D. Landau in the context of plasma physics [9], prevents beam instabilities to a certain extent [5, 4]. The effectiveness of Landau damping turned out to depend on the momentum spread of the beam. Imaginary impedances do not drive transverse instabilities, but suppress Landau damping. They may therefore cause instabilities that would be damped if only the real part was present [10, 5].

Complementary to the theoretical description, measuring techniques were developed to analyze collective effects. One technique is the use of beam transfer functions [11, 5, 10]. The transverse beam transfer function is defined as the ratio of the beam response to its time harmonic excitation. BTFs are furthermore a common tool to probe beam parameters such as the momentum spread.

Picking up the signal of a beam without excitation yields a signal, as well — the Schottky noise, inherent to any current emitted by an incoherent source. This phenomenon was first investigated by W. Schottky in electrical conductors [12]. In a circular accelerator where this noise passes a detector periodically, bands arise in the power spectrum of the beam. These bands are called Schottky bands and also reveal many properties of the beam non-destructively [13]. Impedances deform the Schottky bands in a characteristic way that can be analyzed to detect the impedance [14].

A system to measure beam transfer functions and Schottky spectra was developed for GSI's '**E**xperimentier **S**peicher**r**ing' ESR [15,16]. In ESR beams are cooled to raise their phase-space density [17,18]. As a result, collective effects perturb beams having an intermediate number of particles. The diagnostics was applied to inspect the cooling process, collective effects and the function of a feedback system [19, 20]. A reproduction of the detectors is available for measurements in SIS-18 [21, 22].

The implications of space-charge effects on the coherent beam stability has been paid less attention to than to impedances. At ultra-relativistic particle energies the space-charge effects vanish and consequently they are not of interest in many accelerator facilities. Nevertheless space charge is an issue in hadron accelerators because ions need much more energy and time to be accelerated to ultra-relativistic speeds than electrons. Due to its reactive nature, space charge does not drive coherent instabilities like real impedances do. Space charge is, however, relevant for the beam stability as it has the capability to suppress Landau damping [23,24]. Another effect, which is outside the scope of this work, is the destabilization of the one-particle orbits since space charge may shift the eigenfrequency of the particles onto the frequency of an excitation by field errors [23]. The particle is then excited resonantly and lost.

Space charge is therefore important for the performance of high-intensity accelera-

tors. One approach for the modeling of space charge is predicated on the assumption that the beam cross-section is not altered by a coherent beam oscillation. Then the beam dynamics can be described by the dispersion relation [25]. The dispersion relation can be used for stability predictions based on numerical computations [26] or for further analytical investigations [27]. Also for Schottky measurements in the transverse plane the impact of space charge has been examined theoretically [28, 29].

The results of detailed theoretical studies about space charge are controversial and difficult to verify experimentally. However, in the regime of moderate space charge, i. e. where the non-linear components of the self-field are negligible compared to the first order, the model can be simplified. The linearized space charge is similar to an imaginary impedance and often treated like an impedance in the literature, e. g. in Ref. [5, 30]. Documents discussing the difference between image-current effects and linear space-charge effects, e. g. Ref. [7, 31, 4], do not draw conclusions concerning the consequences for the diagnostics. Experiments targeting at the measurement of space-charge effects are scarcely reported in the literature. For these reasons experiments with space-charge affected beams help improve the understanding of space-charge effects.

On the one hand the sensitivity of beam transfer functions and Schottky spectra opens a diagnostic window to the beam dynamics with collective effects. The advantage of this was taken in this work. On the other hand, these tools can be used to support the operation of accelerators with intense beams only if the influence of collective effects on the signals is understood. This gives another motivation for the measurements performed in this work. In addition to the experiments, simulations were conducted to model space-charge effects free from the assumptions underlying the analytic model on the one side, and from the uncertainties of the beam parameters in measurements on the other side.

This document reports both on measured and simulated Schottky spectra and BTFs with space charge. The simulations include also imaginary impedances. Chap. 2 gives an overview over GSI and the FAIR project. Chap. 3 is dedicated to the description of the transverse beam dynamics, collective effects and the theory of the diagnostic methods used in this work. The equipment for the measurement of the Schottky spectra, the BTFs and beam profiles in SIS-18 are the subjects of Chap. 4. The post-processing of the data is also explained there. In Chap. 5 the results of an experiment for the detection of space-charge effects are presented. The data are compared with the analytic model and a calculation using measured beam parameters. The application of Schottky diagnostics to the measurement of the chromaticity, an important parameter for experiments with coherent beam instabilities, is shown as well. Chap. 6 describes the numerical model used in the simulations. The outcome of the simulations and the comparison with the model follow in Chap. 7. Finally the conclusions of the previous chapters are drawn in Chap. 8.

Chapter 2

GSI and FAIR

The 'GSI Helmholtzzentrum für Schwerionenforschung' (Helmholtz center for heavy ion research; GSI) is a facility for fundamental research with ion beams. It is funded by the Federal Republic of Germany and the state of Hesse. After the foundation in 1969, the **Uni**versal **L**inear **Ac**celerator UNILAC was built to provide ion beams for experiments in nuclear physics. The supplement 'universal' refers to its capability to accelerate ions over a wide range of masses and charges spanning from protons to uranium. Until 1990 SIS-18 and ESR were built to raise the beam energy and phase-space density for new scientific applications [32, 18]. The number 18 indicates the maximal rigidity of the synchrotron in Tm. (The definition of rigidity is given in Eq. 3.5.) In SIS-18 the ions are accelerated to an adjustable energy whose peak value depends on their mass-to-charge ratio. The maximum lies between 1 GeV/u for U^{73+} ions, where u is the unified atomic mass unit, and 4.5 GeV for protons. GSI at its present state is described in Sec. 2.1.

In order to accommodate the demand for higher and higher beam energy and intensity for more advanced physics experiments, the installation of the **F**acility for **A**ntiproton and **I**on **R**esearch (FAIR) is currently being prepared at GSI. FAIR will host two ion synchrotrons, SIS-100 and SIS-300, and several storage rings as well as beam targets [33]. SIS-18 will serve as booster for SIS-100. Therefore FAIR comprehends an upgrade of UNILAC and SIS-18 to ensure that SIS-18 will provide beams with the quality and intensity required by FAIR. The FAIR project is introduced in Sec. 2.2 with the focus on the upgrade program of SIS-18.

2.1 Present state of GSI

A scheme of the accelerators and experiments at GSI is shown Fig. 2.1. On the western side ion sources are available to produce the ions that are accelerated by UNILAC. After UNILAC the beam arrives in the low-energy experimental hall, where it is either used for experiments, among them the production of super-heavy elements [34] and the examination of exotic nuclei in traps [35], or directed into the transfer channel at the end of which it is injected into SIS-18. The injection energy is generally 11.4 MeV/u.

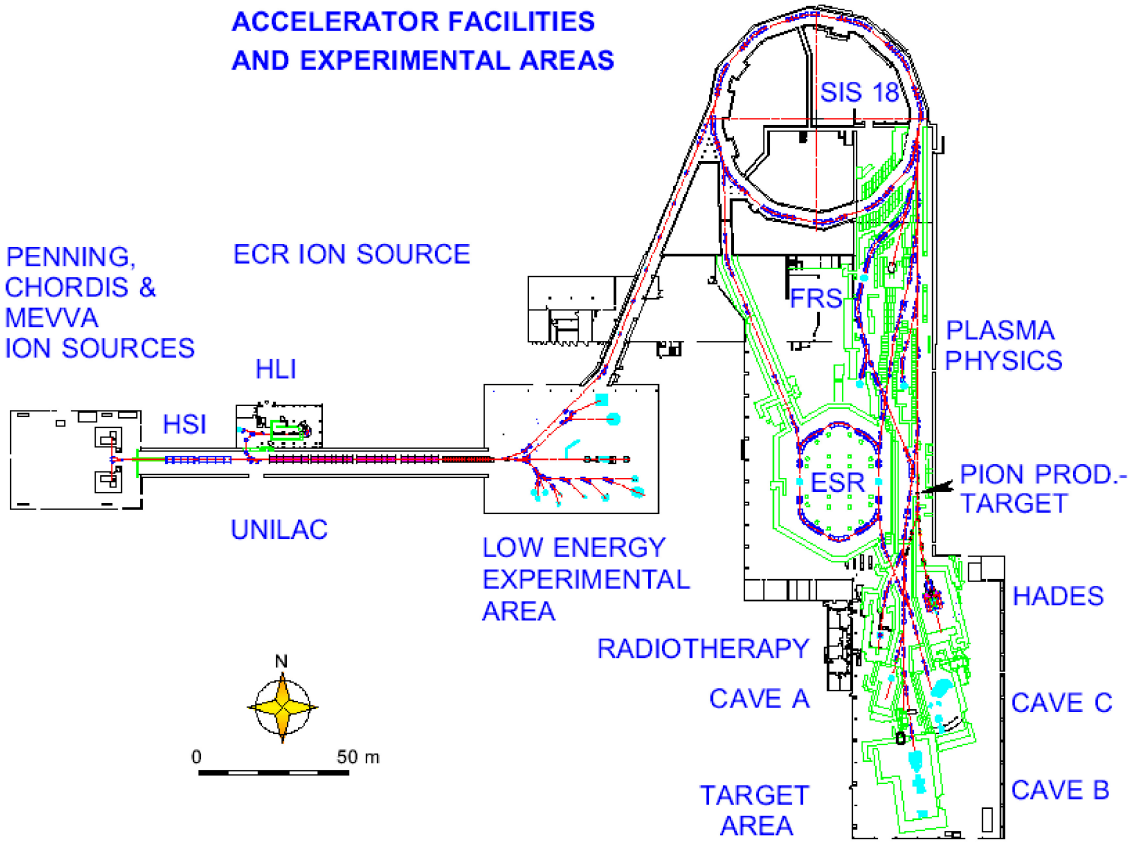

Figure 2.1: Accelerators and experiments at GSI. The ion sources are located to the left side of the figure. Following UNILAC one arrives in the low-energy experimental hall with the transfer channel to SIS-18. After the extraction from SIS-18, the beam is provided to experiments in the fragment separator (FRS), plasma physics, ESR, various scattering experiments (HADES, FOPI) and the radiotherapy.

SIS-18 has a circumference of 216.72 m, consisting of 12 identical lattice sections. The beam optical elements in each cell are two dipoles, three quadrupoles and one sextupole. The maximal field strength of the normal conducting dipoles is 1.8 T. The space between the magnets is occupied by different devices in different sections. Two radio frequency cavities are used for the acceleration. Furthermore, for the beam diagnostics, beam position monitors, current transformers and an ionization profile monitor are present. The technical parameters of SIS-18 can be found in Ref. [36].

In SIS-18 the coasting (dc) beam is captured in four radio frequency buckets and accelerated. For experiments with the beam at injection energy, the bunching and acceleration can be delayed. This was done during the experiments discussed in Chap. 5. An electron cooler is available to decrease the size of the beam and to increase the intensity [37, 38]. The state of the synchrotron after acceleration is called flat top and is followed by the extraction of the beam. The flat top can also be stretched for accelerator experiments.

Table 2.1: Present and future beam intensities in SIS-18.

	present SIS-18			booster operation for FAIR		
Ion	U^{73+}	U^{28+}	Ar^{18+}	U^{73+}	U^{28+}	Ar^{18+}
particles/cycle	$4 \cdot 10^9$	$1 \cdot 10^{10}$	$2 \cdot 10^{10}$	$1.6 \cdot 10^{10}$	$1.4 \cdot 10^{11}$	$5.8 \cdot 10^{11}$
Energy / GeV/u	1	0.2	1.7	1	0.2	1.7

There are two ways to extract the beam. The slow extraction is initialized by shifting the beam on a resonance with the sextupoles. The ions then drift off the closed orbit until they can be pushed out by an electrostatic field. For the fast extraction the beam is kicked off the closed orbit by fast-switching magnets, the so-called kickers, within one turn.

After the extraction, the beam is used for experiments in plasma physics, atomic physics, astrophysics, nuclear physics, material sciences, biophysics and cancer therapy. The goals of the experiments are the investigation of atoms, nuclei, nucleons, elementary particles and the forces acting between them, matter under extreme heat and pressure, and the synthesis of the elements in stars. Numerous articles published in scientific journals witness the productivity of the research at GSI. For recent highlights see e. g. Ref. [39, 40, 41, 42]. An overview over current research activities is given regularly in the annual GSI scientific reports [43].

2.2 FAIR

Two new synchrotrons, SIS-100 and SIS-300, will be built for FAIR to accumulate and accelerate the beams from SIS-18. Their circumference is 1083 m and the rigidity in Tm is indicated by their name. From SIS-100 the beams can be delivered with a maximal energy of 2715 MeV/u for U^{28+} to the experiments or transferred to SIS-300 for further acceleration up to 34 GeV/u for uranium after increasing the charge to 92+ [44]. A large complex of storage rings and targets is attached to the new synchrotrons as Fig. 2.2 displays. The full layout of FAIR is described in Ref. [33]. A brief overview over the system of storage rings is given in Ref. [45].

The energy density of the beams in FAIR gives access to nuclear reactions and extreme matter states that cannot be achieved with SIS-18. The increased particle density furthermore allows the observation of rare events. The possibility to experiment with antiproton beams is completely new. Further advances in the scientific fields addressed by GSI will follow with benefits for quantum chromodynamics, astrophysics and others [46, 47, 48, 49].

All experiments of FAIR get the beam directly or indirectly from SIS-18. Therefore SIS-18 limits the intensity and quality of the beams available for the future experiments. The targeted beam intensities go considerably beyond the values achieved in the past. Hence the upgrade of SIS-18 is an essential part of the FAIR project. The highest beam intensities in SIS-18 accomplished so far [50] and the design intensity for FAIR [33] are listed in Tab. 2.1.

FAIR is optimized for the acceleration of intense uranium beams. In the past

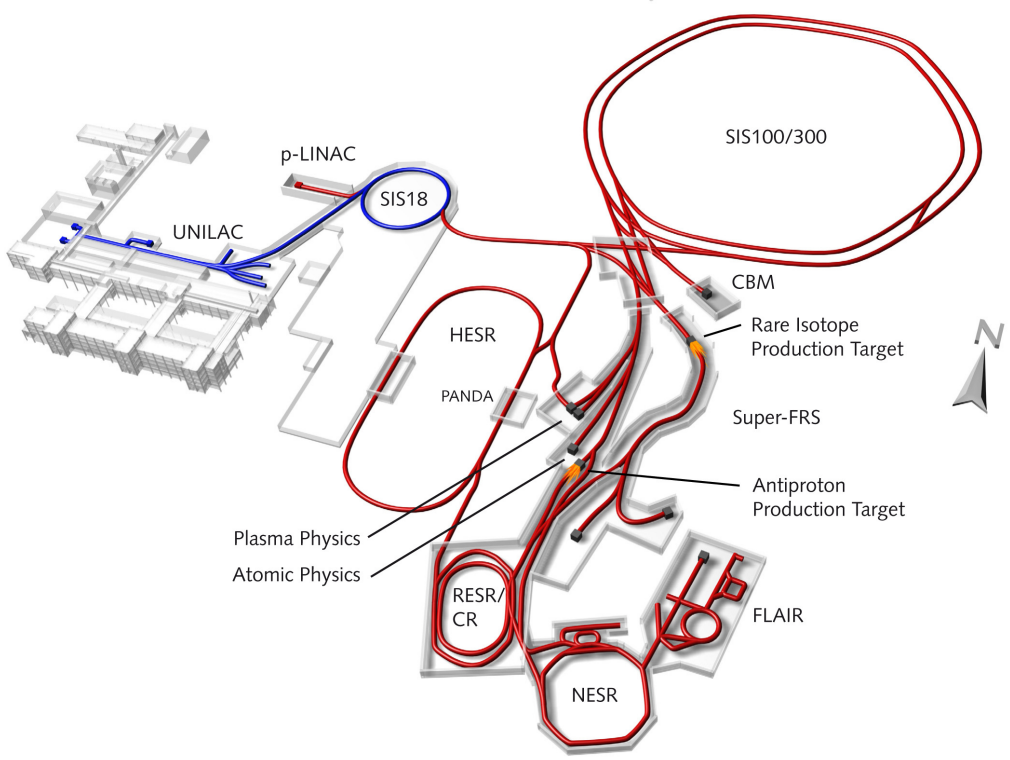

Figure 2.2: Accelerators and experiments of FAIR. The synchrotrons SIS-100 and SIS-300 are shown in the upper right corner, and the experiments below them. To left hand side one sees the present GSI (UNILAC and SIS-18).

U^{73+} ions were used successfully. The electric field of these ions is, however, too strong to concentrate a sufficient number of them in the accelerators. The solution of this problem is the use of a lower charge state, namely U^{28+}. The drawback of this solution is that U^{28+} ions change their charge state easily when colliding with residual gas molecules.

The upgrade program of SIS-18 includes the following technical improvements and investigations:

- For the booster operation, the cycle time of the beam in SIS-18 will be decreased to increase the number of particles extracted per second [45].

- A new radio frequency cavity for the acceleration will be installed to form bunches with a flatter longitudinal density distribution. In this manner the peak current will be reduced [51].

- The vacuum system needs to be improved. Covering the beam pipe with a non-evaporable getter coating reduces the static pressure in the sections between the vacuum pumps [52]. The exchange of the beam pipe in SIS-18 with covered pipes has already partially been done.

- A critical point due to the charge exchange is the dynamic vacuum. Uranium ions with the wrong charge leave their orbit, hit the wall and liberate a large number of molecules (desorption) with the ability to collide with other uranium ions. The increasing gas pressure leads to a beam loss until the beam intensity dropped significantly. Dedicated collimators have been designed and partially installed to catch ions after a charge exchange with little emission of molecules [53].

- U^{28+} ions have a lower charge-to-mass ratio than U^{73+}. Some components of the injection system were exchanged to provide the higher voltages needed to inject the U^{28+} ions at an energy of 11.4 MeV/u into SIS-18 [54]. The accomplishment of this work yielded recently an increase of the beam intensity in SIS-18.

- Deformations of the closed orbit have to be corrected to exploit the full acceptance of SIS-18. Deviations of the actual orbit from the reference reduce the effective aperture [55].

- Due to the self-field of the beam, the incoherent motion of the particles that is stable at low intensity can become unstable at high intensity. Resonances without and with space-charge effects are investigated to find a working point for intense beams [56].

- Collective effects in bunched beams are studied as they play an important role in the damping of longitudinal oscillations [57].

- Intense coasting beams are prone to coherent transverse instabilities. The impact of moderate space charge on the beam stability and diagnostic methods is investigated in this work.

Chapter 3

Transverse beam dynamics

The transverse dynamics of a non-accelerated charged particle beam in a circular accelerator or storage ring is explicated in this chapter. In Sec. 3.1 the motion of an ensemble of non-interacting particles is examined. Starting with a single particle influenced by magnetic fields, the terms describing a particle beam are introduced.

In Sec. 3.2 two diagnostic methods for the examination of the transverse beam dynamics applied in this work are explained. First Schottky noise, the basis of one measuring technique, is reviewed. Then transverse beam transfer functions, the response of a beam to an excitation, are explained. Along the way some insights relevant to the following sections are gained.

The implications of collective effects — phenomena arising due to a large number of particles — on the beam stability and diagnostics are discussed in Sec. 3.3. The interaction of the particles with each other and with the beam environment due to their electromagnetic fields are highlighted with a focus on the stability of the beam. An intrinsic damping mechanism against coherent instabilities based on the momentum spread of the beam is described. A method to assess the limitations of this damping is discussed.

It is shown that Schottky and BTF diagnostics can be used to determine the strength of collective effects in stable beams. An analytic model describing the impact of collective effects at moderate beam intensity is derived. For convenience lists of the symbols and abbreviations used in this work is provided in App. A.

3.1 Transverse beam dynamics at low intensity

The motion of a single particle with constant momentum in an accelerator is examined to prepare the discussion of a beam as a many particle system. The underlying accelerator model is kept as simple as possible. Non-linear effects and some linear effects are neglected. Whenever possible the lattice parameters are even assumed to be constant in the entire accelerator. The horizontal and vertical motion are assumed to be independent of each other since the lattice of accelerators is generally designed to have no transverse coupling in first order.

The terms characterizing the motion of a particle are then applied to describe

the transverse dynamics of a particle beam that is distributed uniformly around the circumference of the accelerator. This kind of beam is called *coasting beam*. Important beam parameters are attributed to the distributions of the one-particle parameters. A more detailed discussion of transverse beam dynamics can be found in many textbooks, e. g. Ref. [1, 2, 58] and in the proceedings of the CERN Accelerator School, e. g. Ref. [59, 60].

3.1.1 Single particle dynamics

The motion of a single particle in a synchrotron or a storage ring is analyzed in this subsection. The beam optics defines the *nominal orbit* or *reference orbit* as the trajectory of a virtual ideal particle with the *nominal momentum* $\vec{p}_0$. As the acceleration of beams is not considered in this work, $|\vec{p}_0|$ is constant. The reference orbit considered in this work is closed and plane. Without loss of generality, we assume that the plane of nominal orbit be horizontal. The earth's magnetic field needs not to be taken into account. The *revolution frequency* of the ideal particle is denoted by f_0 or ω_0. Physical frequencies are substituted by the corresponding angular frequencies with $\omega_? = 2\pi f_?$ if this simplifies an expression.

The position of the ideal particle is parameterized by the path length $s(t) = \int |\vec{v}_0| \, \mathrm{d}t$, where the velocity $\vec{v}_0$ determined by $\vec{p}_0$. According to the special theory of relativity, the interrelation between the speed $\vec{v}$ and the momentum $\vec{p}$ of a particle with rest mass $m_p A$ is given by

$$\vec{p} = \gamma m_p A \vec{v}, \tag{3.1}$$

where

$$\gamma \equiv 1/\sqrt{1-\beta^2} \tag{3.2}$$

is the Lorentz factor and $\beta \equiv |\vec{v}|/c$ the velocity divided by the speed of light in vacuum c. Since this work covers ion beams only, the rest mass is split into the proton mass m_p and the mass number A, which is equal to the number of protons and neutrons in the ion.

The motion of a non-ideal particle is expressed by means of a six dimensional, orthogonal Cartesian coordinate system centered on the ideal particle. The vector

$$\vec{r} = \begin{pmatrix} x \\ x' \\ y \\ y' \\ z \\ \Delta p \end{pmatrix} \tag{3.3}$$

represents the deviation of the particle from the ideal one. x, y, z are the coordinates in real space such that z is oriented in parallel to the reference orbit. The unity vectors spanning the coordinate system in real space are denoted by $\vec{e}_x$, $\vec{e}_y$, and $\vec{e}_z$. The velocity is hence $\vec{v}_0 = v_0 \vec{e}_z$, and correspondingly $\vec{p}_0 = p_0 \vec{e}_z$. The direction of z designates the longitudinal direction. z is linked to a delay or an advance in time

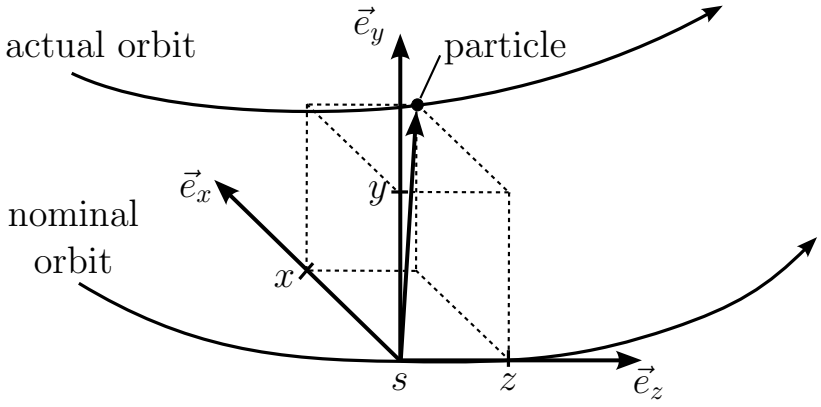

Figure 3.1: Coordinate system parameterizing the position of a particle with respect to the reference particle at s. The coordinate system follows the nominal orbit with the nominal velocity v_0.

$\Delta t = z/v_0$. This is relevant if time-dependent forces, like the radio frequency for acceleration, are active in the ring, but not for the situation considered here. x and y span the so-called *transverse* plane such that x points to the horizontal direction and y to the vertical one. For an illustration see Fig. 3.1.

The longitudinal momentum deviation is normalized by the nominal momentum, i. e. $\Delta p \equiv (p - p_0)/p_0$. A finite momentum perpendicular to p_0 prevents the particle from moving in parallel to the ideal particle. x', defined as $\mathrm{d}x/\,\mathrm{d}s$, and y' correspondingly, express the local slopes of the actual orbit with respect to the reference orbit. The prime $'$ always represents the differentiation with respect to s in this document. In a stable beam, only small momentum deviations occur. Therefore we may assume

$$x', y', \Delta p \ll 1. \tag{3.4}$$

The shape of the reference orbit in synchrotrons is defined by magnetic dipoles. In a homogeneous magnetic field of the flux density $B\vec{e}_y$, our particle moves on a circular trajectory with a radius R. The orbit in a synchrotron, comprising arcs and straight sections, is described by the mean radius $R = C/2\pi$ where C is the path length of one revolution. The product of B and R is called rigidity. It is linked to the particle's charge Ze and p by virtue of

$$BR = \frac{p}{Ze}. \tag{3.5}$$

e is the elementary charge and Z is an integer specifying the number of protons in the ion. Due to Δp our particle moves on an orbit with a slightly different R. The motion on an orbit with a different curvature gives a contribution Δx_R to x. This effect is described by the *dispersion* function $D(s)$ [58].

The dispersion affects also the revolution frequency f_0 of the non-ideal particle as it increases the length of the orbit for $\Delta p > 0$. Besides this effect, we have to consider

the change of the speed and the mass according to Eq. 3.1. For $\beta \ll 1$, the change in speed preponderates so that $\mathrm{d}f_0/\,\mathrm{d}p > 0$, while for $\gamma \gg 1$ we have $\mathrm{d}f_0/\,\mathrm{d}p < 0$. The energy with $\mathrm{d}f_0/\,\mathrm{d}p = 0$ is called transition energy and the corresponding γ is denoted by γ_T. For small momentum deviations, the change of the revolution frequency is expressed by

$$\frac{\Delta f_0}{f_0} = -\eta \Delta p \tag{3.6}$$

and the *slip factor*

$$\eta = 1/\gamma_T^2 - 1/\gamma^2. \tag{3.7}$$

In the following discussion of the transverse motion, the displacement of a particle due to the dispersion is neglected. Within the scope of this approximation, there is no difference between the vertical and horizontal motion. Therefore only the horizontal plane will be discussed explicitly. Unless stated differently, the following equations referring to the horizontal plane can be transfered to the vertical one by exchanging the parameters x by y. In equations without explicit coordinate, the subscripts referring to either plane are omitted.

A synchrotron needs focusing elements to prevent x' and y' from driving the particle away from the reference orbit. The transverse motion with a periodic focusing function $k(s)$ is described by the homogeneous Hill's equation [58]

$$x'' + k_x(s)\, x = 0, \tag{3.8}$$

where the total derivative of x with respect to the time t is expressed in terms of its derivative with respect to s using $\mathrm{d}x/\,\mathrm{d}t = v\ \mathrm{d}x/\,\mathrm{d}s$. The solution can be written as a pseudo-harmonic oscillation

$$x(s) = \sqrt{\epsilon_x \hat{\beta}_x(s)}\cos[\psi_x(s) + \psi_{0,x}], \tag{3.9}$$

where $\hat{\beta}(s)$ is the *amplitude function*, ϵ is an integration constant, and

$$\psi(s) = \int_0^s \frac{\mathrm{d}s}{\hat{\beta}(s)} \tag{3.10}$$

is the phase advance or betatron phase with the initial phase $\psi_{0,x}$. Note that $\psi_{0,y}$ is independent of $\psi_{0,x}$.

From Eq. 3.10, the number of transverse oscillations Q during one revolution can be calculated by virtue of

$$Q = \frac{1}{2\pi} \oint \frac{\mathrm{d}s}{\hat{\beta}(s)}, \tag{3.11}$$

where the path of integration is the reference orbit. Q is called *(betatron) tune* or working point. The mean oscillation frequency

$$f_\beta = Q f_0 \tag{3.12}$$

is the *betatron frequency*.

For the operation of a synchrotron, Q_x and Q_y must be chosen carefully. Setting Q to integers, or halves or thirds of them, would let field errors — present in any machine — excite the particle resonantly. A destabilization of the orbit and particle loss would be the consequences. The same holds for the sum and difference of Q_x and Q_y [60]. However, single-particle instabilities is not dealt with in this work and the lattice is assumed to be perfect.

Magnetic quadrupoles are usually installed in particle accelerators in order to focus the beam. Presuming the quadrupoles are aligned properly, the motions in x and y direction are decoupled. The focusing strength in the horizontal plane is given by

$$k_x = \frac{Ze}{p}\frac{\partial B_y}{\partial x}. \tag{3.13}$$

The horizontal gradient $\partial B_y/\partial x$ is constant for a quadrupolar field. Evaluating k in the vertical plane yields $k_y = -k_x$. This means any quadrupole focuses in one transverse plane and defocuses in the other one. However, net focusing in both planes is achieved by a sequence of quadrupoles with alternating polarity.

The solution of Eq. 3.8 is substantially simplified if k is constant. This usually occurs piecewise in an idealized synchrotron because k is constant within a quadrupole and zero outside. Nonlinear fringe fields at the edges of the quadrupoles can be taken into account to first order by calculating an effective length of a field with the nominal strength k [2]. The fringe fields of dipoles can be approximated as thin lenses by changing x' and y' instantaneously at the edges of the homogeneous field.

The particle motion in a linear lattice can be described efficiently via a matrix algorithm [61, 1, 2]. The initial phase-space vector $\vec{r}(0)$ is transformed to $\vec{r}(s)$ by the multiplication with the *transport matrix* M,

$$\vec{r}(s) = M(0,s) \cdot \vec{r}(0). \tag{3.14}$$

M incorporates the action of the magnetic field along the trajectory. The transport through a beam line is calculated by the multiplication of successive transport matrices.

Since we neglect the particle displacement due to the dispersion, the transverse subspace is decoupled from the longitudinal one. Therefore the horizontal motion is described by a two dimensional sub-matrix

$$\begin{pmatrix} x \\ x' \end{pmatrix} = M_{x,x'}(0,s) \cdot \begin{pmatrix} x_0 \\ x'_0 \end{pmatrix}. \tag{3.15}$$

As it was used in the simulations, we explicitly provide the horizontal transport matrix of a focusing quadrupole given by [2, 1]

$$M_{x,x'}(l) = \begin{pmatrix} \cos(\sqrt{k_x}l) & 1/\sqrt{k_x}\sin(\sqrt{k_x}l) \\ -\sqrt{k_x}(\sin\sqrt{k_x}l) & \cos(\sqrt{k_x}l) \end{pmatrix}. \tag{3.16}$$

l can be the length of the focusing channel or any fraction of it.

In the defocusing plane, where $k<0$, the trigonometric functions in Eq. 3.16 are replaced by the corresponding hyperbolic functions with $k \to |k|$ [58]. The vertical

motion is simply evaluated by replacing x by y and focusing elements by defocusing ones and vice versa in Eq. 3.16.

According to Eq. 3.13, Δp causes a focusing error Δk which in turn leads to an error $\Delta\hat{\beta}$ of the amplitude function introduced in Eq. 3.9. Finally this error propagates into an error of Q (Eq. 3.11), causing a chromatic tune shift

$$\Delta Q_\xi = \xi Q \Delta p. \tag{3.17}$$

The constant ξ is called *chromaticity*. As far as stemming from quadrupoles only, it is called *natural chromaticity* and written as

$$\xi_{nat} = -\frac{1}{4\pi Q} \oint \hat{\beta}(s)\, k(s)\, \mathrm{d}s. \tag{3.18}$$

ΔQ_ξ limits the tolerance of the accelerator for momentum deviations. This is one reason why sextupoles allowing the adjustment of ξ, without changing the linear lattice, are installed in synchrotrons. Assuming $\hat{\beta} \approx$ const within the sextupoles of length l_s, one can assess the chromaticity by virtue of [1]

$$\xi = \xi_{nat} + \frac{1}{4\pi Q} \sum_i \hat{k}_i \hat{\beta}_i D_i, \tag{3.19}$$

where $\hat{\beta}_i$ is the beta function in the i^{th} sextupole and $\hat{k}_i = \partial^2 B_x/\partial x^2\, l_s/(BR)$ is the sextupole strength in $1/\mathrm{m}^2$. D_i, the dispersion function in the sextupole, can not be neglected here. Note that D_i always refers to the horizontal plane in contrast the other parameters in Eq. 3.19. Sextupoles are responsible for higher order aberrations [58], but these are not relevant for this work.

For the following discussion it is useful to describe the evolution of x along the orbit by means of lattice functions. For this purpose we introduce the Courant-Snyder parameters $\hat{\alpha}, \hat{\beta}, \hat{\gamma}$. $\hat{\beta}$ was already defined in Eq. 3.9 as amplitude function. The other two are given by

$$\hat{\alpha}(s) \equiv -\frac{1}{2}\hat{\beta}'(s) \text{ and } \hat{\gamma}(s) \equiv \frac{1+\hat{\alpha}^2(s)}{\hat{\beta}(s)}. \tag{3.20}$$

Using these parameters, we combine Eq. 3.9 and its derivative,

$$x'(s) = -\sqrt{\frac{\epsilon_x}{\hat{\beta}_x}} \{\hat{\alpha_x} \cos[\psi_x(s) + \psi_{0,x}] + \sin[\psi_x(s) + \psi_{0,x}]\}, \tag{3.21}$$

to obtain

$$\epsilon_x = \hat{\gamma}_x(s) x^2(s) + 2\hat{\alpha}_x(s) x(s) x'(s) + \hat{\beta}_x(s) x'^2(s). \tag{3.22}$$

This equation describes an ellipse in the horizontal phase space. The orientation and shape of this ellipse change along the orbit, but its area $\pi\epsilon_x$ remains constant. The quantity ϵ_x is called horizontal *emittance*. It is a measure for the energy in the horizontal motion.

The position of a particle on the ellipse at a fixed point s depends on ψ_x in Eq. 3.9. At every turn the particle passes by on a different position on the ellipse because the

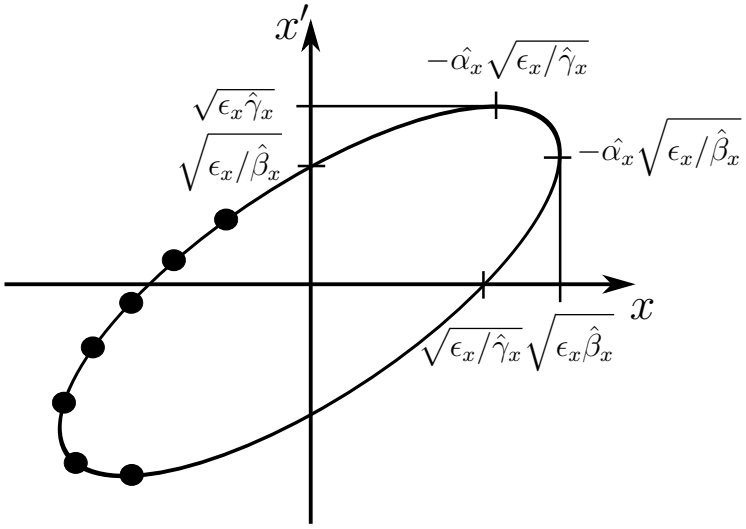

Figure 3.2: Horizontal phase-space ellipse. The black dots mark the position of a particle during subsequent revolutions. Some interesting points are parameterized using the Courant-Snyder parameters.

restrictions to Q enforce ψ_x to change from turn to turn. Hence the stored particle encloses the area of the entire phase-space ellipse as illustrated in Fig. 3.2. The maximal particle offset as a function of s,

$$\hat{x}(s) = \sqrt{\epsilon\hat{\beta}(s)}, \tag{3.23}$$

is called *envelope*. $\hat{x}(s)$ is limited by the local size of the vacuum chamber. The largest emittance fitting into an accelerator is called admittance.

The peculiarities of a certain accelerator lattice are not of interest for the fundamental beam properties discussed in the following subsections. Therefore we replace the lattice functions by their mean values with respect to the circumference of the accelerator. This means that $\hat{\beta} = const$ and, according to Eq. 3.20, $\hat{\alpha} = 0$ and $\hat{\gamma} = 1/\hat{\beta}$. Technically this corresponds to a *constant focusing*. As a result, the betatron oscillation is truly harmonic and Eq. 3.11 yields

$$Q = \frac{R}{\hat{\beta}}. \tag{3.24}$$

Hill's equation (Eq. 3.8) simplifies to

$$x'' + k_x x = 0, \tag{3.25}$$

or equivalently $\ddot{x} + \omega_{\beta,x} x = 0$, where ω_β is the betatron frequency. The solution is

$$x(s) = \sqrt{\epsilon_x\hat{\beta}_x}\,\cos\left(\frac{s}{\hat{\beta}_x} + \psi_0\right), \tag{3.26}$$

where

$$\hat{\beta} = 1/\sqrt{k} \tag{3.27}$$

and $k > 0$. Constant focusing is assumed in the following sections unless stated conversely.

3.1.2 Many particle dynamics

A beam in a synchrotron often consists of a large number of particles with randomly distributed initial phase-space coordinates. A beam is described by means of the statistical distribution of the one-particle coordinates. Generally we assume that the distributions are centered around the corresponding nominal values. As an exception, the beam may have an offset in some of the following subsections. In the horizontal plane, the barycenter of the beam is then located at

$$\bar{x} \equiv \langle x \rangle, \tag{3.28}$$

where the angular brackets $\langle \cdots \rangle$ indicate the averaging over all particles in the beam.

The volume in the six-dimensional phase space that is occupied by all particles divided by π^3 is defined as the *total emittance* of the beam. It is equal to the superposition of all one-particle ellipsoids. The division by π^3 is a convention because the occupied volume is generally well described by an ellipsoid whose the semi-axes are equal to the spread of the phase-space coordinates. The projections of this phase-space ellipsoid into the $x-x'$, $y-y'$ and $z-\Delta p$ subspaces yield the horizontal, vertical and longitudinal emittance, respectively. These two-dimensional projections are conserved individually in first order. The horizontal emittance was already introduced in Eq. 3.22 for one particle.

The total emittance is defined by the particles with the largest one-particle emittances in each plane. However, this definition is often not useful. For unlimited distribution models, like e. g. a Gaussian, the total emittance is not even defined and a limit must be chosen. Often the emittance referring to one or two standard deviations σ of the distribution are considered. The *rms beam size* is given by

$$a = \sqrt{\langle \hat{x}^2 \rangle} = \sqrt{\epsilon \hat{\beta}}, \tag{3.29}$$

where we use Eq. 3.23. In this case ϵ obviously refers to the rms emittance. The abbreviation for root mean square, 'rms', precedes statistical variables referring to the standard deviation of the associated distribution throughout this work.

Beams of different transverse density distributions are frequently compared by considering beams with the same transverse rms emittance, as proposed by the *principle of rms equivalent beams* [62]. In this way, beams with a non-linear profile are approximated by a beam with a constant transverse density. Such a beam is called K-V beam in honor of I. M. Kapchinsky and V. V. Vladimirsky, who first studied its properties [63]. Although K-V beams do not exist in real accelerators, they are a useful approximation in many cases. For the linearization of the space-charge force in Subsec. 3.3.2 we take benefit of this idea.

The beams in this work are always coasting, i. e. except the fluctuations discussed in Sec. 3.2.1, the longitudinal particle-density distribution is constant and the beam

length is equal to the accelerator circumference. The longitudinal emittance of coasting beams is not an interesting quantity. However, the momentum spread plays an important role for collective effects. Thus we define the standard deviation of the momentum distribution, σ_p, as a measure for the momentum spread.

3.2 Theory of transverse beam diagnostics

The operation of an accelerator relies on diagnostic tools telling the state of the beam. Two tools determining important parameters, like f_0, σ_p and Q, are explained in this subsection. In Subsec. 3.2.1 *Schottky measurements*, detecting the electromagnetic radiation constantly emitted by the beam, are explained. Subsec. 3.2.2 discusses how information is gained from *beam transfer functions*, obtained by measuring the response of a beam to a time harmonic excitation.

In this subsection collective effects are neglected. The diagnostics of intense beams is subject of Subsec. 3.3.4 and Subsec. 3.3.5. Technical aspects of the measurements are clarified in Chap. 4.

3.2.1 Schottky noise and diagnostics

In Sec. 3.1.2 beam parameters, such as the momentum distribution σ_p and emittance ϵ, were introduced as quantities characterizing the distributions of the single-particle parameters. However, the underlying distributions are merely models for the mean distribution. The fact that there is a finite number of particles causes random deviations from the mean distributions. These deviations are the so-called *fluctuations*. The fluctuations of a uniform current were first described by W. Schottky [12], hence they are known as *Schottky noise*.

The use of Schottky noise to investigate beam properties is discussed in this subsection. In the following sections we find out that Schottky noise is also relevant for other diagnostic methods and for collective effects. A thorough inspection of fluctuations and Schottky noise can be found in Ref. [14], which served as main reference for this subsection. The fluctuations of different parameters are assumed to be independent of each other.

The beam current detected by an ideal probe in the beam pipe due to a single particle with the index j is given by

$$I_j(t) = 2\pi Z e f_j \sum_{m=-\infty}^{\infty} \delta(\omega_{0,j} t + \theta_j - \theta_p - 2\pi m) \tag{3.30}$$

where f_j is the revolution frequency, θ_j is its random initial phase, θ_p is an additional phase depending on the azimuthal position of the pick-up and $\delta(\cdots)$ is Dirac's delta function. Without loss of generality we assume $\theta_p = 0$ because the signals detected by a Schottky pick-up are independent of the phase. The total current is the sum of

all N_p particles

$$I(t) = \sum_{j}^{N_p} I_j(t). \tag{3.31}$$

Since we consider a coasting beam, the distribution of θ_j is uniform in the interval $[0, 2\pi]$. Expressing the series of δ-functions in terms of the Fourier series expansion,

$$2\pi \sum_{m=-\infty}^{\infty} \delta(\omega_{0,j}t + \theta_j - 2\pi m) = \sum_{m=-\infty}^{\infty} \cos[m(\omega_{0,j}t + \theta_j)], \tag{3.32}$$

and taking the symmetry of the cosine into account , we arrive at

$$I(t) = Ze \sum_{j=1}^{N_p} f_j + 2Ze \sum_{j=1}^{N_p} \sum_{m=1}^{\infty} f_j \cos[m(\omega_{0,j}t + \theta_j)]. \tag{3.33}$$

Now we define the mean current

$$\langle I(t) \rangle \equiv Ze \sum_{j=0}^{N_p} f_j = NZef_0, \tag{3.34}$$

where the angular brackets $\langle \cdots \rangle$ indicate an averaging over the random parameters θ_j and $\omega_{0,j}$ of all particles. The difference $I - \langle I \rangle = \delta I(t)$ is the current fluctuation with $\langle \delta I(t) \rangle = 0$. From Eq. 3.33 we obtain

$$\delta I(t) \equiv 2Ze \sum_{j=1}^{N_p} \sum_{m=1}^{\infty} f_j \cos[m(\omega_{0,j}t + \theta_j)]. \tag{3.35}$$

Equation 3.35 indicates that $\delta I(t)$ is not white noise but has a time structure. This structure manifests itself in the auto-correlation function [14]

$$C_I(t, t') = \langle \delta I(t) \delta I^*(t') \rangle, \tag{3.36}$$

where I^* denotes the complex conjugate of I, if the complex notion is used. Putting Eq. 3.35 into Eq. 3.36 yields in first order

$$C_I(\tau) = 2Z^2 e^2 f_0^2 \sum_{j=1}^{N_p} \sum_{m=1}^{\infty} \cos(m\omega_{0,j}\tau) \tag{3.37a}$$

$$= 2Z^2 e^2 f_0^2 \sum_{j=1}^{N_p} \sum_{m=1}^{\infty} \cos[(1 - \eta\Delta p_j)m\omega_0\tau], \tag{3.37b}$$

where $\tau = t - t'$ and $\omega_{0,j} = \omega_0(1 - \eta\Delta p_j)$. f_j in Eq. 3.35 is approximated by f_0 as Δf_j gives only a second order contribution. Due to the averaging, the random phases, θ_j, disappear.

The spectral power density of the field generated by the current fluctuation, $P_\parallel(\Omega)$, is proportional to the Fourier transform of C_I [14],

$$P_\parallel(\Omega) \propto \int_{-\infty}^{\infty} C_I(\tau)\, \mathrm{e}^{\mathrm{i}\Omega\tau}\, \mathrm{d}\tau = 2\pi Z^2 e^2 f_0^2 \sum_{j=1}^{N_p} \sum_{\substack{m=-\infty \\ \neq 0}}^{\infty} \delta[\Omega + m\omega_0(1-\eta\Delta p_j)]. \tag{3.38}$$

$P_\parallel(\Omega)$ is called *longitudinal Schottky spectrum.* In order to model $P_\parallel$, we normalize Δp_j by σ_p and introduce the parameter

$$\sigma_{m,\omega} = |\eta|\,|m|\omega_0\sigma_p \tag{3.39}$$

to obtain

$$P_\parallel(\Omega) \propto Z^2 f_0 \sum_{j=1}^{N_p} \sum_{\substack{m=-\infty \\ \neq 0}}^{\infty} \frac{1}{|m|}\, \delta\!\left(\frac{\Omega + m\omega_0}{\sigma_{m,\omega}} - \frac{\Delta p_j}{\sigma_p}\right) \tag{3.40}$$

from Eq. 3.38.

Next we introduce an analytic function $\Psi(\Delta p)$ describing the distribution of Δp_j in the beam in a good approximation. If Ψ is normalized such that $\int \Psi(p)\,\mathrm{d}p = 1$, the summation over $\Theta(\Delta p_j)$ with an arbitrary function Θ can be approximated by

$$\sum_{j=1}^{N_p} \Theta(\Delta p_j) \approx N_p \int_{-\infty}^{\infty} \Theta(\Delta p_j)\Psi(\Delta p_j)\ \mathrm{d}(\Delta p_j). \tag{3.41}$$

Using this relation in Eq. 3.40 yields

$$P_\parallel(\Omega) \propto Z^2 f_0 N_p \sum_{\substack{m=-\infty \\ \neq 0}}^{\infty} \frac{1}{|m|}\, \Psi\!\left(\frac{\Omega - m\omega_0}{\sigma_{m,\omega}}\right), \tag{3.42}$$

a series of *longitudinal Schottky bands* defined by

$$P_m(\Omega) \equiv \frac{Z^2 f_0 N_p}{|m|}\, \Psi\!\left(\frac{\Omega - m\omega_0}{\sigma_{m,\omega}}\right). \tag{3.43}$$

The harmonic number m is used to identify the Schottky bands.

For a symmetric distribution $\Psi(\Delta\omega)$, the Schottky bands are centered around $\Omega = m\omega_0$. For convenience we define the frequency of the m^{th} harmonic as

$$f_m \equiv m f_0. \tag{3.44}$$

Thus Schottky diagnostics allows us an accurate measurement of f_0 in a non-destructive way. The rms width of the m^{th} Schottky band is given by $\sigma_{m,\omega}$, defined in Eq. 3.39. As a consequence, the Schottky bands reveal the momentum distribution of the beam. The rms momentum spread is written as

$$\sigma_p = \frac{\sigma_{m,\omega}}{|\eta|\,|m|\omega_0}. \tag{3.45}$$

The amplitude of the Schottky bands decreases with m and the width increases with m, conserving the total power within each band. For this reason, the bands overlap for large m. For the measurement of σ_p, m should be chosen small enough to avoid an overlapping.

Similar to the longitudinal case, the *transverse Schottky spectrum*, originating from the current dipole-moment fluctuations can be deduced. The treatment is, however, more complicated because longitudinal and transverse fluctuations have to be considered jointly. The beam is assumed to pass through the detector center, otherwise additional coherent components would arise [14]. The current dipole-moment then reads

$$d(t) = \sum_{j=1}^{N_p} d_j(t) = \sum_{j=1}^{N_p} x_j(t) I_j(t), \tag{3.46}$$

where

$$x_j(t) = \hat{x}_j \cos(Q_j \omega_{0,j} t + \phi_j) \tag{3.47}$$

is the betatron oscillation of the particle and I_j given by Eq. 3.33. Due to the betatron amplitude, $\hat{x}_j$, and the betatron phase, ϕ_j, the current dipole-moment features two random parameters in addition to θ_j and Δp_j. The latter now affects both $\omega_{0,j}$ and Q_j.

Using Eq. 3.32 and $2\cos\alpha\,\cos\beta = \cos(\alpha+\beta) + \cos(\alpha-\beta)$, Eq. 3.46 can be transformed to

$$d(t) = \frac{Ze}{2} \sum_{j=1}^{N_p} f_j \hat{x}_j \sum_{m=-\infty}^{\infty} \sum_{\pm} \cos[(m \pm Q_j)\omega_{0,j} t \pm \phi_j + m\theta_j]. \tag{3.48}$$

In order to proceed, we define

$$f_m^{\pm} \equiv (m \pm Q_f) f_0, \tag{3.49}$$

where Q_f is the fractional part of Q. For a particle with a momentum deviation Δp_j, it follows from Eq. 3.17 and Eq. 3.6 that

$$\omega_{m,j}^{\pm} \equiv (m \pm Q_j)\omega_{0,j} \approx \omega_m^{\pm} + [m \pm (Q_f - Q\xi/\eta)]\Delta\omega_{0,j} \tag{3.50a}$$

$$= \omega_m^{\pm} + S_m^{\pm} \omega_0 \Delta p_j, \tag{3.50b}$$

where we define

$$S_m^{\pm} \equiv -[\eta m \pm (\eta Q_f - Q\xi)]. \tag{3.51}$$

Eq. 3.48 then writes

$$d(t) = \frac{Ze}{2} \sum_{j=1}^{N_p} f_j \hat{x}_j \sum_{m=-\infty}^{\infty} \sum_{\pm} \cos[(\omega_m^{\pm} + S_m^{\pm}\omega_0 \Delta p_j) t \pm \phi_j + m\theta_j]. \tag{3.52}$$

The mean dipole moment $\langle d(t) \rangle$, obtained by averaging over all random parameters, vanishes identically due to

$$\int_0^{2\pi} \mathrm{d}\phi_j \int_0^{2\pi} \mathrm{d}\theta_j d_j(t) \equiv 0,$$

so that d and its fluctuation are identical, $\delta d(t) \equiv d(t)$. However, the fluctuation can again be detected considering the auto-correlation function [14]

$$C_d(t-t') = \langle d(t)d^*(t')\rangle \tag{3.53a}$$

$$= \frac{e^2Z^2}{8}\langle\hat{x}^2\rangle \sum_{j=1}^{N_p} f_j^2 \sum_{m=-\infty}^{\infty}\sum_{\pm} \cos[(\omega_m^{\pm} + S_m^{\pm}\omega_0\Delta p_j)(t-t')]. \tag{3.53b}$$

Averaging over the phases eliminated ϕ_j and θ_j. $\langle\hat{x}^2\rangle$ is equal to a^2 according to Eq. 3.29. The term f_j^2 can be split into f_0^2 and a second order term that is neglected from here on.

The Fourier transform $\mathcal{F}\{C_d(\tau)\}$, with $\tau = t - t'$, is proportional to the spectral power density of the dipolar fluctuations, or say the *transverse Schottky spectrum*, $P_0^{\pm}$, of a low intensity beam. The Fourier transformation of Eq. 3.53 yields

$$P_0^{\pm}(\Omega) \propto 2\pi Z^2a^2f_0^2 \sum_{j=1}^{N_p}\sum_{m=-\infty}^{\infty}\sum_{\pm} \delta(\Omega - \omega_m^{\pm} - S_m^{\pm}\omega_0\Delta p_j) \tag{3.54a}$$

$$= Z^2a^2f_0 \sum_{j=1}^{N_p}\sum_{m=-\infty}^{\infty}\sum_{\pm} \frac{1}{|S_m^{\pm}|}\,\delta\left(u^{\pm} - \frac{\Delta p_j}{\sigma_p}\right), \tag{3.54b}$$

where

$$u^{\pm}(\Omega) \equiv \frac{\Omega - \omega_m^{\pm}}{\sigma_{m,\omega}^{\pm}} \tag{3.55}$$

is the normalized frequency and

$$\sigma_{m,\omega}^{\pm} \equiv |S_m^{\pm}|\omega_0\sigma_p. \tag{3.56}$$

Now we apply Eq. 3.41 with the momentum distribution Ψ to Eq. 3.54b to obtain

$$P_0^{\pm}(u^{\pm}) \propto Z^2N_pf_0a^2 \sum_{m=-\infty}^{\infty}\sum_{\pm} \frac{1}{|S_m^{\pm}|}\,\Psi(u^{\pm}) \tag{3.57a}$$

$$\equiv \sum_{m=-\infty}^{\infty}\sum_{\pm} P_{0,m}^{\pm}(u^{\pm}), \tag{3.57b}$$

where the $P_{0,m}^{\pm}$ denotes the transverse Schottky bands or Schottky side bands. The upper sign refers to the *upper Schottky side bands*, since they are located at a higher frequency than the longitudinal band corresponding to the same m. Analogously the lower sign refers to the *lower Schottky side bands*.

The amplitude of $P_0^{\pm}$ is proportional to ϵ and $\hat{\beta}$ at the detector according to Eq. 3.29. If Ψ is symmetric then the transverse Schottky bands are centered around $\omega_m^{\pm}$. As the integer part of Q was omitted in the definition of $\omega_m^{\pm}$ (Eq. 3.49), the Schottky side bands appear next to the longitudinal band with the same m. Therefore their positions reveal Q_f. The width of the side bands is given by $\sigma_{m,\omega}^{\pm}$. Hence the

width of the side bands is proportional to the momentum spread. For increasing m the width of the bands increases with $|S_m^{\pm}|$, while the amplitude decreases with that factor. Transverse Schottky bands can also be used to measure ξ. In Subsec. 5.4 two methods to do this are presented.

3.2.2 Transverse beam transfer functions

Schottky diagnostics provides a direct and non-destructive tool to measure various beam and accelerator parameters. A disadvantage is the low signal-to-noise ratio, in particular at low beam intensity. In this case it may be advantageous to measure the ***b**eam **t**ransfer **f**unction* (BTF) of the accelerator. Another primary application of the BTF is the analysis of the beam stability. However, this subject is not discussed until Subsec. 3.3.4 as it requires an understanding of collective effects.

Transverse BTFs are obtained by exciting the beam with a transverse electromagnetic field. A time harmonic signal or white noise can be applied for the excitation, but here only the former is discussed. The beam response is picked up with a Schottky probe. The ratio of the response to the excitation in the frequency domain is defined as BTF. A network analyzer supplies the exciting signal to the kicker and acquires the response signal from the pick-up.

For the following discussion, x is generalized as a complex variable of which the real part is the horizontal coordinate in real space. Applying a time harmonic force with an amplitude F and frequency Ω to a particle turns the equation of motion of a particle in a constant focusing channel (Eq. 3.25) to

$$\ddot{x}_j(t) + \omega_{\beta,j}^2 x_j(t) = \frac{F}{m_p A \gamma}\, \mathrm{e}^{-\mathrm{i}\Omega t}. \tag{3.58}$$

We solve this equation with the ansatz

$$x_j(t) = \hat{x}_j\, \mathrm{e}^{\mathrm{i}(n\theta - \Omega t)}, \tag{3.59}$$

where $\mathrm{e}^{\mathrm{i}n\theta}$ with $n \in \mathbb{Z}$ takes stationary orbit deformations due to a coherent beam excitation into account [5,10]. This ansatz presumes that transient effects have decayed. During the revolution of the particle, the phase changes according to $\theta = \theta_0 + \omega_{0,j} t$. A stationary observer sees an oscillation in time with the frequency Ω, though.

Plugging Eq. 3.59 into Eq. 3.58 yields

$$\hat{x}_j = \frac{F}{m_p A \gamma [\omega_{\beta,j}^2 - (n\omega_{0,j} - \Omega)^2]}, \tag{3.60}$$

where we chose a location with $\theta_j = 0$ so that the phase $\mathrm{e}^{\mathrm{i}n\theta}$ disappears. In order to proceed, we use the approximation

$$\omega_{\beta,j}^2 - (n\omega_{0,j} - \Omega)^2 \approx \mp 2\omega_\beta [\Omega - (n \pm Q_j)\omega_{0,j}], \tag{3.61}$$

which is valid in the vicinity of either of the two distinct poles at $\Omega = (n \pm Q_j)\omega_{0,j}$. For the sake of convenience, we substitute n by m such that

$$\begin{aligned} n + Q &= m + Q_f \qquad \text{for the upper pole, and} \\ n - Q &= m - Q_f \qquad \text{for the lower pole.} \end{aligned} \tag{3.62}$$

Using first Eq. 3.50b and then Eq. 3.55 we rewrite Eq. 3.61 as

$$\omega_{\beta,j}^2 - (n\omega_{0,j} - \Omega)^2 \approx \mp 2\omega_\beta(\Omega - \omega_m^\pm - S_m^\pm \omega_0 \Delta p_j) \tag{3.63a}$$

$$= \mp 2\omega_\beta \sigma_{m,\omega}^\pm \left(u^\pm - \frac{\Delta p_j}{\sigma_p}\right), \tag{3.63b}$$

which is valid for $S_m^\pm > 0$. This expression is put into Eq. 3.60, ending up with

$$\hat{x}_j = \mp \frac{F}{2\omega_\beta \sigma_{m,\omega}^\pm m_p A\gamma(u^\pm - \tilde{p})}, \tag{3.64}$$

where we define

$$\tilde{p} \equiv \Delta p_j/\sigma_p. \tag{3.65}$$

$u^\pm$ is defined in Eq. 3.55.

The response of the beam is obtained by integrating Eq. 3.64 multiplied with the normalized particle distribution $\Phi(\hat{x}_j)\Psi(\tilde{p}_j)$. The distribution of $\hat{x}_j$ and $\tilde{p}_j$ can be factorized because the distributions are uncorrelated. Using $\int_0^\infty \hat{x}_j \Phi(\hat{x}_j)\,\mathrm{d}\hat{x}_j = \hat{x}$, we arrive at

$$\hat{x} = \mp \frac{F}{2\omega_\beta \sigma_{m,\omega}^\pm m_p A\gamma} \int_{-\infty}^{\infty} \frac{\Psi(\tilde{p})\,\mathrm{d}\tilde{p}}{u^\pm - \tilde{p}}. \tag{3.66}$$

The solution of this integral is non-trivial because the integrand possesses a singularity in the integration interval. In order to solve it, a small growth rate $\epsilon_\tau > 0$ of the exciting force, corresponding to an adiabatic growth of the excitation, is introduced [5, 4]. Replacing $\Omega \to \Omega + \mathrm{i}\epsilon_\tau$ in Eq. 3.58 shifts the pole in Eq. 3.66 up by $\mathrm{i}\epsilon_\tau/\sigma_{m,\omega}^\pm$. The integral then is solved along a closed path in the complex plane so that the residue theorem [64] can be applied. The path, visualized in Fig. 3.3 with a solid line, follows the real axis and then a semicircle with radius R_p in the upper complex plane. Solving the path integral piecewise and using the residue theorem, we arrive at

$$\oint \frac{\Psi(\tilde{p})\,\mathrm{d}\tilde{p}}{u^\pm + \mathrm{i}\epsilon' - \tilde{p}} = \int_{-R_p}^{R_p} \frac{\Psi(\tilde{p})\,\mathrm{d}\tilde{p}}{u^\pm + \mathrm{i}\epsilon' - \tilde{p}} + \mathrm{i}\int_0^\pi \frac{\Psi(u^\pm + R_p\,\mathrm{e}^{\mathrm{i}\phi}) R_p\,\mathrm{e}^{\mathrm{i}\phi}\,\mathrm{d}\phi}{\mathrm{i}\epsilon' - R_p\,\mathrm{e}^{\mathrm{i}\phi}} \tag{3.67a}$$

$$= -2\pi\mathrm{i}\Psi(u^\pm + \mathrm{i}\epsilon'). \tag{3.67b}$$

The singularity can also be circumvented by following a semicircle with the radius $\epsilon' = \epsilon_\tau/\sigma_{m,\omega}^\pm$ around the singularity, instead of shifting it. In order to enclose the singularity, the semicircle is placed into the lower complex plane. In Fig. 3.3 the deviation from the former path is indicated with a dashed line. From the piecewise solution and the residue theorem, it follows

$$\oint \frac{\Psi(\tilde{p})\,\mathrm{d}\tilde{p}}{u^\pm - \tilde{p}} = \int_{-R_p}^{u-\epsilon'} \frac{\Psi(\tilde{p})\,\mathrm{d}\tilde{p}}{u^\pm - \tilde{p}} - \mathrm{i}\int_\pi^{2\pi} \Psi(u^\pm + \epsilon'\,\mathrm{e}^{\mathrm{i}\phi})\,\mathrm{d}\phi$$
$$+ \int_{u^\pm+\epsilon'}^{R_p} \frac{\Psi(\tilde{p})\,\mathrm{d}\tilde{p}}{u^\pm - \tilde{p}} - \mathrm{i}\int_0^\pi \Psi(u^\pm + R_p\,\mathrm{e}^{\mathrm{i}\phi})\,\mathrm{d}\phi \tag{3.68a}$$

$$= -2\pi\mathrm{i}\Psi(u^\pm). \tag{3.68b}$$

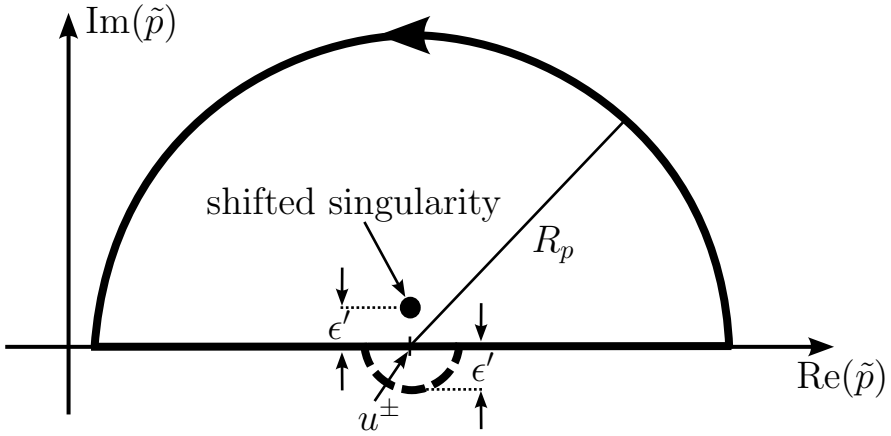

Figure 3.3: Paths for the solution of the dispersion integral applying the residue theorem. $\epsilon' = \epsilon_\tau/\sigma^{\pm}_{m,\omega}$ is the shift of the singularity in one case and the radius of the small semicircle in the other case.

In the limit $\epsilon' \to 0$, Eq. 3.67b and Eq. 3.68b become equal. Hence

$$\int_{-R_p}^{R_p} \frac{\Psi(\tilde{p})\,\mathrm{d}\tilde{p}}{u^{\pm}-\tilde{p}} = P.V. \int_{-R_p}^{R_p} \frac{\Psi(\tilde{p})\,\mathrm{d}\tilde{p}}{u^{\pm}-\tilde{p}} - \mathrm{i}\int_{\pi}^{2\pi} \Psi(u^{\pm})\,\mathrm{d}\phi, \tag{3.69}$$

where *P.V.* stands for Cauchy's principal value of the integral. Taking the limit $R_p \to \infty$ results in the *dispersion integral*

$$r_0(u^{\pm}) \equiv \int_{-\infty}^{\infty} \frac{\Psi(\tilde{p})\,\mathrm{d}\tilde{p}}{u^{\pm}-\tilde{p}} = P.V. \int_{-\infty}^{\infty} \frac{\Psi(\tilde{p})}{u^{\pm}-\tilde{p}}\,\mathrm{d}\tilde{p} - \mathrm{i}\pi\Psi(u^{\pm}). \tag{3.70}$$

Landau was the first to propose this technique to describe frictionless damping in plasmas [9].

With Eq. 3.70 we rewrite Eq. 3.66 as

$$\hat{x} = \mp \frac{F}{2\omega_\beta \sigma^{\pm}_{m,\omega} m_p A \gamma} r_0. \tag{3.71}$$

Now we define the transverse BTF measured at a side band above or below m as

$$r^{\pm}_m(\Omega) \equiv 2\omega_\beta \sigma^{\pm}_{m,\omega} m_p A \gamma \frac{\hat{x}(\Omega)}{F}. \tag{3.72}$$

Applying Eq. 3.70 as well as Eq. 3.71, we have

$$r^{\pm}_{0,m}(u^{\pm}) \equiv \mp \left[P.V. \int_{-\infty}^{\infty} \frac{\Psi(\tilde{p})}{u^{\pm}-\tilde{p}}\,\mathrm{d}\tilde{p} - \mathrm{i}\pi\Psi(u^{\pm}) \right] = \mp r_0(u^{\pm}), \tag{3.73}$$

where the subscript 0 labels a BTF without collective effects.

Eq. 3.73 can be solved analytically for various momentum distributions. Examples are given in Ref. [5]. For a Gaussian distribution,

$$\Psi(\tilde{p}) = \frac{1}{\sqrt{2\pi}}\,\mathrm{e}^{-\tilde{p}^2/2}, \tag{3.74}$$

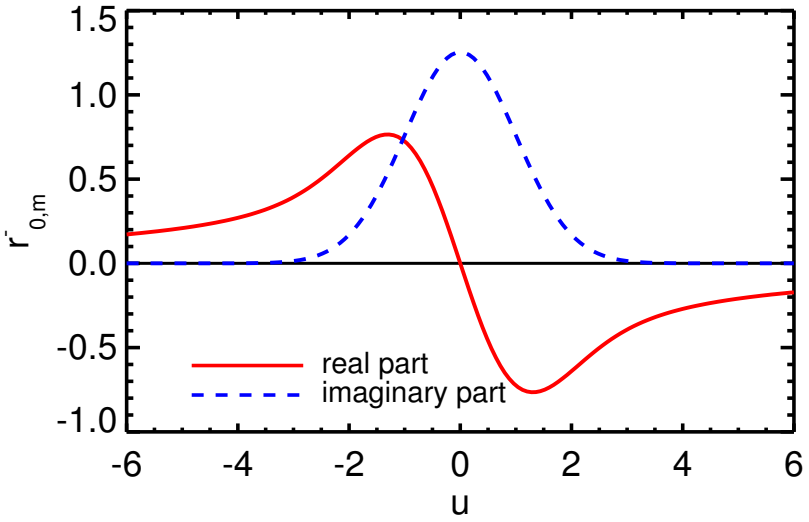

Figure 3.4: Real and the imaginary part of the dispersion integral of a lower side band with a Gaussian momentum distribution (Eq. 3.75). The imaginary part reflects the momentum distribution.

the solution reads [31]

$$r_0(u^{\pm}) = \mathrm{i}\sqrt{\frac{\pi}{2}}\left[1 - \mathrm{erf}\left(\frac{\mathrm{i}u^{\pm}}{\sqrt{2}}\right)\right] \mathrm{e}^{-(u^{\pm})^2/2}, \tag{3.75}$$

which is known as complex error function. The real and imaginary part of Eq. 3.75 are shown in Fig. 3.4.

$r_m^{\pm}$ is observable with a network analyzer, an exciter and a pick-up. Its imaginary part reflects the momentum distribution of the beam. Similar to Schottky diagnostics, σ_p and Q_f can be identified via BTF measurements. The application of BTFs for the analysis of the beam stability is discussed in Subsec. 3.3.4.

3.3 Collective effects

With increasing beam intensity, the electromagnetic self-field of the beam exerts an increasing force on each particle in the beam. This electromagnetic interaction is a subgroup of collective effects in particle beams [6]. The shape of the self-field depends on the distribution of the particles and on the beam environment. Electromagnetic interactions that are present in a beam if its environment is negligible are called space-charge effects. However, particle beams in accelerators are always surrounded by materials which modify the boundary conditions for the self-field. The impact of the beam environment on the field and hence on the beam is described with the concept of impedances. The effects of space charge and impedances on the transverse dynamics of a weakly relativistic beam, such that β cannot be approximated by 1, in a synchrotron was the topic of this work.

In Subsec 3.3.1 dipolar transverse impedances are introduced without going into the details of their evaluation. Space charge is the topic of Subsec. 3.3.2. The commonalities and the differences in the action of impedances and space charge are emphasized. Landau damping, a beam-intrinsic damping-mechanism against coherent instabilities, is examined in Subsec. 3.3.3. In Subsec. 3.3.4 and 3.3.5 the BTF and Schottky theory are revised in order to include impedance and space-charge effects. An analytic model suitable for the comparison with measured or simulated data is derived.

3.3.1 Impedances and coherent tune shift

In an accelerator, the self-field of the beam is influenced by the beam environment. Quantitatively this effect is described with (coupling) impedances. In this work only *dipolar transverse impedances* are considered. These impedances deflect the beam. Higher order impedances, which may for instance focus the beam, are disregarded.

Let $\vec{E}$ be the electric and $\vec{B}$ the magnetic field produced by the interaction of a beam with the current dipole-moment $I\bar{x}$ with the surrounding accelerator components. The field originating from the beam itself is explicitly excluded here; it is the subject of Sec. 3.3.2. The transverse impedance of an accelerator component with the length L is defined by the integral [4, 30]

$$Z_\perp(\Omega) = -\frac{\mathrm{i}}{\beta I \bar{x}} \int_0^L \left[\vec{E}(s,\Omega) + \vec{v} \times \vec{B}(s,\Omega)\right]_\perp \mathrm{d}s. \tag{3.76}$$

The transverse impedance is generally a complex function. The real part or resistive part corresponds to an energy loss in the material, therefore we have [5]

$$\mathrm{Re}[Z_\perp(\Omega > 0)] \geq 0. \tag{3.77}$$

This feature is important for the stability of the beam, as clarified below.

The assessment of impedances is an area of active research at many accelerator facilities. For devices with a complicated geometry, numerical simulations have to be performed. Perhaps the most simple but still useful example of an impedance is that of a perfectly conducting beam pipe. The beam pipe contributes strongly to the total impedance of an accelerator because it surrounds the beam almost along its entire length. For a circular pipe of a perfectly conducting material and of radius b, as sketched in Fig. 3.5, the impedance is [30]

$$Z_\perp^{cw} = -\mathrm{i}\frac{Z_0 R}{\beta^2\gamma^2 b^2}, \tag{3.78}$$

where Z_0 is the characteristic impedance of vacuum. This impedance is purely reactive because the resistivity is neglected. The fact that it is independent of the frequency is a peculiarity of the perfectly conducting beam pipe.

Taking the finite resistivity of the beam pipe into account gives an impedance with a real part, and complicates the evaluation significantly. Approximate expressions

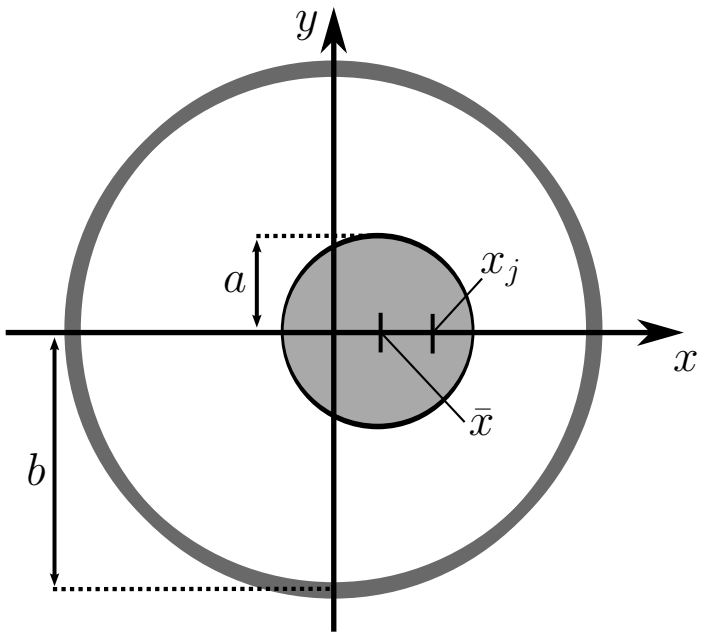

Figure 3.5: Circular beam with a local horizontal offset $\bar{x}$ in a circular beam pipe. b is the radius of the beam pipe and a is the radius of the beam. A test particle is located at x_j.

with different limitations can be found in the literature (e. g. in Ref. [30]). General expressions are derived in Ref. [65]. Fig. 3.6 shows the real part of the resistive wall as a function of the frequency. It decreases monotonically so that it is most dangerous for the lowest modes.

Another impedance of major importance in SIS-18 stems from the 9 kickers installed for the fast extraction of the beam. This impedance is displayed in Fig. 3.6, as well. It was evaluated experimentally as well as with approximate analytical and numerical calculations [66, 67] with comparable results. Several sharp maxima below 20 MHz due to the pulse-forming network of the kicker are observed in the horizontal plane. Above 100 MHz the ferrite material present in the kickers increases the impedance.

In accelerators with intense ion beams, electron clouds can form and interfere with the beam [68]. This effect can be described by an impedance with a maximum close to 20 MHz. However, the investigation of electron clouds in SIS-18 has started only recently [69]. Therefore the electron densities to be expected and the associated impedance are still uncertain.

In order to study the interaction of the beam with the accelerator impedance, we consider a beam stored in a synchrotron. For the time being, the beam is assumed to have no momentum spread. Such a beam is known as a *cold beam* because the particles have little energy in their random motion, similar to the particles in a cold solid body.

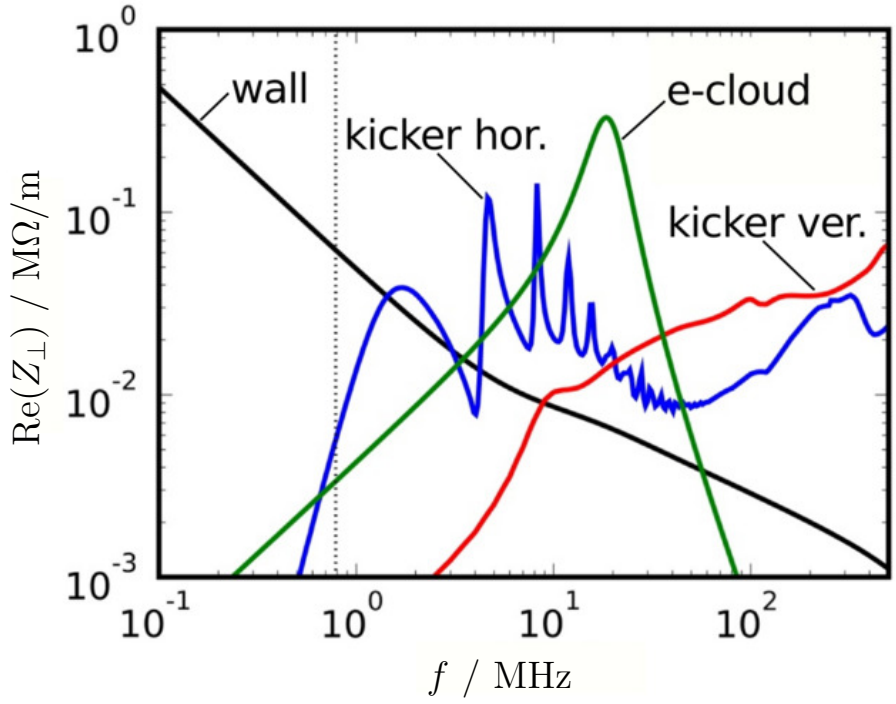

Figure 3.6: Real part of the impedances of the resistive wall, the kickers (horizontal and vertical) and an estimation for the electron cloud, in SIS-18. The dashed line indicates f_0.

(Courtesy O. Boine-Frankenheim)

Choosing $L = 2\pi R$ in Eq. 3.76, we find the mean force experienced by a particle during one revolution

$$F(\Omega) = \mathrm{i}\frac{e^2 Z^2 N_p \beta \omega_0 \bar{x}}{4\pi^2 R} Z_\perp(\Omega). \tag{3.79}$$

Due to the stationary transverse modes, the beam offset along the orbit is given by $\bar{x} = \hat{x}\,\mathrm{e}^{\mathrm{i}n\theta}$. Assuming that the perturbation of the beam causes an oscillation $\mathrm{e}^{-\mathrm{i}\Omega t}$, where Ω is a complex frequency, the equation of motion is stated as

$$\ddot{x}_j(t) + \omega_\beta^2 x_j(t) = 2\omega_\beta \Delta\tilde{\omega}\hat{x}\,\mathrm{e}^{\mathrm{i}(n\theta - \Omega t)}, \tag{3.80}$$

where we define

$$2\omega_\beta \Delta\tilde{\omega} \equiv \mathrm{i}\frac{e^2 Z^2 N_p \beta \omega_0}{4\pi^2 m_p A \gamma} Z_\perp(\Omega). \tag{3.81}$$

The ansatz Eq. 3.59 yields, similarly to Eq. 3.60,

$$\hat{x}_j = \frac{2\omega_\beta \Delta\tilde{\omega}\,\hat{x}}{\omega_{\beta,j}^2 - (n\omega_{0,j} - \Omega)} \tag{3.82a}$$

$$= \mp\frac{\Delta\tilde{\omega}}{\Omega - \omega_m^\pm}\hat{x}, \tag{3.82b}$$

where the external excitation is replaced by Eq. 3.81 and Eq. 3.63a is applied with $\Delta p_j = 0$ because we consider a cold beam. Eq. 3.82b is then multiplied with the normalized $\hat{x}_j$-distribution, $\Phi(\hat{x}_j)$, and integrated with respect to $\hat{x}_j$, as done in Sec. 3.2.2. After division by $\hat{x}$, we find the coherent modes

$$\Omega = \omega_m^{\pm} \mp \Delta\tilde{\omega} \equiv \omega_m^{\pm} \mp \left(\Delta\omega + \frac{\mathrm{i}}{\tau}\right). \tag{3.83}$$

On the right hand side, the complex frequency $\tilde{\omega}$ is decomposed into the real and imaginary part,

$$\Delta\omega \equiv \frac{e^2 Z^2 N_p \omega_0}{8\pi^2 c m_p A Q \gamma} \operatorname{Im}[Z_\perp(\omega_m^{\pm})], \text{ and} \tag{3.84a}$$

$$\frac{1}{\tau} \equiv \frac{e^2 Z^2 N_p \omega_0}{8\pi^2 c m_p A Q \gamma} \operatorname{Re}[Z_\perp(\omega_m^{\pm})]. \tag{3.84b}$$

Obviously imaginary impedances cause a shift of the frequency of the coherent beam oscillation, or say a *coherent tune shift*. For the perfectly conducting beam pipe (Eq. 3.78) one obtains

$$\Delta Q = \frac{r_p Z^2 N_p R}{2\pi A Q \beta^2 \gamma^3 b^2}. \tag{3.85}$$

Real impedances, on the other hand, lead to an exponential growth or damping of the oscillation. From Eq. 3.77 and Eq. 3.84b, it follows that only lower side bands can be excited.

Under the assumptions made so far, an arbitrarily small real impedance would destabilize the beam. Fortunately the momentum spread — unavoidably present in any beam — prevents the beam from responding in a fully coherent way. The damping effect of the momentum spread is clarified in Sec. 3.3.3.

3.3.2 Space charge and incoherent tune shift

Space-charge effects are understood as the result of the interaction between the self-field, i. e. the field originating solely from the particles belonging to the beam, and each particle of the beam, independently of the environment. Since particles with the same charge sign repel each other, the space-charge force is defocusing in both planes. However, the force is suppressed with increasing beam energy due to the Lorentz transformation. This effect can also be interpreted as a consequence of the attractive force between the parallel currents represented by the particles. With rising v_0, the same charge corresponds to a higher current which partially compensates the repulsion. Thus space charge is most important at low energy.

The space-charge force is different for each particle because it depends on the particles' position with respect to the barycenter of the beam. Furthermore, the force depends on the non-linear transverse particle distribution and is consequently non-linear, too. Because of this, a detailed analysis of the space-charge effects becomes

quite involved. However, for the analysis of the data from measurements or simulations, simple models that can be fitted to the data are useful, as long as they reflect the essential features of space charge. Such a model is derived in this subsection.

As a first simplification, we assume that we have a *K-V beam* (introduced in subsection 3.1.2). Such a beam is favorable for the modelling because it features a *linear space-charge force*. This approximation is justified only if the space-charge force is weak enough to neglect the non-linear components.

The second major simplification used here is called *rigid beam assumption*. A beam is said to oscillate rigidly if its cross-section is not altered by the oscillation. Only under this condition the particle density is constant in time or with respect to s.

Let the beam have an offset $\bar{x}$ and a test particle be at x_j, as shown in Fig. 3.5. Applying Maxwell's equations to a homogeneous circular beam yields [7]

$$F_x(\bar{x}, x_j) = \frac{e^2 Z^2 N_p}{2\pi\epsilon_0 \beta^2 \gamma^2 R a_{kv}^2}(x_j - \bar{x}) \equiv 2\omega_\beta \Delta\omega_{sc} \gamma m_p A (x_j - \bar{x}) \tag{3.86}$$

as horizontal Lorentz force with the dielectric constant of vacuum ϵ_0, and the full beam radius a_{kv}. This force incorporates the electrostatic field $\vec{E}$ and the magnetostatic field $\vec{B}$, where $B = v/c^2 E$, because the current density $\vec{J}$ is related to the charge density ρ by $\vec{J} = \vec{v}\rho$. Since all particles move almost in parallel, the force $\vec{F} = eZ(\vec{E} + v\vec{e}_z \times \vec{B})$ simplifies to $\vec{F} = eZ/\gamma^2 \vec{E}$. The corresponding equation of motion is written as

$$\ddot{x}_j(t) + \omega_\beta^2 x_j(t) = 2\omega_\beta \Delta\omega_{sc}[x_j(t) - \bar{x}(t)]. \tag{3.87}$$

Subtracting $2\omega_\beta \Delta\omega_{sc} x_j(t)$ from Eq. 3.87 separates x and x_j. Using the modified betatron frequency

$$\omega_{\beta,sc} \equiv \omega_\beta - \Delta\omega_{sc}, \tag{3.88}$$

$\omega_\beta^2 - 2\omega_\beta \Delta\omega_{sc}$ is then replaced by ω_{sc}^2, which is a good approximation for moderate space charge, i. e. $\Delta\omega_{sc} \ll \omega_\beta$. According to Eq. 3.88, the one-particle betatron frequency is shifted by $\Delta\omega_{sc}$. The corresponding tune shift

$$\Delta Q_{sc} \equiv \frac{\Delta\omega_{sc}}{\omega_0} \tag{3.89}$$

is therefore called *space-charge tune-shift*. The sign of $\Delta\omega_{sc}$ is always the same in both planes. In our notation $\Delta\omega_{sc} > 0$. It is an *incoherent tune shift* because it concerns the individual oscillation of each single particle as opposed to the coherent tune shift referring to the barycenter of the beam.

Coming back to the coasting beam with the stationary coherent modes $\hat{x}\,\mathrm{e}^{\mathrm{i}n\theta}$ and adding a perturbation with the frequency Ω, the equation of motion is

$$\ddot{x}_j(t) + \omega_{\beta,sc}^2 x_j(t) = -2\omega_\beta \Delta\omega_{sc} \hat{x}\,\mathrm{e}^{\mathrm{i}(n\theta - \Omega t)}. \tag{3.90}$$

This equation looks similar to Eq. 3.80 with a reactive impedance. But the important difference is that the eigenfrequency of the one-particle oscillation is modified by space

charge. This means that linear space-charge effects can be modeled like an imaginary impedance after replacing ω_β by $\omega_{\beta,sc}$ in the equation of motion. For convenience we define

$$\omega^{\pm}_{m,sc} \equiv \omega^{\pm}_{m} \mp \Delta\omega_{sc} \tag{3.91}$$

and the normalized frequency (Eq. 3.55) with space charge

$$u^{\pm}_{sc} = \frac{\Omega - \omega^{\pm}_{m,sc}}{\sigma^{\pm}_{m,\omega}}. \tag{3.92}$$

The incoherent tune shift deduced from Eq. 3.86 is given by

$$\Delta Q_{sc} = \frac{r_p Z^2 N_p R}{2\pi A Q \beta^2 \gamma^3 a^2_{kv}}. \tag{3.93}$$

Comparing this result with Eq. 3.85, one finds that ΔQ_{sc} exceeds the tune shift due to image currents by a factor a^2_{kv}/b^2. In the literature the so-called 'space-charge impedance' is defined as the impedance that causes a tune shift according to Eq. 3.93. However, this label is inaccurate because the shift of the incoherent tune due to space charge (Eq. 3.88) is qualitatively different from impedance effects.

In a more general form the horizontal tune shift reads [7]

$$\Delta Q_x = \frac{r_p Z^2 N_p g}{\pi A \beta^2 \gamma^3 B(\epsilon_{kv,x} + \sqrt{\epsilon_{kv,x}\epsilon_{kv,y} Q_x/Q_y})}, \tag{3.94}$$

where $\epsilon_{kv,x}$ and $\epsilon_{kv,y}$ represent the total emittances of a K-V beam, and g and B are form factors depending on the actual particle distribution. Interchanging all x and y yields the vertical tune shift. The bunching factor B provides the ratio of the mean current to the peak current in bunched beams. For coasting beams we have $B = 1$.

If the beam profile is inhomogeneous, then the space-charge force becomes non-linear and the shift of the one-particle tune ΔQ_j depends on the individual betatron amplitude a_j. The beam thus experiences a tune spread in addition to the shift. g is defined such that Eq. 3.94 returns the largest tune shift in a beam with arbitrary transverse profile. For a K-V beam g is 1 and the total emittances are to be inserted. For a Gaussian density distribution, $g = 2$ is to be taken and the total emittances are approximated by the $2\,\sigma$ emittances.

Remembering the restrictions to the value of Q discussed in Subsec. 3.1.1 we see that the tune spread creates a problem. As it smears out the working point even at the optimal setting, a part of the beam may hit a one-particle resonance [6]. However, for coherent beam instabilities the maximal tune shift is less of interest than its mean value. An approximation of the mean tune shift is obtained by applying the principle of rms equivalent beams. Eq. 3.94 is then applied to the K-V beam with equal rms emittance. Note that $\epsilon_{kv} = 4\epsilon$ because $a_{kv} = 2a$ [62].

3.3.3 Landau damping

In Subsec. 3.3.1 it is shown that arbitrarily small, real impedances destabilize a beam without momentum spread. The benefit of the omnipresent momentum spread in any

real beam for the beam stability is elaborated in this section. The stability limit of a coasting beam with given momentum distribution is derived.

The equation of motion of a particle under the influence of an impedance and space charge, obtained by combining Eq. 3.80 and Eq. 3.87, reads

$$\ddot{x}_j + \omega^2_{\beta,sc,j} x_j = 2\omega_\beta(\Delta\tilde{\omega} - \Delta\omega_{sc})\hat{x}\,\mathrm{e}^{\mathrm{i}(n\theta - \Omega t)}. \tag{3.95}$$

The solution, found by following the procedure presented in Sec. 3.2.2, is the *dispersion relation*

$$1 = \mp\frac{\Delta\tilde{\omega} - \Delta\omega_{sc}}{\sigma^\pm_{m,\omega}} r_0(u^\pm_{sc}) \tag{3.96a}$$

$$= \mp(\Delta U^\pm - \Delta U^\pm_{sc} + \mathrm{i}\Delta V^\pm)\, r_0(u^\pm_{sc}). \tag{3.96b}$$

The first line is the analogon to Eq. 3.71 after division by $\hat{x}$ and the replacement $F/(m_p A\gamma) \to 2\omega_\beta(\Delta\tilde{\omega} - \Delta\omega_{sc})\hat{x}$. In the second line we introduced the parameters

$$\Delta U^\pm_{sc} \equiv \frac{\Delta\omega_{sc}}{\sigma^\pm_{m,\omega}}, \tag{3.97a}$$

$$\Delta U^\pm \equiv \frac{\mathrm{Im}(\Delta\tilde{\omega})}{\sigma^\pm_{m,\omega}}, \quad \text{and} \tag{3.97b}$$

$$\Delta V^\pm \equiv \frac{\mathrm{Re}(\Delta\tilde{\omega})}{\sigma^\pm_{m,\omega}} \tag{3.97c}$$

as quantities expressing the effectiveness of collective effects. $\Delta U^\pm_{sc}$ is called *space-charge parameter*. These parameters correspond to the tune shift due to collective effects normalized with the frequency spread of the associated mode.

Despite the case without momentum spread, it is generally infeasible to resolve Eq. 3.96b analytically with respect to the eigenmodes Ω. Instead it is common to plot $1/r_0(u^\pm_{sc})$ with $\Omega \in \mathbb{R}$, yielding the set of $\mp(\Delta U^\pm - \Delta U^\pm_{sc} + \mathrm{i}\Delta V^\pm)$ corresponding to the limit of stability. Hence this representation is known as *stability diagram* [11, 5]. The stability diagram evaluated using Eq. 3.75 is shown in Fig. 3.7. Taking both the upper and the lower side band into account yields two curves enclosing an area centered around the origin. This region is the area of stability because collective effects corresponding to a $\Delta U^\pm - \Delta U^\pm_{sc} + \mathrm{i}\Delta V^\pm$ resided within this region do not destabilize the beam. Hence a beam with momentum spread is not destabilized by arbitrarily small impedances — in contrast to the cold beam. The frictionless damping of the coherent motion of an ensemble of particles due to the incoherent motion of the constituents is called *Landau damping*.

$\mathrm{Im}(r_0^\pm) \propto \Psi(u^\pm_{sc})$ is the damping term which implies that Landau damping is maximal at the maximum of Ψ (see Eq. 3.73). Space charge shifts the resonance frequency of the particles without interfering with the coherent beam oscillation. Thus the excited coherent frequency is separated from the damping eigenfrequencies and Landau damping is suppressed. Despite the infinite range of the Gaussian distribution, which describes the momentum spread often well in the range of few σ_p, the

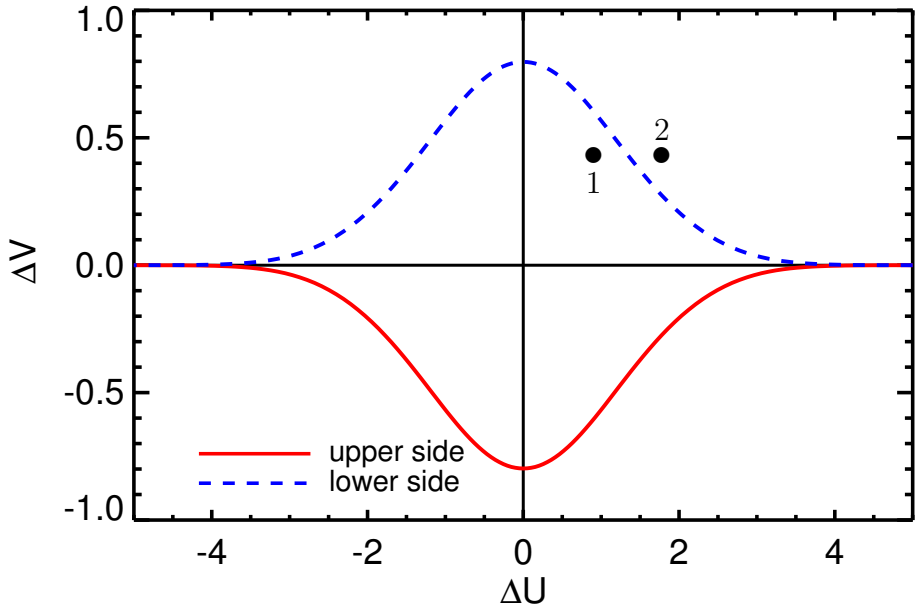

Figure 3.7: Dispersion relation with a Gaussian momentum distribution. The two curves correspond to the lower and upper side band of one harmonic m. The beam is stable if $\Delta U^{\pm} - \Delta U^{\pm}_{sc} + \mathrm{i}\Delta V^{\pm}$ is located somewhere in the region enclosed by the two curves, like point 1. Point 2 corresponds to an unstable beam.

momentum distribution in a real beam is finite. Therefore $\Delta\omega_{sc}$ can even completely prevent Landau damping. In this case, the beam behaves like a cold beam. Fig. 3.7 also exemplifies the role of space charge for the beam stability. $\Delta U^{\pm} + \mathrm{i}\Delta V^{\pm}$ corresponding to point 1 implies a stable beam. However, a shift by $\Delta U^{\pm}_{sc}$ to point 2 leads to an instability.

The parameters $U^{\pm}_{(sc)}$ and $V^{\pm}$ depend inversely on $\sigma^{\pm}_{m,\omega}$ per definition (Eq. 3.97). Thus the efficiency of Landau damping is proportional to σ_p according to Eq. 3.56. In the limit $\sigma_p \to 0$, Eq. 3.96b turns to Eq. 3.83. Due to $S^{\pm}_m$, Landau damping is different for every mode with a minimum at $m \approx Q_f - Q\xi/\eta$ for the lower side bands. Therefore the value of ξ can be critical for the beam stability. As matter of fact, instabilities have been induced in SIS-18 by setting $\xi > 0$. Subsec. 5.4 shows how ξ was measured in order to support the measurement of beam instabilities.

For large m, $\Delta U^{\pm}_{(sc)}$ and $\Delta V^{\pm}$ decrease roughly with $1/m$. Therefore the resistive wall impedance, being largest at low frequencies (see Fig. 3.6), is dangerous for the beam stability. Instabilities observed in SIS-18 are referred to the resistive wall [70]. The future SIS-100 is expected to suffer from it as well [71].

3.3.4 High-intensity BTF

In section 3.3.3 it is mentioned that Landau damping prevents beams from becoming unstable to a certain extent. Thus knowing the effectiveness of Landau damping is crucial for beam-stability issues, like the prediction of the achievable beam intensity.

Beam transfer functions (BTFs) are capable of scanning the stability limits, which makes them an important tool for the stability analysis.

The equation of motion of a particle having a momentum deviation and being a subject to collective effects as well as external harmonic excitation includes the features presented beginning from Sec. 3.2.2 to Sec. 3.3.3, and reads

$$\ddot{x}_j(t) + \omega_{\beta,j}^2 x_j(t) = \left\{ \frac{F}{\gamma m_p A} + 2\omega_\beta [\Delta\tilde{\omega}\hat{x} + \Delta\omega_{sc}(\hat{x}_j - \hat{x})] \right\} \mathrm{e}^{\mathrm{i}(n\theta - \Omega)t}. \tag{3.98}$$

Using the ansatz Eq. 3.59 and integrating over $\Phi(\hat{x}_j)$ yields the sum of Eq. 3.71 and Eq. 3.96a,

$$1 = \mp \left(\frac{F}{2\omega_\beta \sigma_{m,\omega}^\pm m_p A \gamma \hat{x}} + \frac{\Delta\tilde{\omega} - \Delta\omega_{sc}}{\sigma_{m,\omega}^\pm} \right) r_0(u_{sc}^\pm) \tag{3.99a}$$

$$= \mp \left(\frac{1}{r_m^\pm(u_{sc}^\pm)} + \Delta U^\pm - \Delta U_{sc}^\pm + \mathrm{i}\Delta V^\pm \right) r_0(u_{sc}^\pm). \tag{3.99b}$$

For the second line we recall Eq. 3.96b and the definition of the BTF, Eq. 3.72.

From Eq. 3.99 we obtain the BTF with collective effects,

$$r_m^\pm(u_{sc}^\pm) = \frac{r_0(u_{sc}^\pm)}{\epsilon^\pm(u_{sc}^\pm)}, \tag{3.100}$$

where we define the *dielectric function*

$$\epsilon^\pm(u_{sc}^\pm) \equiv \mp 1 - (\Delta U^\pm - \Delta U_{sc}^\pm + \mathrm{i}\Delta V^\pm) r_0(u_{sc}^\pm). \tag{3.101}$$

$r_m^\pm$ is observable with a network analyzer. For vanishing collective effects, Eq. 3.100 turns to the low intensity BTF (Eq. 3.73). Provided the momentum distribution (or $r_m^\pm$) is known, the strength of the collective effects can be determined from the deformation of r_m. Three examples are compared in Fig. 3.8. $\Delta U^\pm = -1$ and $\Delta U_{sc}^\pm = 1$ cause the same deformation of the BTF. The BTF deformed by space charge is, however, closer to the undistorted BTF, because ΔQ_{sc} moved the tune to right side according to Eq. 3.91. When $\Delta U^\pm = \Delta U_{sc}^\pm$ there is no deformation but the shift due to ΔQ_{sc} remains. Hence the BTF is shifted.

The stability diagram corresponding to Eq. 3.100 is given by

$$\frac{1}{r_m^\pm(u_{sc}^\pm)} = \mp \frac{1}{r_0(u_{sc}^\pm)} - \Delta U^\pm + \Delta U_{sc}^\pm - \mathrm{i}V^\pm, \tag{3.102}$$

which is simply shifted with respect to the low intensity BTF. Hence the shift provides a measure of space charge and impedances. The origin of the stability represents the beam response to an infinitely small excitation, implying beam stability if it is in the area of stability. Therefore the distance of the origin to the closest branch of the BTF indicates how far the beam is away from an instability.

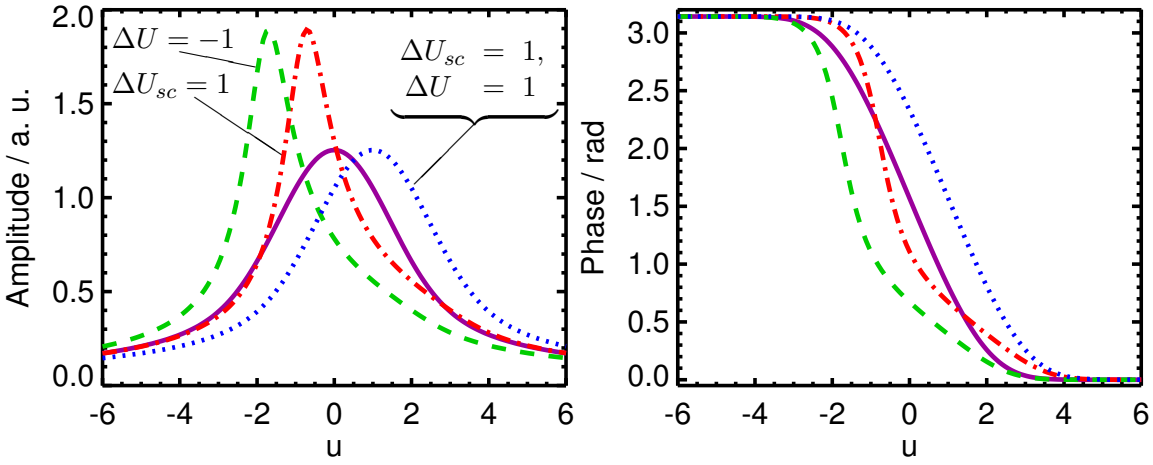

Figure 3.8: Gaussian BTF of a lower side band deformed by space charge and a reactive impedance. The solid line shows the BTF without collective effects. The other graphs correspond to the parameters provided in the left plot.

3.3.5 High-intensity Schottky diagnostics

In subsection 3.2.1, the Schottky spectrum of a beam consisting of a large number of non-interacting particles is presented. However, impedances and space charge modify the Schottky spectrum drastically. An analytic expression for Schottky bands affected by impedances can be derived using a microscopic kinetic model [14,72]. This derivation is quite complicated and is not treated here. Instead, a more illustrative approach presented in Ref. [14] is followed.

As starting point, the BTF is considered from a more general point of view. Using Eq. 3.72 and excluding collective effects, one may write $\hat{x} = c_1\, F\, r_0$ with $c_1 = 1/(2\omega_\beta \sigma^{\pm}_{m,\omega} m_p A \gamma)$. r_0 is a function relating the input F of a system to its output $\hat{x}$. Fig. 3.9 illustrates this process in a block diagram with the solid arrows. Now collective effects are included. They give rise to forces depending on $\hat{x}$. In the picture of the block diagram, a branch linking the output of r_0 with its input represents the self-interaction where a gain factor g quantifies the strength of the feedback. The addition of $g\hat{x}$ to the input in turn gives an additional output $gr_0\hat{x}$ which is again multiplied by g and fed back to the input. This cycle repeats for ever. Substituting the loop by the effective transfer function r, as indicated in Fig. 3.9, we find $\hat{x} = c_1 F r$ which is equivalent to Eq. 3.72. Provided $|gr_0| < 1$, r can be represented by the limit of the geometrical series

$$r = r_0 \sum_{k=0}^{\infty} (gr_0)^k = \frac{r_0}{1 - gr_0}. \tag{3.103}$$

Identifying g with $\Delta U^{\pm} - \Delta U^{\pm}_{sc} + \mathrm{i}\Delta V^{\pm}$ we find that we have rederived Eq. 3.100.

A block diagram can similarly be applied to the fluctuation of the current dipole-moment, δd, introduced in subsection 3.2.1. Now the excitation stems not from an external force F but merely from an initial fluctuation δd_0. Due to collective

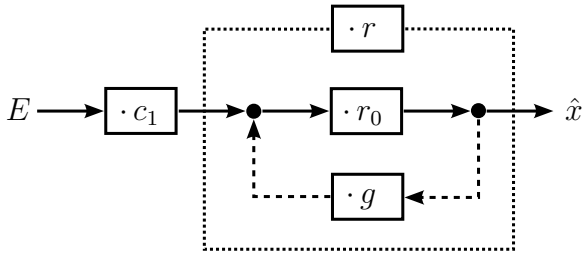

Figure 3.9: Block diagram representing a BTF. Without collective effects, i. e. $g = 0$, only a constant c_1 and r_0 turn the input into the output as indicated by the solid arrows. The dashed arrows indicate the feedback of collective effects with the gain factor $g \neq 0$. The loop formed by r_0 and g can be replaced by the effective BTF r.

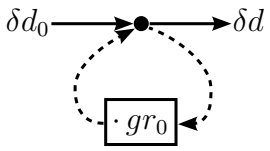

Figure 3.10: Block diagram representing the self-interaction of a fluctuation of the dipole moment δd_0.

effects, a force proportional to gr_0 arises and modifies δd_0 by $\delta d_0 gr_0$. This additional dipole moment in turn gives another contribution to the collective interaction. The alternating change of the current dipole-moment and the collective feedback go on in an infinite loop. The corresponding block diagram is shown in Fig. 3.10.

Evaluating the geometric series $\sum_{k=0}^{\infty}(gr_0)^k$ yields the final current dipole-moment $\delta d = \delta d_0/(1 - gr_0)$. A quantitative statistical modeling reveals [14]

$$\delta d = \frac{\delta d_0}{\epsilon^{\pm}}. \tag{3.104}$$

The transverse Schottky spectrum is obtained from the Fourier transform of the auto-correlation function of δd (Eq. 3.53). Thus a transverse Schottky band with a deformation due to an impedance is given by [14, 72, 28]

$$P_m^{\pm}(u^{\pm}) = \frac{P_{m,0}^{\pm}(u^{\pm})}{|\epsilon^{\pm}(u^{\pm})|^2}, \tag{3.105}$$

where the low intensity Schottky band $P_{m,0}^{\pm}$ is provided by Eq. 3.57.

The description of transverse Schottky spectra with space charge is quite intricate. Based on the statistical theory of plasmas [73], an expression looking similar to Eq. 3.105 is derived for Schottky bands with space-charge in Ref. [28]. In the linear approximation we assume

$$P_m^{\pm}(u_{sc}^{\pm}) = \frac{P_{m,0}^{\pm}(u_{sc}^{\pm})}{|\epsilon^{\pm}(u_{sc}^{\pm})|^2}, \tag{3.106}$$

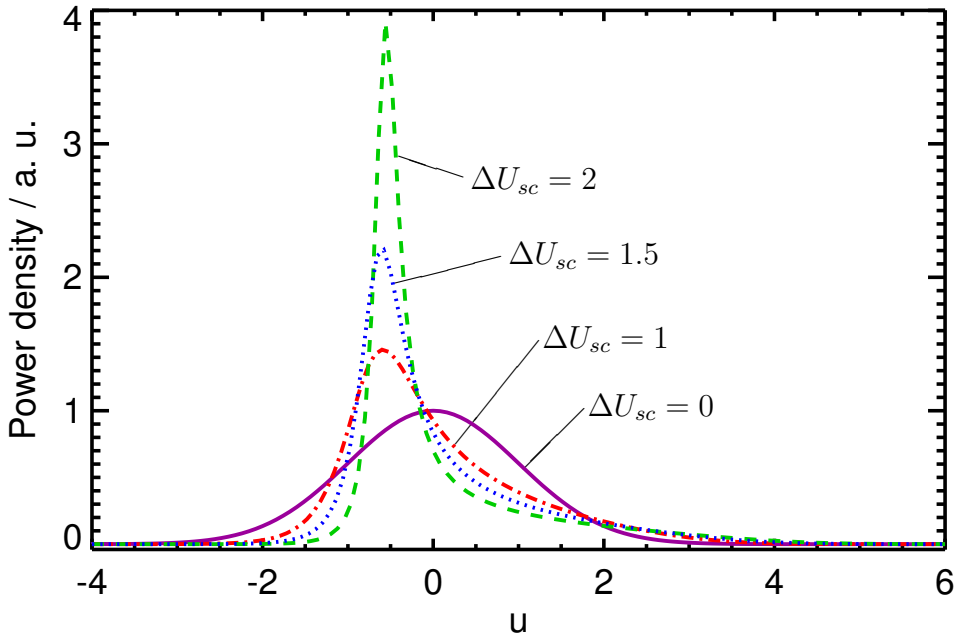

Figure 3.11: Deformation of a lower Schottky side band due to different space charge parameters.

where $\epsilon^{\pm}$ is defined in Eq. 3.101. The difference between an impedance and space charge manifests itself only in the shift of $u_{sc}^{\pm}$, as found for the BTF in Subsec. 3.3.4. Hence space charge and imaginary impedances produce the same deformation but shift the maximum to different positions. For this reason, in Fig. 3.11 only the effect of different space-charge parameters is demonstrated.

At this point we have derived a model to describe impedance and space-charge effects in transverse Schottky spectra and BTFs. This model is used to analyze the data from measurements in Chap. 5 and simulations in Chap. 7. The equipment used in experiments to measure the impact of space-charge is the topic of the next chapter.

Chapter 4

Beam diagnostics in SIS-18

The principles of Schottky and BTF diagnostics are introduced in Chap. 3 at a rather theoretical level. This chapter is dedicated to the technical aspects of the experiments performed in SIS-18. The hardware used to measure Schottky spectra and BTFs is described in Sec. 4.1 and Sec. 4.2, respectively. The post-processing of the data is explained as well, without analyzing the physical information.

An ionization profile monitor (IPM) is mounted in SIS-18 to measure beam profiles. With these profiles, a and ϵ were determined in the experiments. The IPM is presented in Sec. 4.3 because the emittance of the beam was used to estimate ΔQ_{sc}.

4.1 Schottky diagnostics

A system for Schottky diagnostics was developed for ESR [15]. A replicate of the system was mounted in SIS-18 without modifications of relevance for this work [22]. The basic components are sketched in Fig. 4.1. A detailed description of the hardware is given in Ref. [15].

The probe for the detection of the beam's Schottky noise is a plate capacitor in the beam pipe. Fig. 4.2 shows a picture of the pick-up. Two pairs of metal plates are installed to allow horizontal and vertical measurements. The plates are shaped concavely to provide a linear response to the offset of the beam. As the horizontal acceptance of SIS-18 is larger than the vertical one, the gap between the horizontal plates has to be wider. For this reason, the vertical probe has a better signal-to-noise ratio.

The current detected by the pick-up is smaller than the beam current for weakly relativistic beams. In order estimate the performance of the detector we consider the image current induced by the beam in the beam pipe. The image currents in a pipe with the radius b are by a factor $1/I_0[\omega b/(\beta\gamma c)]$ smaller than the beam current, where I_0 is the modified Bessel function of zeroth order [74]. A suppression of the image currents by 3 dB, often chosen as tolerance level, occurs at $f_{3dB} = 0.19\,\beta\gamma c/b$. With $b \approx 7$ cm, $\beta \approx 0.15$ and $\gamma \approx 1$ at injection, we find $f_{3dB} \approx 127$ MHz as the upper frequency limit. This is far above the frequencies considered in this work.

More critical for the experiments aiming to observe collective effects is the lower

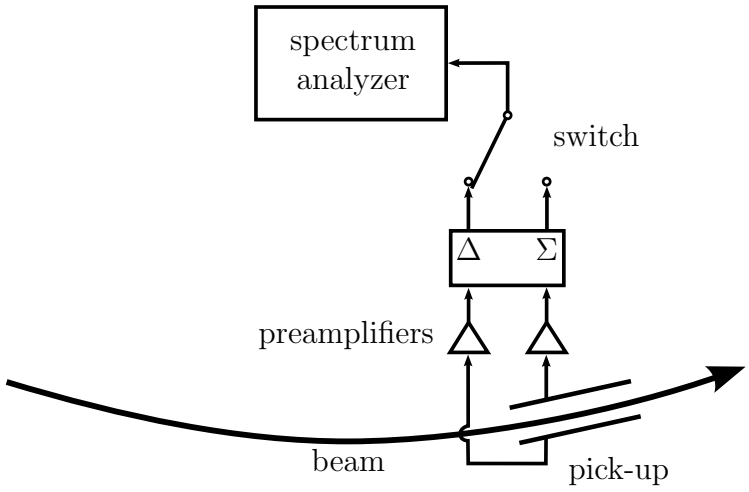

Figure 4.1: Setup of a Schottky measurement. The spectrum of the beam is detected by the two plates of the Schottky pick-up. After a preamplification, the sum and the difference of the signals are taken and directed to different ports. A switch allows to connect one of the ports with the spectrum analyzer.

frequency limit, because $\Delta U_{(sc)}$ and ΔV (Eq. 3.97) are largest at low frequencies. Below 10 MHz the signal-to-noise ratio drops [15] and the amplifiers do not work linearly [22]. For this reason the measurements were accomplished at frequencies above 10 MHz.

The measurements in this work were performed with an electrostatic pick-up. Such a pick-up has one port connected with a preamplifier by a coaxial cable and no other connections. The alternative strip-line pick-up, with a second port connected to a non-reflecting closed end, provides a lower signal-to-noise ratio at low β [15].

A switch allows to change between the resonant and the non-resonant operation of the probe. For the former, a splitter conducts a part of the signal current into a cable resonator. The resonant mode is advantageous for weak signals as it features a higher signal-to-noise ratio. At high intensity, however, the pick-up disturbs the beam in this mode. Furthermore the resonance frequency is adjustable in a range above 20 MHz only, where the emerging collective effects are much weaker than at frequencies close to 10 MHz. Therefore the non-resonant mode was used.

The sum of the preamplified outputs from a pair of plates yields a signal proportional to the beam current. Thus the sum of the signals indicates the longitudinal Schottky spectrum of the beam. The difference of the signals on the other hand provides a measure for the current dipole-moment — this is the transverse Schottky spectrum.

The amplified signals were recorded with a RSA3303A, a real-time spectrum analyzer from Tektronix®. A screen-shot from the spectrum analyzer is shown in Fig. 4.3. This device offers several operation modes but only in the real-time spectrum analyzer mode it can be triggered externally [75,76]. External triggering was compulsory

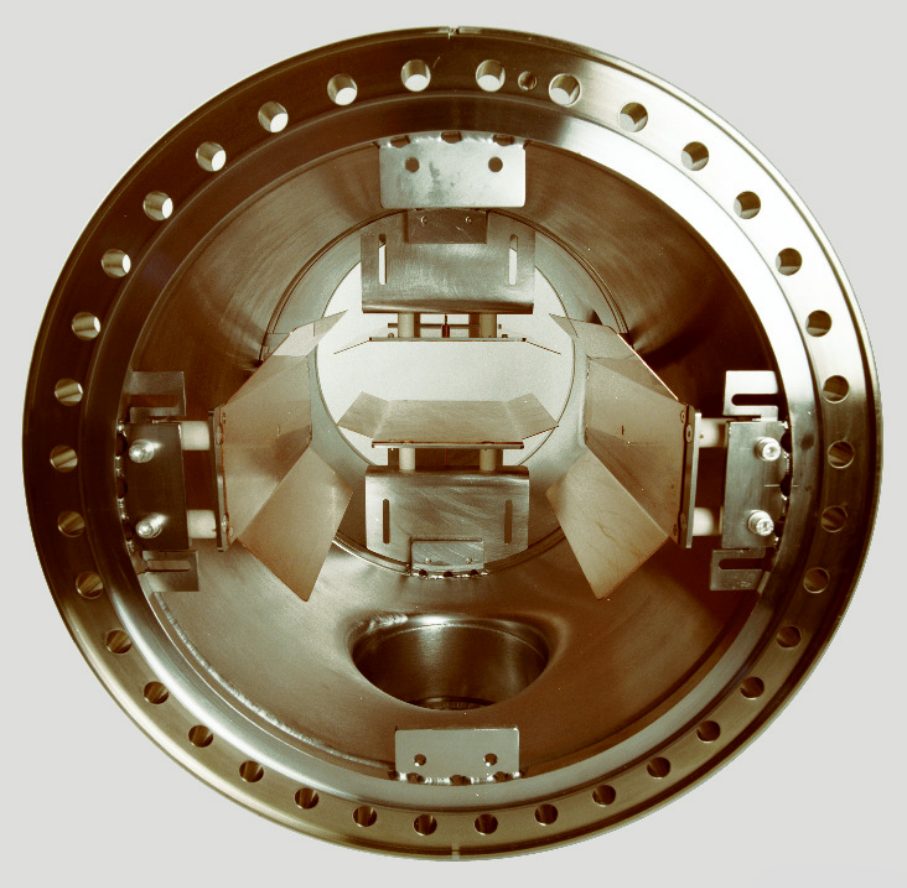

Figure 4.2: Picture of the Schottky pick-up. In the front one sees the horizontal detector and behind the vertical one. (Courtesy A. Zschau)

to synchronize the data acquisition with the cycle of the synchrotron, so the real time mode had to be used. The user can set the frequency span and the center of the measurement as well as the measuring time.

A single spectrum is called *frame*. The measuring time of one frame, the *frame time*, decreases with increasing span. Once triggered, data are acquired until the measuring time is reached. The full data set is called a block. The number of frames in a block is given by the ratio of the measuring time to the frame time. Due to the poor signal-to-noise ratio of the Schottky spectra, several hundred frames have to be averaged to gain a clear Schottky signal. The ideal setup of a measurement is a compromise between optimal span, frequency resolution, measuring time and number of frames.

The spectrum analyzer saves the data in a binary (iqt) format only, but upon request Tektronix® supplied a software called 'ReadIQT' (version 2.02) for the conversion into the ASCII format. All measured Schottky spectra were converted applying that software. In the real-time mode each frame consists of a fixed number 1024 points, among them 641 so-called *bins*. The bins contain the physical data of the measurement, the others are artificial byproducts of the fast Fourier transform

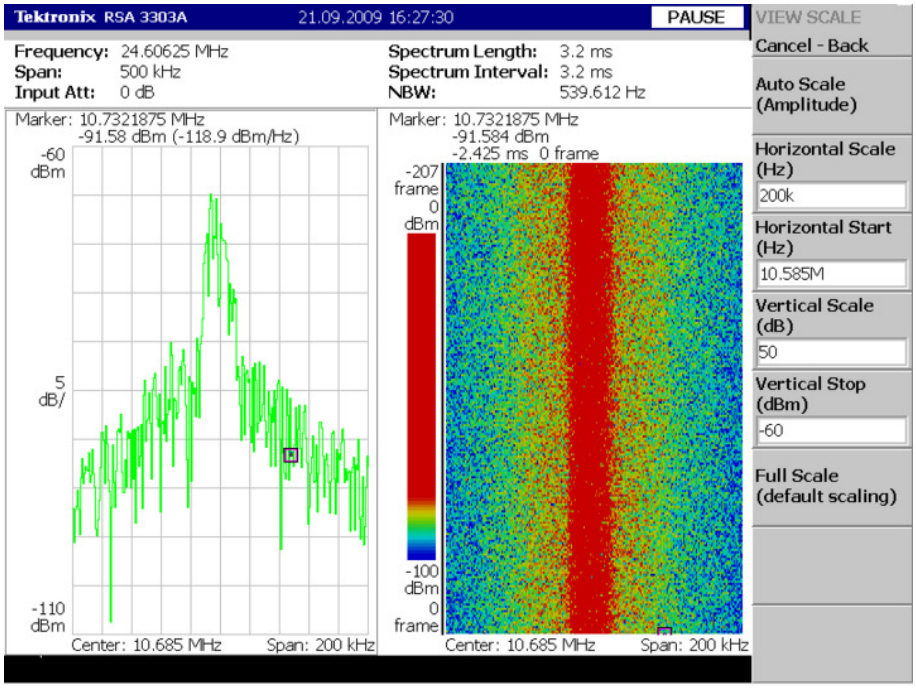

Figure 4.3: Screen-shot of the spectrum analyzer after the measurement of a longitudinal Schottky band. On the left side one frame is shown in dBm. On the right side, 207 frames, stacked on top of each other with the most recent one at the bottom, are displayed as a spectrogram. The coloring indicates the power level.

and can be discarded.

A C++ program was written to process the data. First it separates the bins from the non-physical data. If desired, only a fraction of the span or the frames is regarded. Then the average of the selected data is evaluated. Finally the amplitude provided in Volt is converted to Watt since the Schottky theory refers to power densities. The averaged power spectrum and optionally the real-time spectrum are written to files.

4.2 BTF diagnostics

For BTF measurements, a network analyzer is employed to produce the excitation signal and to acquire the beam's response. The amplitude and the phase of the response-to-excitation ratio are displayed and can be written to files. In the experiment presented in this work, a ZVB4 Rhode & Schwarz® network analyzer was employed.

Fig. 4.4 illustrates the setup of a BTF measurement. The network analyzer is connected to a 0°/180° hybrid which outputs the incoming signal on two ports with a phase shift of π between them. Power amplifiers enhance the signals before they are applied to a kicker which excites the beam. A description of the kicker can be found in Ref. [15]. It is interconnected as strip-line to enhance its coupling to the beam. Due to the phase shift between the signals transfered to the two plates of the

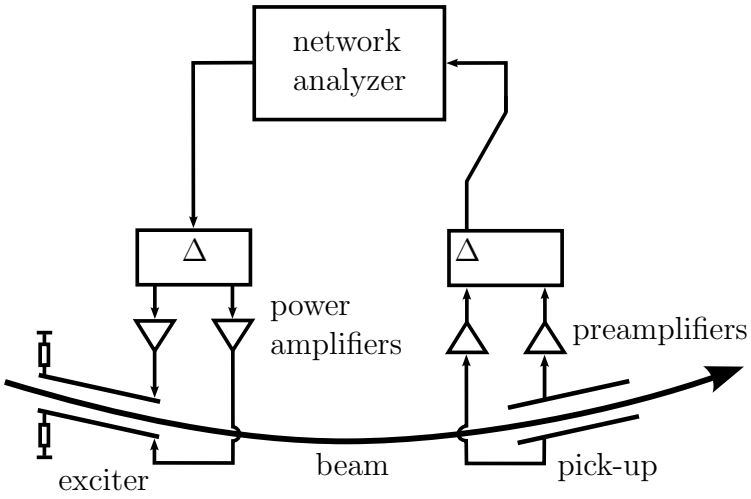

Figure 4.4: Setup of a BTF measurement. The right part of the figure is similar to Fig. 4.1, with the difference that for the transverse BTF only the difference signal is used. On the left side the exciting signal is split in two with a phase shift of π. Both are magnified and transmitted to the exciter. The wires from the hybrid to the exciter have the same optical length.

exciter, the beam is excited transversely. The response of the beam is detected as described in Sec. 4.1, with the distinction that only the difference signal is useful for the transverse BTF.

A BTF is acquired sweeping over a selected frequency range with a selected number of frequency steps. The duration of the excitation at each frequency must be long enough for the beam to reach an equilibrium, taking into account the run time of the signal. In the experiment presented here, a sweep with up to 2000 frequency steps was performed within 3 s.

The data were saved in ASCII files containing the frequency and the corresponding amplitude and phase of the BTF. Due to the long detection time, the noise on the data can not be suppressed by acquiring many data sets and subsequent averaging. Particularly the stability diagrams are affected by the noise. In order to improve the signal quality, a *Mathematica*® 6 [77] script was written to apply a time gating procedure as proposed in Ref. [78] for the noise suppression.

The first step of the time gating procedure is a discrete Fourier transformation of the BTF data. In the time domain, the response to the excitation decays quickly and most data points contain only noise. After the erasure of the noise, the inverse discrete Fourier transformation generates the cleaned BTF. Since there is no sharp changeover from the signal to the noise, the filtering process leads to artifacts. Therefore the time gated signals feature a modulation-like deformation in some parts. The limits of the filter were adapted for each data set to keep this distortion as low as possible. Overall the signal quality is significantly improved despite minor degradations. A sample of data before and after filtering is shown in Fig. 4.5.

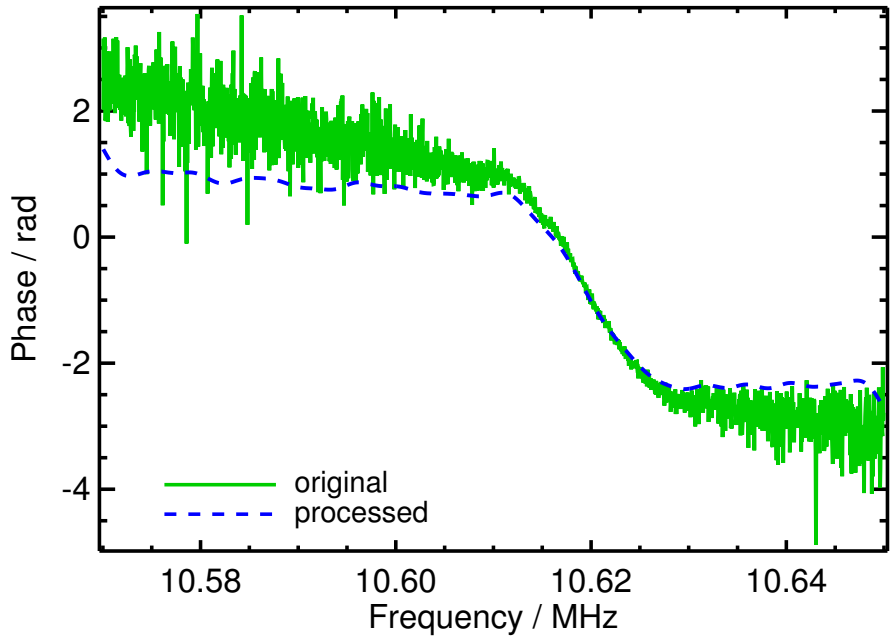

Figure 4.5: Example for the effects of the time gating and of the correction of the phase drift. The slope of the straight sections of the phase indicates the phase drift. The drift is compensated for the filtered signal.

Another artifact disturbing the analysis, also visible in Fig. 4.5, is a *phase drift*. Off the resonance the phase should converge against constant values on both side as seen in Fig. 3.8. However, the measured phase decreases within the entire interval. Also the change of the phase in the resonant region is larger than π. This observation can be attributed to the run time of the signal from the output port to the input port of the network analyzer.

As Fig. 4.4 shows, the run time is given by the propagation time to the exciter, the traveling time of the beam to the pick-up and the propagation time from the pick-up to the network analyzer, including some electronic devices on the way. The absolute time difference does not matter to the BTF, but during a sweep the phase associated with the run time changes by

$$\Delta\varphi = \Delta\Omega\, t_{run}, \tag{4.1}$$

where $\Delta\Omega$ is the frequency span of the BTF. Since the run time of the signal could not be measured with the required accuracy, the correction of the phase-drift was performed empirically. A linear function was added to the measured phases to rotate the straight sections into the horizontal plane. This procedure also changed the difference between the phases to the left and to the right of the resonance to π. A correction of 27 rad/MHz was determined to give the best results. Measured at about 10 MHz, this corresponds to $t_{run} \approx 5\,\mu$s — a reasonable value taking into consideration several 100 m of cable with a propagation speed of $0.7\,c$ and $0.9\,c$, respectively, delays in the electronics, and the traveling time of the beam [79]. The line representing the *processed* data in Fig. 4.5 shows the effect of this correction as well.

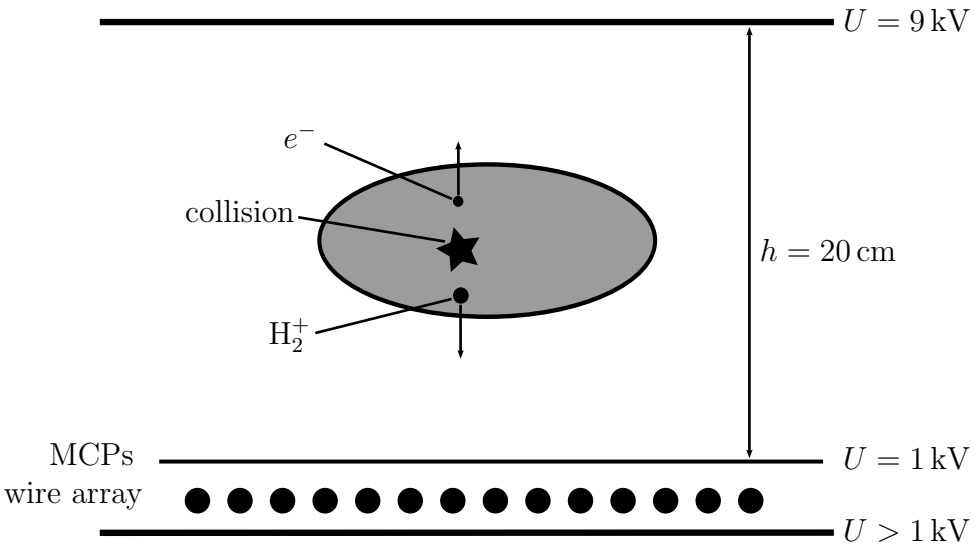

Figure 4.6: Sketch of the IPM in operation. On the right hand side, the electrostatic potential of the components is indicated. A beam ion hits an H_2 molecule which is then ionized and accelerated downwards by the electric field $E_{ipm} = 40\,\mathrm{kV/m}$. The impact onto the MCPs leads to the emission of electrons. The electric field below the MCPs accelerates these electrons further downwards where they are collected by the wire array.

4.3 Ionization profile monitor

The tune shift due to space charge can be estimated from the beam parameters independently of the Schottky and BTF measurements. In order to apply Eq. 3.94, the transverse emittance of the beam has to be calculated from the measured rms beam width using Eq. 3.29. For the measurement of beam profiles, an ***i****onization* ***p****rofile* ***m****onitor* (IPM) is available in SIS-18 [80, 81]. The features of the IPM, including its limitations, are presented in this section.

The mode of operation is illustrated in Fig. 4.6. Molecules of the residual gas with a pressure of nearly 10^{-11} mbar [52] are ionized by collisions with beam particles. The frequency of ionizations is proportional to the density of the beam particles. A homogeneous electric field of several 10 kV/m accelerates the ions towards two micro channel plates (MCPs) on top of each other (Chevron configuration). Supplied with a voltage of about 1 kV, an MCP emits roughly 10^3 electrons when hit by a charged particle. The layer hence liberates 10^6 electrons. The electric field between the MCPs and the anode accelerates these electrons onto a wire array, where most of them are caught. The wires have a diameter of 1.5 mm and a center-to-center distance of 2.1 mm. For a large number of ions hitting the MCPs, a profile can be determined with a higher accuracy than the spacing between the wires, as long as the beam width is large compared to the spacing. The current collected by each wire is transformed to a voltage, amplified, digitized and registered by the data acquisition system. The

data are then cleared from the noise of the electronics.

During one measuring cycle, profiles are acquired every 10 ms with a collection time of 0.5 ms or 5 ms. The array displayed in Fig 4.6 collects a current proportional to the projection of the two dimensional particle density-distribution onto the horizontal plane. For vertical profile measurements, a second device with an orthogonal orientation is installed. The full reconstruction of the two-dimensional distribution can not be accomplished from the two projections, so an assumption has to be made. A bi-Gaussian distribution can be supposed if the observed profiles are well described by Gaussian distributions. This assumption was adopted in this work.

The MCPs are known to wear out as a consequence of the impact of charged particles [82, 83]. For this reason the response of the MCPs becomes spatially non-linear with a minimum in the region of maximal intensity. The MCPs employed in the measurements were several years old and expected to be in a bad state [83]. The actual condition was unknown, though. Recently it was discovered that the response of the MCPs depends on the temperature which changes while the IPM is in use [83]. A non-linear signal suppression with the strongest reduction at the maximum gives the measured curve a larger standard deviation relative to the original one. Hence the actual beam width could be smaller than indicated.

In order to estimate this effect, we evaluate the measured standard deviation a_{mes} of a signal stemming from a Gaussian distribution, $f(x) = A\,\mathrm{e}^{-x^2/2a^2}$, multiplied with the amplitude dependent suppression function $g(x) = 1 - B\,\mathrm{e}^{-x^2/2a^2}$ with $0 < B < 1$ and obtain

$$a_{mes} = \sqrt{\frac{\int x^2 f(x)\, g(x)\,\mathrm{d}x}{\int f(x)\, g(x)\,\mathrm{d}x}} = a\sqrt{\frac{1 - B/2\sqrt{2}}{1 - B/\sqrt{2}}}. \tag{4.2}$$

Setting $B = 0.5$ yields

$$\frac{a_{mes}}{a} \approx 1.1, \tag{4.3}$$

an overrating of the actual beam width by 10%. Larger values of B can be excluded because they would visibly deform the measured profiles.

Another problem arises at high beam intensities because space charge interferes with the electric field of the IPM [84]. Obviously all ions not moving on the symmetry axis of the beam experience a repulsive force so that the measured beam profile is broadened. For the beams for FAIR, this effect is so serious that the development of profile monitors insensitive to the self-field of the beam has already started [80].

We attempt to estimate the space-charge effect on our profile measurements with a simple model. A homogeneous vertical electric field E_{ipm} accelerates ionized residual gas molecules towards the MCPs. In SIS-18 the height of the IPM is $h = 20$ cm [83]. With a vertical voltage of 8 kV the vertical field is $E_{ipm} = 40$ kV/m. The radial electric field of a beam with a circular Gaussian profile reads [4]

$$E_\rho(x, y) = \frac{eZN}{2\pi\epsilon_0 C\rho}\left[1 - \mathrm{e}^{-\rho^2/(2a^2)}\right], \tag{4.4}$$

where $\rho = \sqrt{x^2 + y^2}$ is the distance from the beam center. Consider a molecule hit

at $y = 0$ and $x \approx 1.6\,a$, where E_x is maximal, and yields

$$E_{x,max}(1.6\,a, 0) = 0.45\frac{eZN}{2\pi\epsilon_0 Ca}. \tag{4.5}$$

The vertical acceleration due to E_y is negligible compared to E_{ipm}. With the vertical path length $d_y = h/2$, it follows

$$\Delta x_{sc} < d_y E_{x,max}/E_{ipm}. \tag{4.6}$$

Thus we found an estimation for the upper limit of the deflection due to space charge based on a few parameters only. Anticipating the beam parameters in our experiment (Tab. 5.1) we assume $Z = 18$, $N = 1.1 \cdot 10^{10}$ and $a = 5\,\mathrm{mm}$, and find $E_{sc} \approx 240\,\mathrm{V/m}$. The impact position of the ion is consequently shifted by

$$\Delta x_{sc} < 0.6\,\mathrm{mm}, \tag{4.7}$$

which implies $\Delta x_{sc}/a < 0.1$.

Since the field does decrease with increasing distance from the beam center, the relation 4.6 overestimates the actual effect. On the other hand the molecule is the slowest immediately after the ionization and therefore most affected by the self-field at the place of the collision. The tracking of the field along the path, the calculation of the trajectories beginning at arbitrary (x, y) and finally the reconstruction of a deformed profile requires a computational modeling which is not subject of this work.

Chapter 5

Experimental Results

Various experiments were performed in SIS-18 in order to study collective effects. Since the equipment as well as the beam quality improved from measurement to measurement, and experience with the settings was gained, the latest experiment yielded by far the best results. Therefore this document reports only on the results of this experiment. For a report on intermediate results, see Ref. [85, 86]. A part of the data treated here was published in Ref. [87]

In Sec. 5.1 the measurements of the beam parameters used for the following analysis are explained. The measured transverse Schottky spectra and BTFs are presented in Sec. 5.2 and compared to the model. In Sec. 5.3 the tune shift and the space-charge parameter obtained from the Schottky and BTF data as well as from the estimation based on the beam parameters are discussed.

5.1 Auxiliary measurements

The measurements were performed using $^{40}Ar^{18+}$ beams at the injection energy of 11.4 MeV because ΔU_{sc} is largest at low beam energy, as mentioned in Sec. 3.3. The particle number was varied from $2.5 \cdot 10^8$ ions, which was the minimal beam intensity for the detectors, to $1.1 \cdot 10^{10}$ ions. Beams with higher intensity could not be stored with acceptable losses. The corresponding minimal and maximal beam currents were 0.15 mA and 6.8 mA, respectively. The change of N_p was accomplished by varying the current in the injector without touching the parameters of the injection into SIS-18. In this manner the emittance was nearly conserved. Previous experiments had demonstrated that readjustments associated with changes of the emittance lead to larger uncertainties of the results.

All data presented here were acquired in the vertical plane in order to take advantage of the better signal-to-noise ratio in this direction. On the one hand the detector is designed for use at frequencies above 10 MHz; on the other hand collective effects are strongest at low frequencies. Therefore $m = 50$ corresponding to nearly 10.68 MHz was chosen for the Schottky and BTF measurements. Longitudinal Schottky spectra were recorded to determine f_0 and σ_p. The presence of longitudinal collective effects was excluded from the observation of the undeformed longitudinal Schottky spectra.

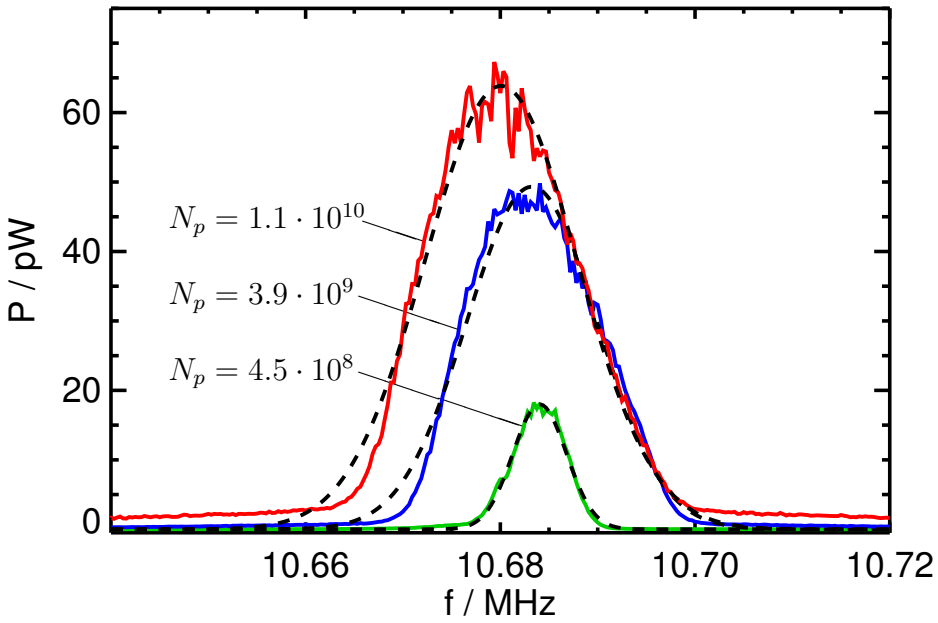

Figure 5.1: Longitudinal Schottky bands measured at three different beam intensities with fitted Gaussian distributions. The harmonic number, m, is 50.

Fig. 5.1 depicts three longitudinal Schottky bands and the model which was fitted to the data assuming a Gaussian distribution. The assumption of a Gaussian momentum distribution is approximately verified. There are only small deviations on the left slope. At high intensity the tails of the distribution are larger than those of the Gaussian model. The fit yielded f_m and $\sigma_{m,f}$ from which f_0 and σ_p were calculated using Eq. 3.44 and Eq. 3.45, respectively. Their values are included in the list of the beam parameters Tab. 5.1. The amplitudes of the bands were also extracted from the fit but as they were not relevant for the following analysis, they are not listed.

Obviously $\sigma_{m,f}$ increases with increasing N_p while f_m decreases. The reason for this behavior is not fully understood, but it is supposed that collective effects in the

Table 5.1: Parameters characterizing the beams used in the experiment. The Schottky bands were measured at $m = 50$. $\sigma_{lon}^{\pm}$ are the calculated rms widths of the side bands.

N_p /10^9	f_m /MHz	$\sigma_{m,f}$ /kHz	f_0 /kHz	σ_p /10^{-4}	a_y /mm	ϵ_y /mm mrad	σ_{lon}^{-} /kHz	σ_{lon}^{+} /kHz
0.25	10.6837	2.53	213.674	2.52	6.4	5.3	2.85	2.21
0.45	10.6840	2.76	213.680	2.75	5.7	4.2	3.11	2.41
0.90	10.6845	4.25	213.690	4.23	5.5	3.9	4.79	3.71
2.	10.6841	5.59	213.682	5.57	5.7	4.2	6.30	4.88
3.9	10.6832	6.69	213.664	6.66	5.7	4.2	7.54	5.84
7.	10.6812	7.59	213.624	7.56	5.7	4.2	8.56	6.22
10.	10.6799	7.82	213.598	7.79	5.7	4.2	8.82	6.82
11.	10.6801	7.81	213.602	7.78	5.9	4.4	8.81	6.81

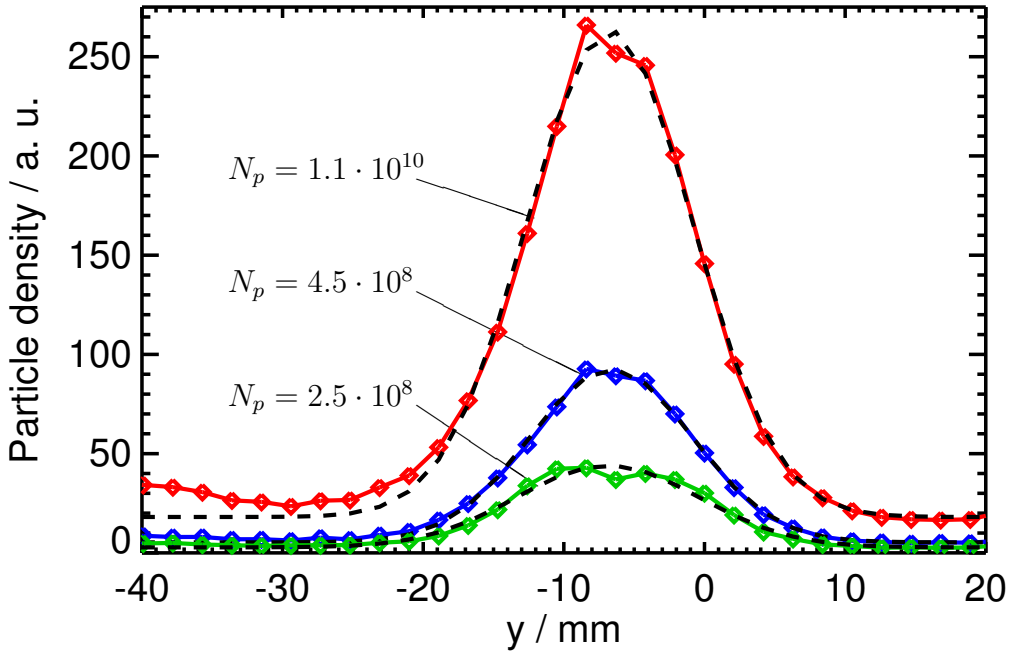

Figure 5.2: Vertical beam profiles measured at the two minimal and the maximal beam intensities.

transfer channel from UNILAC to SIS-18 are responsible. Investigations aiming to clarify this issue are ongoing [88]. The knowledge of f_0 and σ_p for each beam is crucial for the following analysis. The shift found in the longitudinal measurements was compensated in the transverse data so that the changes of their position can be exclusively ascribed to ΔQ_{sc}.

The momentum spread was used to calculate the widths of the side bands using Eq. 3.56 because this reduced the degrees of freedom of the transverse fit. The benefit was that the other fit parameters could be retrieved with a lower uncertainty. The lattice parameters were set to $\eta = -0.94$, according to Ref. [36], and the natural chromaticity, according to the SIS-18 control system (SISMODI), $\xi \approx -1.9$. The knowledge of the latter is actually not very accurate, but for $m = 50$, this uncertainty is not very important. In order to emphasize that the width of the side bands was derived from longitudinal measurements, we label this parameter with the subscript *lon* and write $\sigma^{\pm}_{lon}$.

A Gaussian distribution was also fitted to the beam profiles providing the vertical and horizontal rms beam widths, a_y and a_x, respectively. Fig. 5.2 presents the vertical profiles measured at the highest and the two lowest intensities. The notch on the maximum of the signals, observed in all vertical measurements, is an artifact produced by the IPM. Nevertheless, the Gaussian distribution gives a good approximation of the data. Only at the lowest intensity a stronger deformation is observable.

Using Eq. 3.29 and the beta function at the IPM, $\hat{\beta}_{ipm}$, the emittances were evaluated. The beta functions are $\hat{\beta}_{y,ipm} = 7.8\,\mathrm{m}$ and $\hat{\beta}_{x,ipm} = 6.28\,\mathrm{m}$, according to a simulation of the beam optics in SIS-18 [89]. The resulting emittances have a ratio

$\epsilon_x/\epsilon_y \approx 1.4$. Due to $Q_y/Q_x \approx 0.8$, the square root in Eq. 3.94, when applied to the vertical plane, is approximately equal to ϵ_y. Hence the tune shift can be calculated in good approximation assuming a circular beam. Introducing the parameter ΔQ^{ϵ}_{sc}, in order to distinguish the estimation from the Schottky and BTF measurements, we write

$$\Delta Q^{\epsilon}_{sc} \approx \frac{r_p Z^2 N_p}{8\pi A \beta^2 \gamma^3 \epsilon_y}, \tag{5.1}$$

which describes the tune shift of a circular beam in a machine with similar tunes in both planes. For four beams, no profiles were saved as the displayed beam size did not change when the beam current was changed. In Tab. 5.1 the mean value of the measured values, excluding the measurement with $N_p = 2.5 \cdot 10^8$ ions, are listed for these cases. The small changes of ϵ_y permit us to express the change of the phase-space density as a function of N_p only.

With the beam parameters of the experiment, the maximal values of the collective parameters, defined in Eq. 3.97, can be estimated. Considering the upper side band at the maximal intensity and applying Eq. 5.1, we find $\Delta U^{+}_{sc} = 1.7$. The beam pipe actually has a variable cross-section. A list of the apertures in SIS-18 was compiled by C. Omet [53] and collaborators in the FAIR synchrotrons group. For our estimation we use the mean aperture $b_y \approx 70\,\mathrm{mm}$ and $b_x \approx 100\,\mathrm{mm}$. Assuming, for simplicity, a circular shape with the radius b_y, Eq. 3.85 yields $\Delta U^{+} \approx 0.007$. This is very small relative to ΔU_{sc} and still larger than the actual value for an elliptical beam pipe.

A real impedance of $100\,\mathrm{k\Omega/m}$, which is of the order of the kickers' impedance at 10 MHz in the horizontal plane, according to Fig. 3.6, gives rise to $\Delta V^{+} = 3 \cdot 10^{-4}$, being by far too small to be detected. The impact of the resistive wall and the kickers in the vertical plane is even much weaker. Therefore $\Delta V^{\pm} = 0$ is assumed in the following analysis.

5.2 Transverse Schottky spectra and BTFs

The linear space-charge model for transverse Schottky bands with collective effects was fitted to the data with a Mathematica® script using the preimplemented Levenberg-Marquardt algorithm. For this purpose, Eq. 3.106 was parameterized as

$$P^{\pm}_{m}(f, A, f^{\pm}_{m,sc}, \sigma^{\pm}_{lon}, B) = \frac{A\,\mathrm{e}^{-(u^{\pm}_{sc})^2/2}}{|\mp 1 - \Delta U^{shape}_{sc}\, r_0(u^{\pm}_{sc})|^2} + B, \tag{5.2}$$

where

$$u^{\pm}_{sc} \equiv (f - f^{\pm}_{m,sc})/\sigma^{\pm}_{lon} \tag{5.3}$$

and

$$\Delta U^{shape}_{sc} = \Delta U^{\pm}_{sc} - \Delta U^{\pm} \tag{5.4}$$

as deformation parameter. This way image currents were not excluded, though it was estimated that $\Delta U^{\pm} \ll \Delta U^{\pm}_{sc}$, in order to check the consistency of the deformation with the shift of the incoherent tune. In Sec. 5.3 this is explained in detail. The fit parameters are A, B, $f^{\pm}_{m,sc}$ and ΔU^{shape}_{sc}. $\sigma^{\pm}_{lon}$ was set to the values listed in Tab. 5.1.

Note that the shift of f_0 was compensated in the data presented below. Fig. 5.3 shows the lower and upper Schottky bands of the beams whose longitudinal spectra are depicted in Fig 5.1. At low intensity, the side bands look like Gaussian distributions. On the upper side, a flat tail to the left of the band is visible, though. At higher intensity, the bands are deformed asymmetrically in such a way that the lower and upper band of one beam look almost like mirror images of each other, as predicted by the space-charge model. A difference between them arises from the difference between σ_{lon}^{-} and σ_{lon}^{+}. The fit of Eq. 5.2 is included in the plots and shows a good agreement with the lower and upper side bands. The upper Schottky band corresponding to $3.9 \cdot 10^9$ ions is shifted with respect to the others due to an unknown reason.

Also for the fitting of the BTF model, Mathematica® was employed. As a BTF provides two data sets, the amplitude and the phase, two fits can be performed independently. However, the physical parameters $f_{m,sc}^{\pm}$ and ΔU_{sc}^{shape} gained from both fits have to coincide — otherwise the BTF model is inconsistent. Nevertheless deviations occur because of the limited accuracy of both the measurement and the fitting procedure. Therefore the arithmetic mean of such pairs of fit parameters was taken as result.

The implementation of the BTF model starts from r_0 (Eq. 3.70), which split into its real and imaginary part

$$r_0(u_{sc}^{\pm}) = \hat{f}(u_{sc}^{\pm}) + \mathrm{i}\hat{g}(u_{sc}^{\pm}), \tag{5.5}$$

where $u_{sc}^{\pm}$ is defined in Eq. 5.3. Then the amplitude and phase of $r_m^{\pm}$ (Eq. 3.100) read

$$A_{btf}(f, A, f_{m,sc}^{\pm}, \sigma_{lon}^{\pm}, B_A) = A\left[\frac{1 \pm 2\Delta U_{sc}^{shape}\hat{f}}{\hat{f}^2 + \hat{g}^2} + (\Delta U_{sc}^{shape})^2\right]^{-1/2} + B_A \tag{5.6a}$$

and

$$\varphi_{btf}(f, f_{m,sc}^{\pm}, \sigma_{lon}^{\pm}, B_\phi) = \arctan\left(\frac{\mp\hat{g}}{\mp\hat{f} - \Delta U_{sc}^{shape}(\hat{f}^2 + \hat{g}^2)}\right) + B_\phi, \tag{5.6b}$$

respectively. Eq. 3.75 provides $\hat{f} + \mathrm{i}\hat{g}$ for a Gaussian momentum distribution. Measured amplitudes and phases with the fits are presented together with the corresponding stability diagrams in Fig. 5.4 and Fig. 5.5.

On the lower side and at low intensity, the model agrees well with the BTF. A strong deformation is observed for the high-intensity beam. The model complies with the high-intensity data only roughly. The amplitude with its sharp maximum indicates a larger ΔU_{sc}^{shape} than the phase does. The spike close to the resonance of the phase can not be reproduced by the linear space-charge model with a Gaussian distribution. However, the stability diagram is described reasonably well and the shift due to space-charge is obvious.

The high-intensity stability diagram on the lower side is affected by noise, particularly on the right side. There are two reasons for this noise. One reason is related to

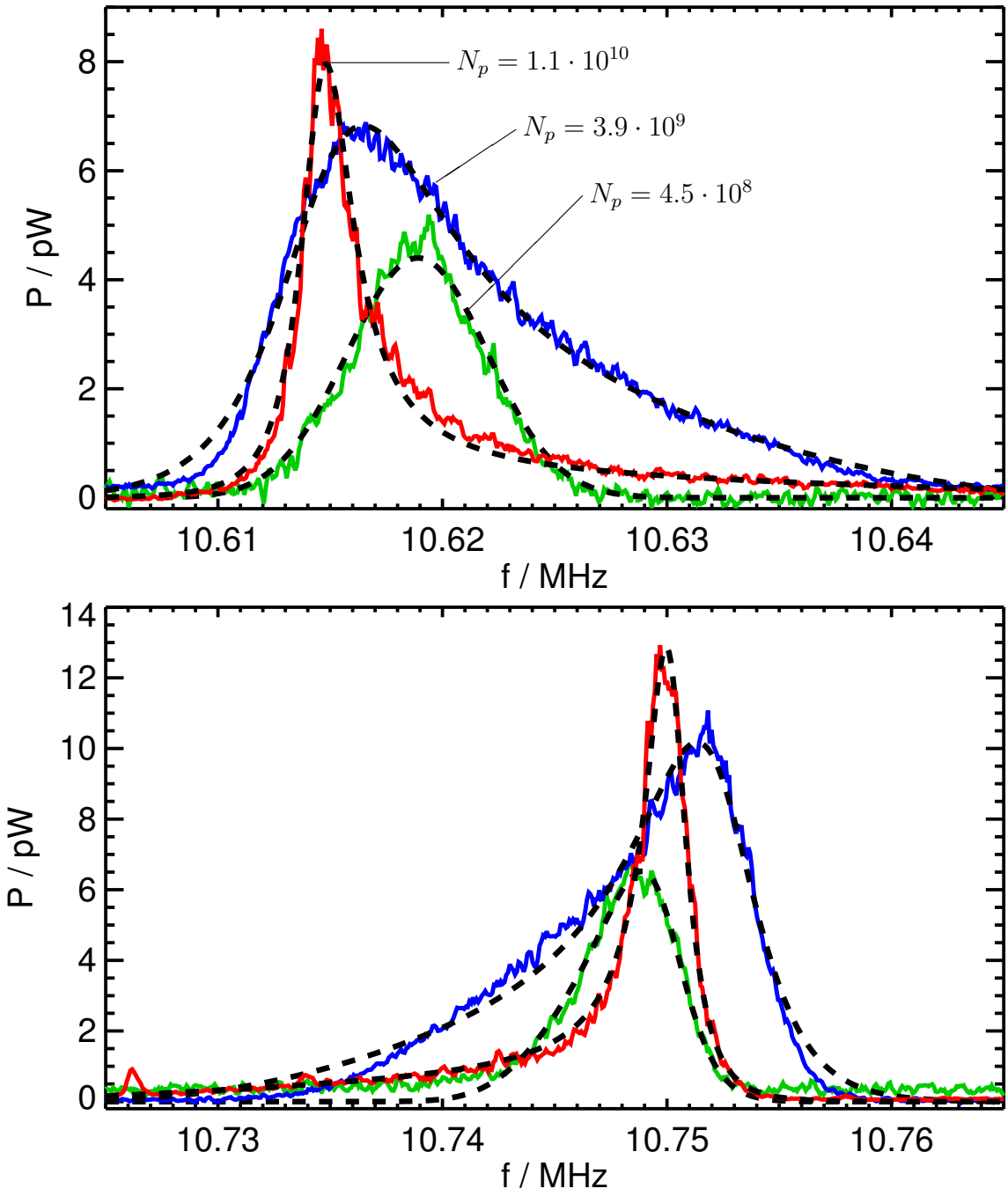

Figure 5.3: Lower and upper Schottky bands at $m = 50$ with different beam intensities. The data were smoothed to reduce the noise. The bands corresponding to $N_p = 2.5 \cdot 10^8$ and $N_p = 3.9 \cdot 10^9$ are magnified to give a better prospect.

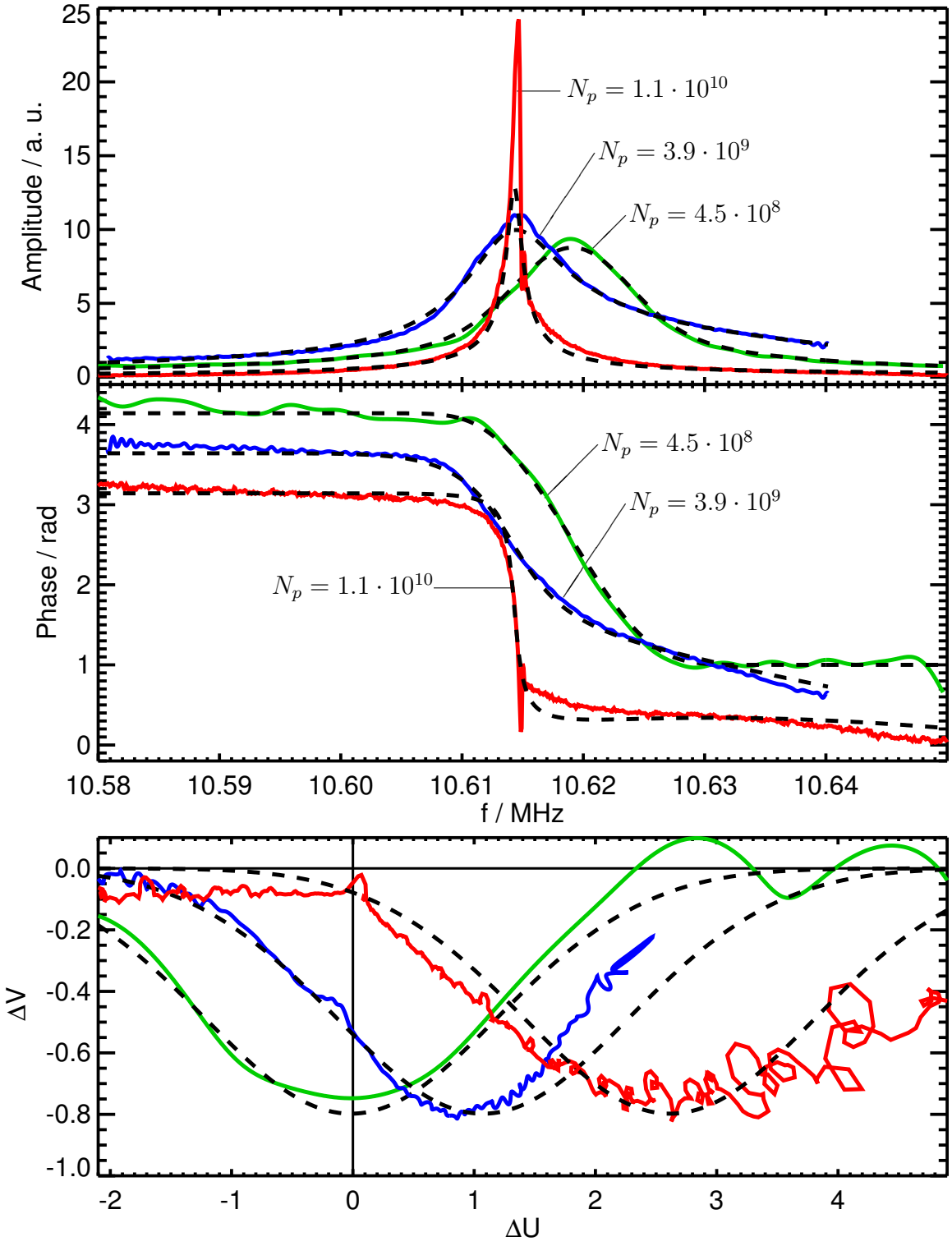

Figure 5.4: Amplitude and phase of BTFs measured at the lower side band after time gating and after the adjustment of the phase. The amplitudes are rescaled and the phases are shifted vertically for a better view. On the bottom the stability diagrams are shown. The high intensity stability diagram was constructed with smoothed data.

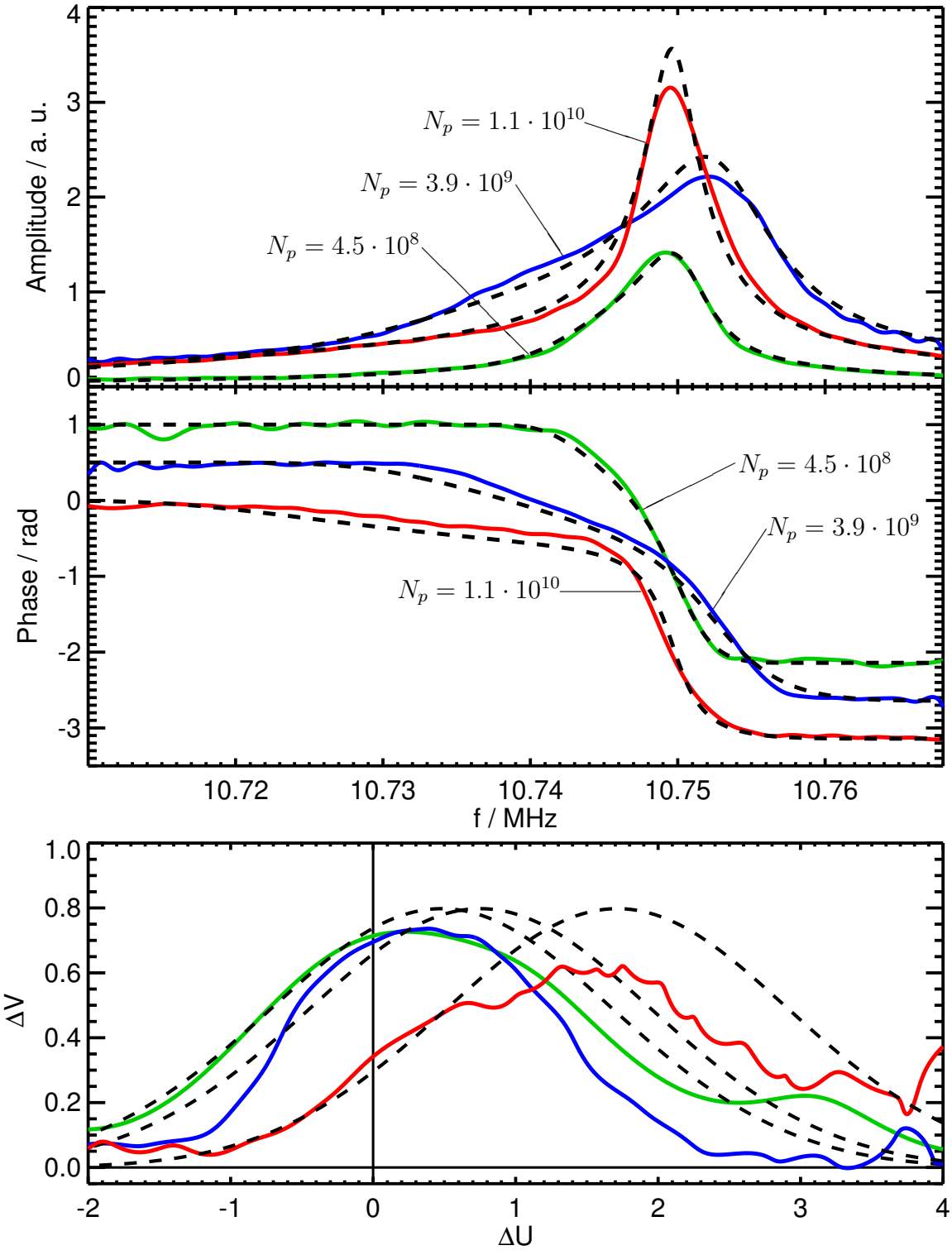

Figure 5.5: BTFs measured on the upper side after time gating and after the adjustment of the phases. The amplitudes are rescaled and the phases are shifted vertically for a better view. On the bottom the stability diagrams are shown.

the evaluation of the stability diagram. When the amplitude is inverted for the construction of the stability diagram, the noise in the regions of a low signal is amplified. At low intensity, when the maximum of the amplitude and the active region of the stability diagram correspond to the same frequency, this does not cause a problem. However, Δf_{sc} shifts the resonance frequency $f^{\pm}_{m,sc}$ away from the maximum of the BTF. Therefore the minimum of the noise on the stability diagram does not coincide with the range of maximal damping anymore, but with the region around the V axis, where the noise is visibly lower.

The other reason is the spiky shape of the amplitude and the phase which gives rise to high-frequency Fourier components. These overlap with the noise so that the noise can not be efficiently erased without significantly deforming the signal. The Fourier transform of the BTF is closely related to the response of the beam to a kick (shock response) [4]. Physically the longer tail of the response in the time domain can be interpreted as a suppressed damping rate due to space charge.

A further complication for the determination of the high-intensity stability diagrams arises from the deformation of the phase. The slower convergence towards the asymptotes makes the identification of the phase drift and the offset rather difficult. Even a small offset strongly distorts the stability diagram. On account of this, the phase offset was fine-tuned with regard to the orientation of the stability diagram.

On the upper side, the BTF is asymmetric at low intensity but the deformation at high intensity is much weaker than on the lower side. The curves are smooth relative to the lower side. Similar to the Schottky data, the BTF at medium intensity is shifted with respect to the others. The stability diagrams are less noisy than on the lower side because the smoother shape does not generate high-frequency Fourier components limiting the efficiency of the time gating. However, the stability diagrams are distorted and shifted less than expected.

A superior agreement between the model and the experiment was demonstrated for the Schottky data. However, the discussion so far was based on qualitative arguments only. In the next section the fit parameters characterizing the collective effects are discussed.

5.3 Comparison

In this section, the tune and the collective parameters derived from the fit and from the beam parameters are compared quantitatively. The estimation of the uncertainty of all parameters can be found in App. B. The bare tune can be read directly from $Q_f = |f^{\pm}_m - f_m|/f_0$ at low intensity. The fractional part of the tune from the measurements of the two least-intense beams,

$$Q_{ref} \equiv 0.301, \tag{5.7}$$

is defined as reference for the bare tune.

The deformation parameter ΔU^{shape}_{sc} (Eq. 5.4) is obtained directly from the fitting

procedure. The incoherent tune is gained from

$$Q_{sc}^{shift} \equiv \pm \frac{f_{m,sc}^{\pm} - f_m}{f_0} \tag{5.8}$$

and allows us to determine the space-charge tune-shift

$$\Delta Q_{sc}^{shift} \equiv Q_{ref} - Q_{sc}^{shift}. \tag{5.9}$$

According to the estimation in Sec. 5.1, $\Delta U^{\pm}$ is negligible which implies $\Delta U_{sc}^{shape} = \Delta U_{sc}^{shift}$. In order to verify the consistency of the measurement we consider the difference

$$\Delta U_{sc}^{gap} \equiv \Delta U_{sc}^{shift} - \Delta U_{sc}^{shape}. \tag{5.10}$$

Using Eq. 3.97a we calculate

$$\Delta Q_{sc}^{gap} = \Delta U_{sc}^{gap} \frac{\sigma_{lon}^{\pm}}{f_0}. \tag{5.11}$$

For an estimation of the incoherent tune based on measured beam parameters only, we evaluate

$$Q_{\epsilon} \equiv Q_{ref} - \Delta Q_{\epsilon}, \tag{5.12}$$

where ΔQ_{ϵ} is defined in Eq. 5.1.

In Sec. 5.1, ϵ_y was found to be almost constant, so that the space-charge effect is proportional to N_p in a good approximation. Therefore the measured tunes are presented as a function of N_p in Fig. 5.6. As expected ΔQ_{sc}^{shift} decreases linearly with increasing N_p. Nevertheless there are remarkable discrepancies between the results of the different measuring methods and between the lower and upper side band. ΔQ_{ϵ} is smaller than ΔQ_{sc}^{shift}, especially for the BTF on the lower side, with $\Delta Q_{\epsilon}/\Delta Q_{sc}^{shift} \approx 50\,\%$. On the upper side, the deviation between Q_{sc}^{shift} and Q_{sc}^{ϵ} is roughly as large as the measuring uncertainty. On the lower side, we find $\Delta Q_{sc}^{gap} \approx 0$, as expected. However, on the upper side, the Schottky bands yield $\Delta Q_{sc}^{gap}/\Delta Q_{sc}^{shift} = 13\,\%$ and the BTFs $\Delta Q_{sc}^{gap}/\Delta Q_{sc}^{shift} = 25\,\%$.

The space-charge parameters are plotted in Fig. 5.7. Eq. 3.97a was applied to calculate $\Delta U_{sc}^{shift} = \Delta Q_{sc}^{shift} f_0/\sigma_m^{\pm}$ and ΔU_{sc}^{ϵ} analogously. On the lower side, ΔU_{sc}^{shape} and ΔU_{sc}^{shift} are very close to each other, while a remarkable deviation from ΔU_{sc}^{ϵ} is found, being again more pronounced in the BTF. On the upper side a only small discrepancy between ΔU_{sc}^{shape} and ΔU_{sc}^{shift} is observed. Comparing the slopes reveals that ΔU_{sc}^{shape} is 12 % smaller than ΔU_{sc}^{shift} according to the Schottky and 31 % according to the BTF data. This is similar to the ratio of ΔQ_{sc}^{gap} to ΔQ_{sc}^{shift}. However, the deviation is not much larger than the measuring uncertainty.

For decreasing intensity, ΔU_{sc}^{gap} and ΔU_{sc}^{shift} do not converge towards 0. The deviation of ΔU_{sc}^{shape} stems from a small asymmetry of the momentum distribution, also indicated in the longitudinal Schottky bands (Fig. 5.1). In contrast to the space-charge effect this deformation is not mirror inverted between the upper and the lower side, and therefore pretends negative values on the lower side. Also ΔU_{sc}^{shift} differs

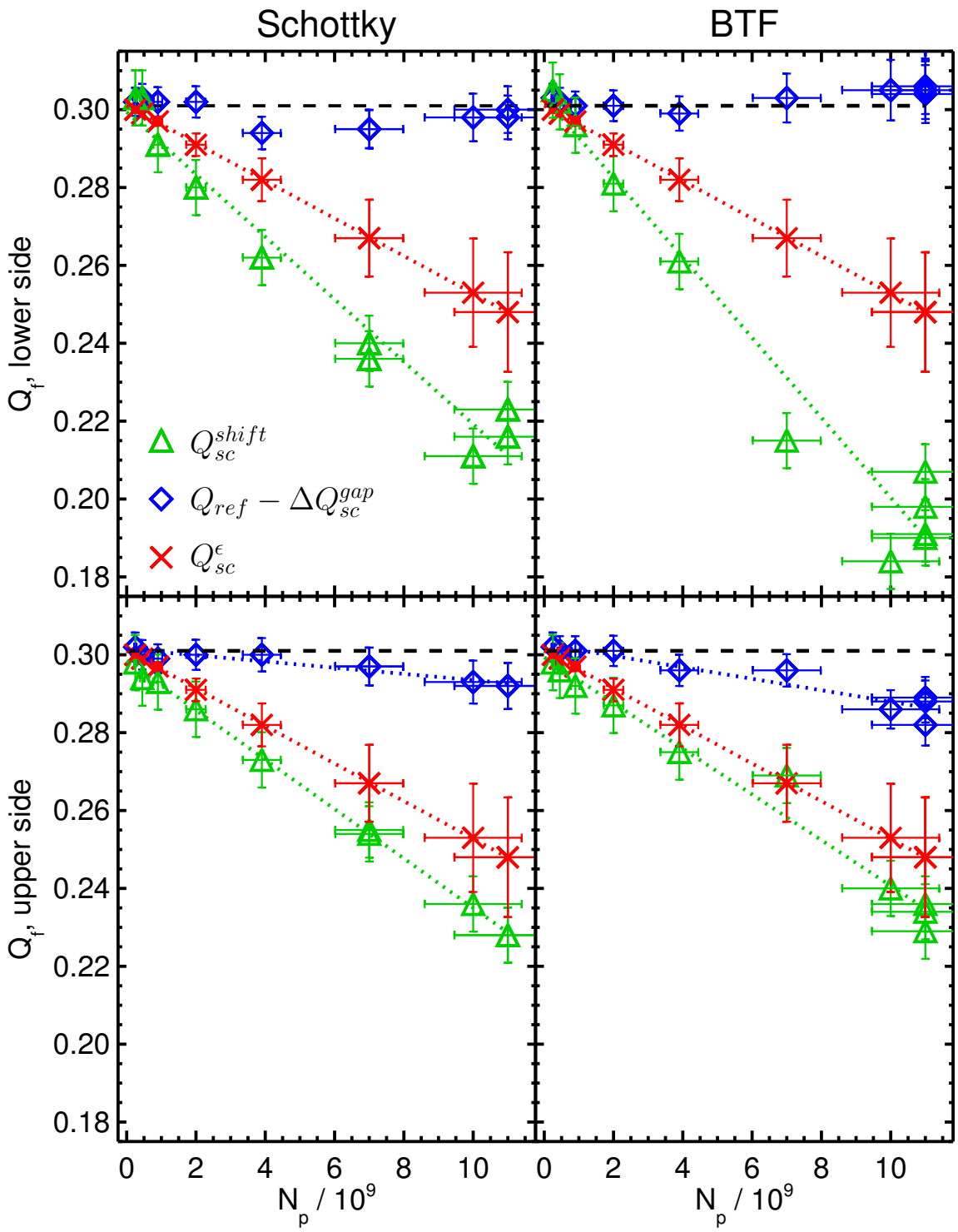

Figure 5.6: Tunes as a function of N_p, measured at the lower and upper side band of the harmonic $m = 50$. Schottky and BTF measurements are plotted separately as well as the lower and the upper side band. Green triangles indicate Q_{sc}^{shift}, red crosses represent Q_ϵ, and blue diamonds indicate $Q_{ref} - \Delta Q_{sc}^{gap}$. The dashed line marks Q_{ref}. Dotted lines are fits to the data. A fit to $Q_{ref} - \Delta Q_{sc}^{gap}$ was done only for the upper side.

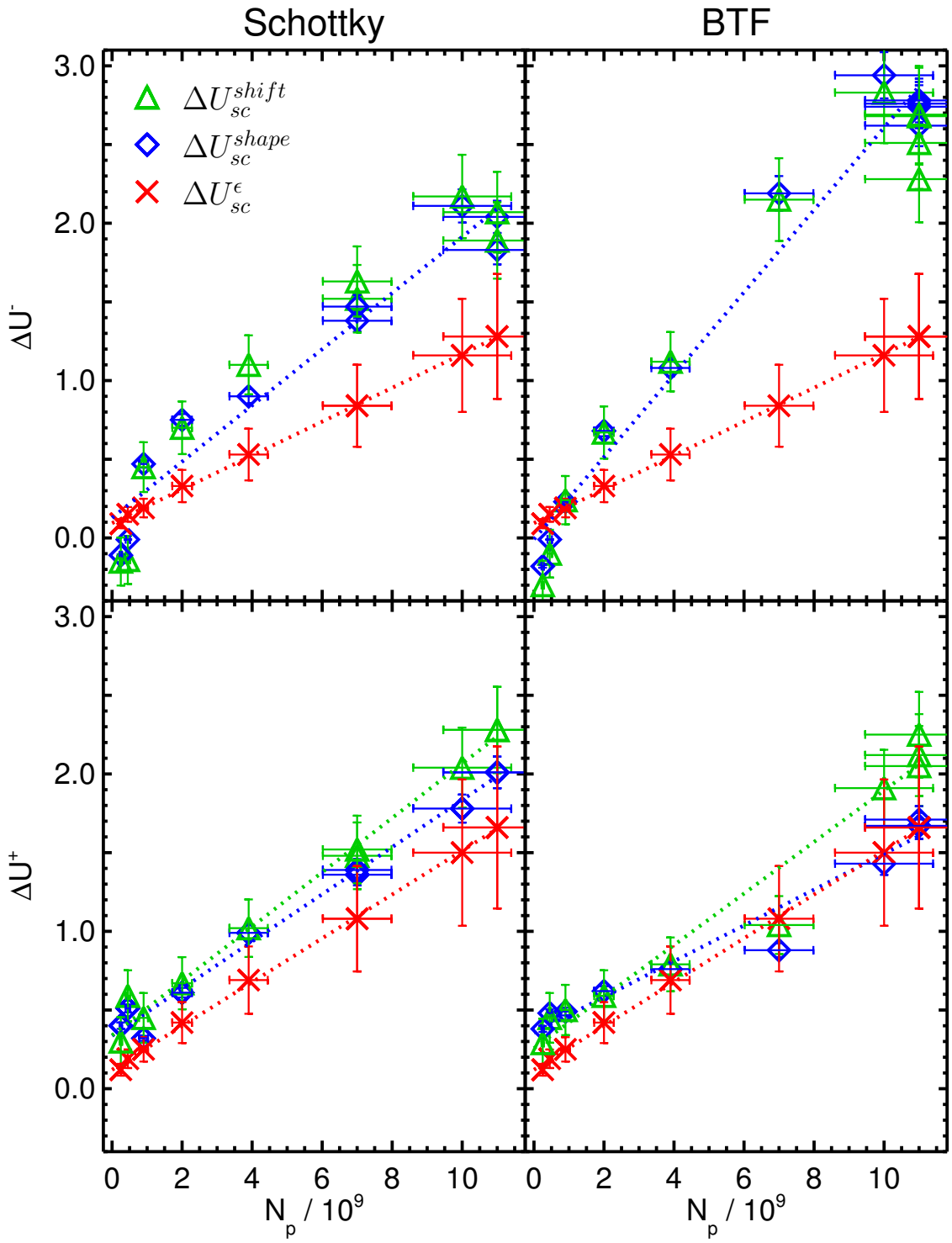

Figure 5.7: Space charge parameters obtained from the Schottky and BTF measurements at the lower and upper side band of $m = 50$. Blue diamonds represent ΔU_{sc}^{shape}, green triangles ΔU_{sc}^{shift} and red crosses ΔU_{sc}^{ϵ}. Fitting lines of ΔU_{sc}^{shape} and ΔU_{sc}^{ϵ}, as well as ΔU_{sc}^{shift} for the upper side, are indicated by dotted lines.

from 0 at low intensity because the values of ΔQ_{sc}^{shift} do not exactly coincide with Q_{ref}. Compared to Q_{ref}, these deviations are small but due to the small momentum spread at low intensity, the deviation of ΔU_{sc}^{shift} is enlarged.

In summary, discrepancies between the Schottky spectra, the BTF data and the estimation with the beam parameters were detected on the lower side. ΔQ_{sc}^{shift} is consistent with ΔQ_{sc}^{shape}, though the values obtained from the Schottky data differ from those found with the BTF. ΔQ_{sc}^{ϵ} is smaller in both measurements. Similar observations are made with the corresponding space-charge parameters.

On the upper side, ΔQ_{sc}^{shift} and ΔQ_{sc}^{shape} differ from each other. The impedance of SIS-18 is assumed to be much too small to cause this effect. Furthermore the frequency of the upper side band is less than 150 kHz above the lower side band where no discrepancy was observed. The deviation is larger according to the BTFs than according to the Schottky spectra. On the other hand, ΔQ_{sc}^{shift} and ΔU_{sc}^{shift} are closer to ΔQ_{sc}^{ϵ} and ΔU_{sc}^{ϵ}, respectively, and the deviation between the Schottky data and the BTF data are small. Compared with the lower side, the values are small at high intensity.

The reason for the observed deviations remained unclear. Possibly the assumption of a Gaussian momentum distribution contributes to the disagreement. Even though this assumption is approximately correct, the small asymmetry actually present pretends a deformation of the low intensity signals. It was assumed that the high intensity signals were only negligibly perturbed, but the actual impact was not studied. Concerning the BTFs, it is also possible that the high-intensity beams did not reach a stable state fast enough for the measurement due to collective effects. The estimation of the space-charge effect is unreliable particularly because of the questionable state of the IPM and the fact that $\hat{\beta}_{ipm}$ was calculated only. The actual value may differ because of imperfections in the accelerator. For instance, closed orbit deformations have been shown to affect $\hat{\beta}$ [90].

The question whether the space-charge model produces unphysical results can be addressed by simulations. Also the uncertainty of the physical parameters is thereby avoided. The code for the simulation of Schottky spectra and BTFs is the subject of the next chapter. But before, an experiment supporting the measurement of the real impedance of SIS-18 is presented.

5.4 Chromaticity Measurement

The sensitivity of the transverse Schottky bands and BTFs to real impedances is too low to be resolved with the beams available in SIS-18. In addition the BTF may not yield reliable results close to instabilities because the beam does not reach a stationary state fast enough for a measurement. An alternative method to determine the real impedance present in the machine is the measurement of the growth time τ of an instability. Eq. 3.84b then yields $\mathrm{Re}(Z_{\perp})$. Such measurements have been carried out in SIS-18 [70].

For this purpose an instability is induced by decreasing the width of the lower side band of the harmonic $m = 1$. The low harmonic number is chosen because the

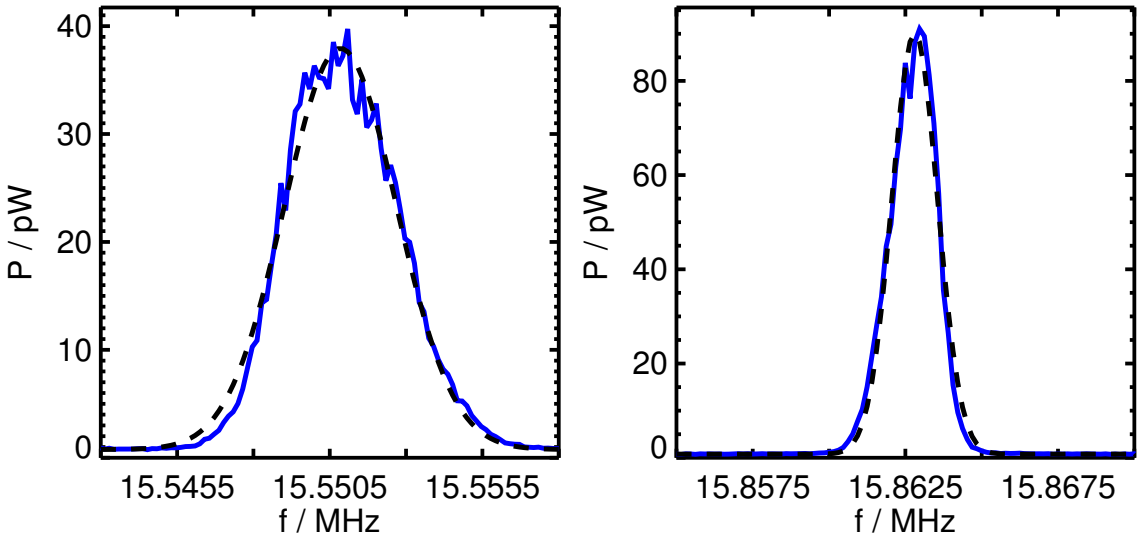

Figure 5.8: Couple of horizontal side bands at 200 MeV/u. Note that the displayed span is equal in both figures.

resistive wall impedance is strongest at low frequencies. The width of the lower side band is minimized by setting

$$\xi = -\eta \frac{1 - Q_f}{Q} \tag{5.13}$$

by virtue of SIS-18's 12 sextupoles. The control system of SIS-18 allows one to set ξ, but the correctness the setting was questionable. After an experiment failed to induce a coherent beam instability, beam time was allocated to assess ξ with and without sextupoles.

ξ can be detected directly via Schottky diagnostics. From Eq. 3.56 it follows

$$\xi = \left(m \frac{\sigma_m^+ - \sigma_m^-}{\sigma_m^+ + \sigma_m^-} - Q_f \right) \frac{|\eta|}{Q}. \tag{5.14}$$

This was done successfully with a $^{132}Xe^{48+}$ beam at 200 MeV/u. A pair of side bands is plotted in Fig. 5.8. The difference between the widths is evident. Applying Eq. 5.14 to the bands measured in both planes yielded $\xi_y = -2.29$ and $\xi_x = -1.32$. Calculations with a beam optics code (MADX) predicted remarkably different values, namely $\xi_y = -1.66$ and $\xi_x = -1.65$ [91]. The reason for the discrepancy is still under investigation.

With the method discussed above, ξ can be determined with little effort. However, its use in SIS-18 is limited to beams with an energy of some hundred MeV/u as a consequence of the limitation of the pick-up to frequencies above 10 MHz. At injection energy, this implies $m \geq 50$ so that ξ contributes only marginally to $\sigma_m^{\pm}$. For this reason the measuring uncertainty of ξ is unacceptably high.

Therefore, for the measurement at injection energy, another technique, employing the electron cooler in SIS-18 [37, 38], was applied. In the cooler, an electron beam follows the orbit of the ion beam with the electron speed adjusted to the velocity

of the ions. The electrons, being much lighter than the ions, absorb most of the transverse momentum and σ_p in collisions. Hence the random motion of the ions is damped — the beam is cooled.

Mismatching the energy of the electron beam, so that the ions move a few per mill slower or faster, changes the mean energy of the beam. This way the energy is varied without changing the magnetic fields of the accelerator. The regular acceleration with the radio frequency cavities could not be used because the control system automatically adapts the magnets to the higher rigidity of the beam. $f_m^{\pm}$ is tracked with Schottky measurements while the mean momentum $p = p_0 - \Delta p$ is varied with the cooler. From Eq. 3.49 one obtains

$$f_{0,k} = \frac{f_{m,k}^{+} + f_{m,k}^{-}}{2m} \tag{5.15}$$

and

$$Q_{f,k} = \frac{f_{m,k}^{+} - f_{m,k}^{-}}{2f_0}, \tag{5.16}$$

where k is the index referring to one electron energy. The values from one arbitrary measurement are defined as references, $f_{0,ref}$ and $Q_{f,ref}$. Subtracting the reference values from $f_{0,k}$ and $Q_{f,k}$, respectively, yields $\Delta f_{0,k}$ and $\Delta Q_{f,k}$. Then, with Eq. 3.6, Δp_k is calculated from $\Delta f_{0,k}/f_0$. The slope of a straight line fitted to $\Delta Q_{f,k}/Q$ as a function of Δp_k is ξ according to Eq. 3.17.

As a result of the first experiment, the electrical connections of the sextupoles were checked and one sextupole was found to be polarized wrongly [91]. After the correction of this error, the experiment was repeated. The measured values ξ_{meas} are plotted versus the set values ξ_{set} in Fig. 5.9. The dashed line corresponds to an equity between the measurement and the setting. In the horizontal plane the chromaticity is affected weaker by the sextupoles than expected. In the vertical plane the measured values are smaller by about 0.4 than the set ones.

The deviation is likely related to the cooler needed for the measurement. The cooler has magnets to ensure that the ion beam and the electron beam do not miss each other. In addition there is a solenoid which gives rise to a coupling between the transverse planes. It is unclear whether the control system handles the modification of the lattice due to the cooler correctly.

Furthermore during the experiment it turned out that the procedure to correct the closed orbit [55] could not be applied with the cooler in operation. Consequently the orbit was not well defined. Closed orbit deformations may be responsible for the observed discrepancy. Recently it was demonstrated that orbit deformations lead to errors of $\hat{\beta}$ [90] which may modify the effectiveness of the sextupoles by virtue of Eq. 3.19.

Further investigations are needed to determine ξ precisely. Nevertheless, the measurement was able to discover a problem with the sextupoles. After the correction of the electric interconnections, coherent beam-instabilities were observed in a dedicated experiment [92].

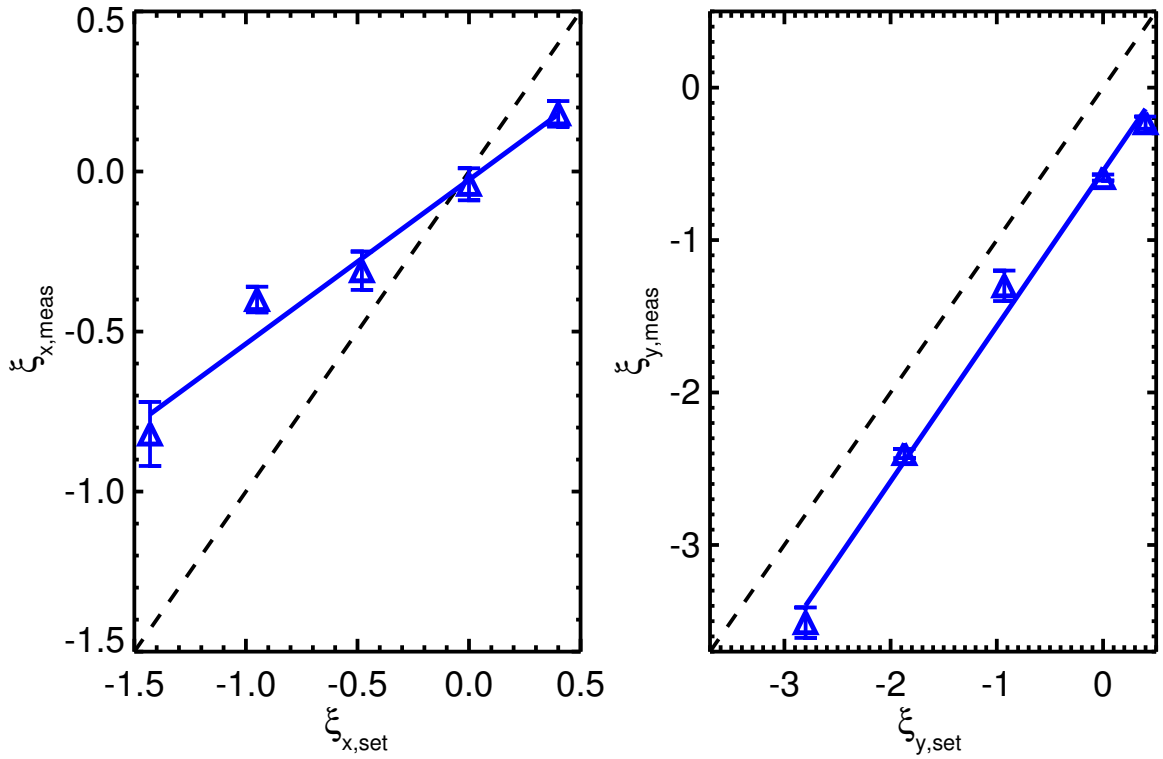

Figure 5.9: Measured chromaticities at injection versus setting.

5.5 Summary of measurements

Transverse Schottky and BTF measurements, dedicated to the investigation of collective effects, were accomplished in SIS-18. Longitudinal Schottky spectra, the particle number and beam profiles were acquired as well, to comprehend all beam parameters of interest. As opposed space charge, impedances were not expected to affect the beam remarkably for the given beam parameters.

An intensity dependent deformation of the transverse Schottky bands and BTFs was observed. The stability diagrams constructed from the BTFs are shifted at high beam-intensity. The linear space-charge model was fitted to the data. For the Schottky bands, a good agreement was found, while the high-intensity BTFs are described only approximately. The space-charge tune-shift ΔQ_{sc} and the space-charge parameter ΔU_{sc} were determined from the deformation and from the position of the signals. In addition the beam parameters were used to estimate ΔQ_{sc} and ΔU_{sc}. As expected, the impact of space-charge increases with increasing beam intensity. However, the values obtained from different methods differ. A detailed explanation for the deviations was not found.

In order to support the detection of coherent transverse beam instabilities and for other purposes, the chromaticity ξ in SIS-18 was measured via Schottky diagnostics. The measured values differ from the set ones. Although the reasons for the stated discrepancies are not fully understood, the measurements helped to find a technical error in SIS-18.

Chapter 6

Simulations

Simulations provide an alternative approach to investigate physical phenomena and to test analytic models. Compared to an experiment, the parameters of interest can be controlled better and undesired physical effects can be excluded. The model assumptions, however, have to be applied with care, to create a model reproducing the physical effects being the subject of interest.

A code for the simulation of the transverse dynamics of a coasting beam with space charge and imaginary impedances was developed in this work. Its task was the computation of transverse Schottky spectra and BTFs, analogously to signals obtained from measurements in an accelerator. The results can be used to test our understanding of the measurements and for the verification of the linear space-charge model. The code was implemented in the C++ programming language [93].

The code was written in order to simulate Schottky spectra and BTFs with collective effects as efficiently as possible. The beam optics is reduced to a constantly focusing field. The self-field of the beam is computed self-consistently in every time step and the fluctuation of the dipole moment, the Schottky noise, is tracked.

Since Schottky noise is based on the fluctuation of the beam's dipole moment, the proper initialization of the particle distribution is crucial. In order to improve the signal quality, it should be possible to average the output of several simulations with equal beam and grid parameters. Therefore it is important to produce the same mean particle-distributions with different noise in subsequent runs. Furthermore, for the studies presented in this work, it was necessary to provide the options to include or exclude space-charge effects, impedance effects and a beam excitation for the BTF simulations. All these requirements were included in the code.

In this chapter the function of the code is described. The computational model and its implementation are the topic of Sec. 6.1. The output of the code is discussed in Sec. 6.2, before in Sec. 6.3 appropriate parameters for the simulations are considered. An estimation of the image currents present in the model follows in Sec. 6.4. It is shown that the effect of the image currents requires only a small correction of the results for an adequately chosen grid.

6.1 Computational model

For the numerical computation of Schottky spectra and BTFs, the space and the time variables in the equation of motion are discretized. The longitudinal steps have the length $\Delta s = v\Delta t$ and are termed $s_n \equiv n\Delta s$. The limitation to coasting beams allows us to simplify the computations in various ways. Firstly, the self-field has no longitudinal components. Hence the field needs to be calculated only in the transverse plane, which reduces the number of dimensions to two. Secondly, with the exception of fluctuations, the self-field is constant in time and $|\vec{B}| = v/c^2|\vec{E}|$. This implies that the magnetostatic field needs not to be evaluated explicitly, but can be implicitly included in the force by $(\vec{E} + \vec{v} \times \vec{B}) = \vec{E}/\gamma^2$, as explained in Subsec. 3.3.2.

Thirdly, the average particle number in a beam disc is independent of s. Therefore we consider a number of *macro particles* N_m in one disc and scale the field to the demanded strength with a virtual *macro charge*. As a consequence of this simplification, there are no longitudinal fluctuations and the code will produce only one side band located around f_β. For our purposes this is adequate. Another side effect is that the width of the side band (Eq. 3.56) gets no contribution from m and η so that ξ has to be included in our model to give the band a finite width.

For the calculation of the self-field, a 2-dimensional square grid with the coordinates $(\tilde{x}_k, \tilde{y}_l)^T$ and the indices k, l running from 0 to $N_g - 1$ is defined, where N_g^2 is the *number of grid cells*. The size of the grid is termed l_g. Codes where the fields are computed on a grid forming cells around the particles are standard tools for computer simulations and are known as *particle in cell* codes [94]. Direct particle interactions like collisions are not included in the code presented here.

The scheme of one computation cycle is illustrated in Fig. 6.1. A simulation starts with the initialization of the beam. According to the input from a configuration file, the particles are distributed randomly in the phase space. The beams were given a Gaussian longitudinal momentum distribution and K-V or Gaussian transverse phase-space distributions. When referring to two dimensions, the precise term for the latter is bi-Gaussian, but here we simply call it Gaussian, knowing that the particle distribution of any beam discussed here is equal in the x and in the y direction. The longitudinal position is the same for all particles for the reason discussed at the beginning of this section.

The routines generating distributions of random numbers were taken from Ref. [95] or PATRIC [96]. These routines redistribute a given set of uniform random numbers to produce the demanded distributions. The uniform random numbers are provided by a random number generator. The generation of these numbers is started with a so-called seed. This seed can be adjusted for each simulation to ensure that a sequence of random numbers does not repeat inadvertently [95].

From the distribution of the particles, the charge density ρ on the two dimensional grid is interpolated via

$$\rho(\tilde{x}_k, \tilde{y}_l, s_n) = \frac{Z_m e}{C(\Delta x_g)^2} \sum_{j=1}^{N_m} S[x_j(s_n), y_j(s_n)], \tag{6.1}$$

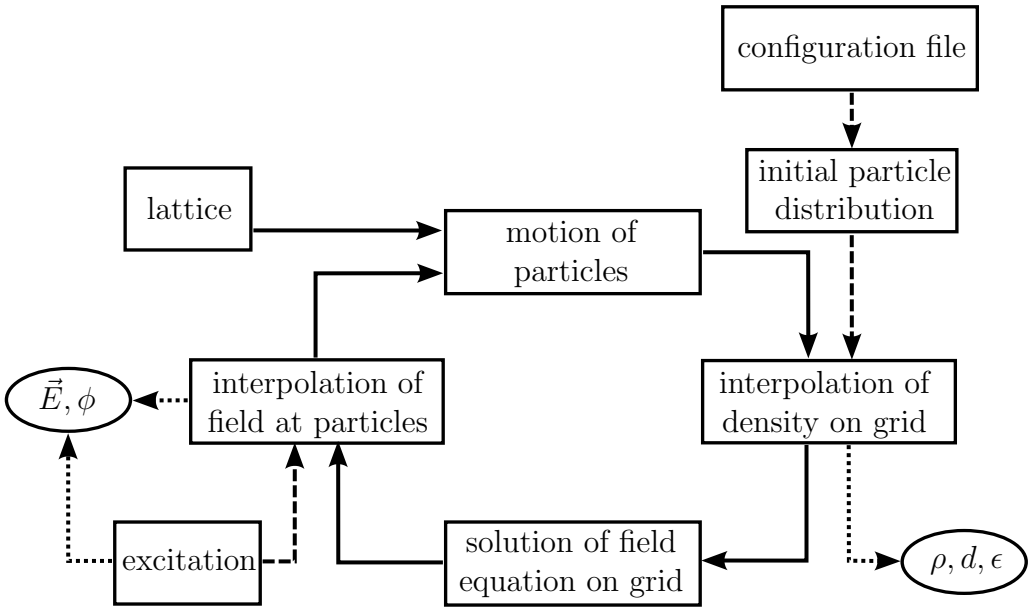

Figure 6.1: Computation cycle of a Schottky or BTF simulation. The simulation starts with the initialization of the beam according to a configuration file. Then the computation of the field and the motion of the particles follow each other with interpolations in between. The dashed arrow starting at the excitation refers to BTF simulations only. The output of the program is indicated with the dotted arrows.

where we introduced the macro charge Z_m, the grid spacing $\Delta x_g \equiv \Delta y_g = l_g/N_g$ and the linear interpolation function $S(x_j, y_j)$. S distributes the charge of each particle onto the four grid points of the surrounding cell. C is the length of the beam. The discretized Poisson's equation is solved by virtue of a discrete Fourier transform and its inverse, as discussed in Ref. [94]. Fast Fourier transforms and their application to solve partial differential equations are elaborated in Ref. [95]. In this implementation a sine transform is applied implying that the boundary is a perfect electric conductor — which is a good approximation for the surface of a beam pipe. The consequence of this assumption is the topic of Sec. 6.4.

The solution of the discrete Poisson's equation yields the electric potential that is numerically differentiated in space to gain the electric field on the grid, $\vec{E}_{sc}(\tilde{x}_k, \tilde{y}_l, s_n)$. An interpolation yields the self-field experienced by the particles,

$$\vec{E}_{sc}(x_j, y_j, s_n) = \tilde{S}[\vec{E}_{sc}(\tilde{x}_k, \tilde{y}_l, s_n)], \tag{6.2}$$

where $\tilde{S}$ interpolates the field from the four grid points forming the cell around the particle. The grid points are determined by the conditions $\tilde{x}_k \leq x_j < \tilde{x}_{k+1}$ and $\tilde{y}_l \leq y_j < \tilde{y}_{l+1}$. For a linear interpolation, the field at $(\tilde{x}_k, \tilde{y}_l, s_n)$, weighted with $(\tilde{x}_{k+1} - x_j)(\tilde{y}_{l+1} - y_j)/(\Delta x_g)^2$, and the fields at the other three points, weighted correspondingly, are summed up to obtain $\vec{E}_{sc}(x_j, y_j, s_n)$. The field associated with an

impedance corresponding to a given ΔU reads

$$E_{imp,x}(s_n) = \frac{4\pi c m_p A}{eZR}\beta\gamma Q\sigma_m^{\pm}\Delta U\bar{x}(s_n), \tag{6.3}$$

where

$$\bar{x}(s_n) = \frac{1}{N_m}\sum_{j=1}^{N_m} x_j(s_n) \tag{6.4}$$

is the offset of the beam's barycenter.

In the case where a BTF is to be simulated, the exciting field,

$$E_{btf}(s_n) = \frac{E_0}{\sqrt{N_f}}\sum_{i=1}^{N_f}\sin\left(\frac{\omega_i s_n}{v} + \phi_i\right), \tag{6.5}$$

is added to the self-field in the corresponding plane. The exciting frequencies, ω_i, are distributed equidistantly around f_β in the range of several σ of the Schottky band. The random phases, ϕ_i, impart E_{btf} characteristics of white noise for sufficiently large N_f. The field amplitude E_0 is to be chosen such that the response of the beam is distinct from the fluctuations of d, but small enough that the beam is only weakly perturbed. A significant growth of the beam size indicates that E_0 is too large. The action of the electric fields during one time step is approximated by an instantaneous change of the transverse momentum,

$$x_j'(x_j, y_j) = \frac{eZ\Delta s}{E_p\beta^2\gamma^3 A}E_x(x_j, y_j), \tag{6.6}$$

where $E_p = m_p c^2$ is the proton rest energy.

The transport through the lattice is calculated efficiently by virtue of the matrix formalism introduced in Subsec. 3.1.1. The lattice is reduced to a constant focusing channel so that the transport matrix, Eq. 3.16, needs to be evaluated only once for both planes at the beginning of a simulation. However, a complication arises from the fact that the chromaticity ξ has to included in our model. Without chromaticity the Schottky band would reduce to a line because we did not take the spread of the revolution frequencies into account. In order to include ξ, we plug Eq. 3.17 into $\Delta Q = -Q/\hat{\beta}\Delta\hat{\beta}$, which results from Eq. 3.24, to obtain

$$\hat{\beta}_j = \hat{\beta}\left(1 - \xi\Delta p_j\right). \tag{6.7}$$

The transport matrix then reads

$$M_{j,x,x'} = \begin{pmatrix} \cos(\Delta s/\hat{\beta}_{x,j}) & \hat{\beta}_{x,j}\sin(\Delta s/\hat{\beta}_{x,j}) \\ -1/\hat{\beta}_{x,j}\sin(\Delta s/\hat{\beta}_{x,j}) & \cos(\Delta s/\hat{\beta}_{x,j}) \end{pmatrix}, \tag{6.8}$$

where we set $l = \Delta s$. This implies that each particle has its own transport matrices $M_{j,x,x'}$ and $M_{j,y,y'}$. The computational drawback is bearable, though, since they have to be evaluated only once.

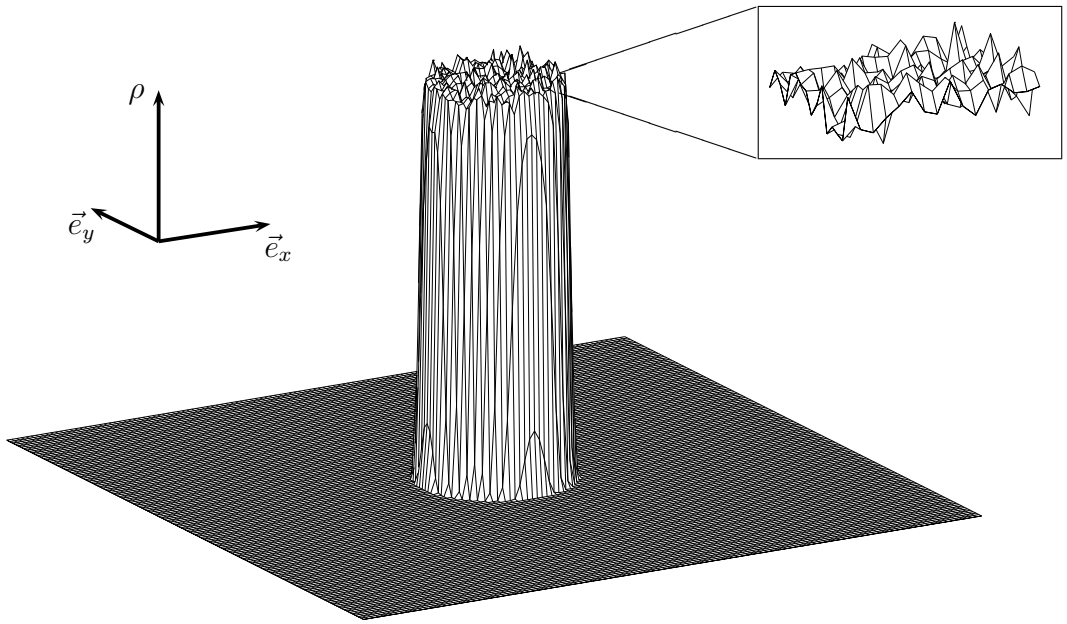

Figure 6.2: Simulated charge density of a K-V beam. The inset magnifies the particle density in the beam and emphasizes the noise due to the random distribution of the particles.

6.2 Simulation output

The output of a simulation is indicated in Fig. 6.1. The self-field $\vec{E}_{sc}(\tilde{x}_k, \tilde{y}_l, s_n)$, the electric potential $\phi(\tilde{x}_k, \tilde{y}_l, s_n)$ and the charge density $\rho(\tilde{x}_k, \tilde{y}_l, s_n)$ on the grid are only needed for benchmarking. This output was compared with the analytic distributions in order to verify its correctness. The simulated charge distributions and electric fields of a K-V and a Gaussian beam are shown in Fig. 6.2–6.4.

$d(s_n)$, $a(s_n)$ and the excitation field $E_{btf}(s_n)$ are recorded after the initialization of the beam and after each time step for both planes. The evolution of the horizontal rms beam radius

$$a_x(s_n) = \sqrt{\frac{1}{N_m}\sum_{j=1}^{N_m}[x_j(s_n) - \bar{x}(s_n)]^2} \tag{6.9}$$

is tracked to make sure that the initial beam size is adequate and to verify that the emittance is approximately constant, apart from fluctuations. This is particularly important if the beam is excited for a BTF simulation. The targets of the simulation are to compute the current dipole-moment

$$d_x(s_n) = eZ_m f_0 \bar{x}(s_n) \tag{6.10}$$

and eventually the excitation given by Eq. 6.5. For $E_0 = 0$

$$P_x(f) \equiv |\mathcal{F}\{d_x(s_n)\}|^2 \tag{6.11}$$

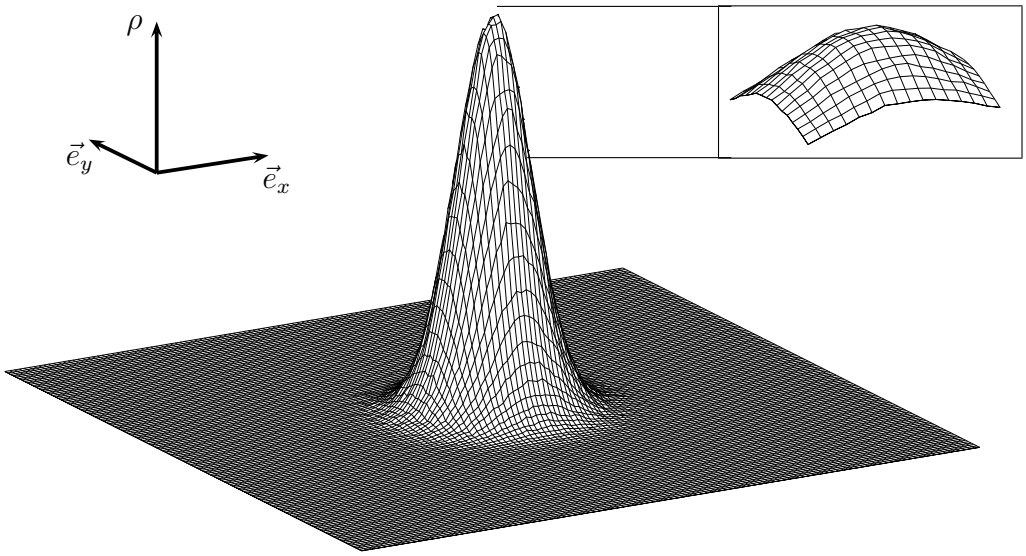

Figure 6.3: Simulated charge density of a Gaussian beam. The inset magnifies the density close to the maximum. The noise appears to be lower than in the K-V beam but actually the vertical scale of the inset is larger because of the varying density.

is the horizontal Schottky spectrum of the beam, while for $E_0 \neq 0$

$$r_x(f) \equiv \frac{\mathcal{F}\{d_x(s_n)\}}{\mathcal{F}\{E_{x,btf}(s_n)\}} \tag{6.12}$$

yields the horizontal BTF. These equations are also applicable to the vertical plane.

Mathematica® scripts were written to evaluate P and r via a fast Fourier transform and then to average over all data sets from simulations with equal beam parameters to reduce the noise. The analytic models, Eq. 5.2 and Eq. 5.6, are compared to $P(f)$ or $|r(f)|$ and $\arg[r(f)]$, respectively. Optionally a smoothing procedure, replacing each data point by the mean value of itself and its neighbors, can be applied. However, since smoothing may affect the shape of signals, particularly if they are strongly non-linear, it should be used with caution.

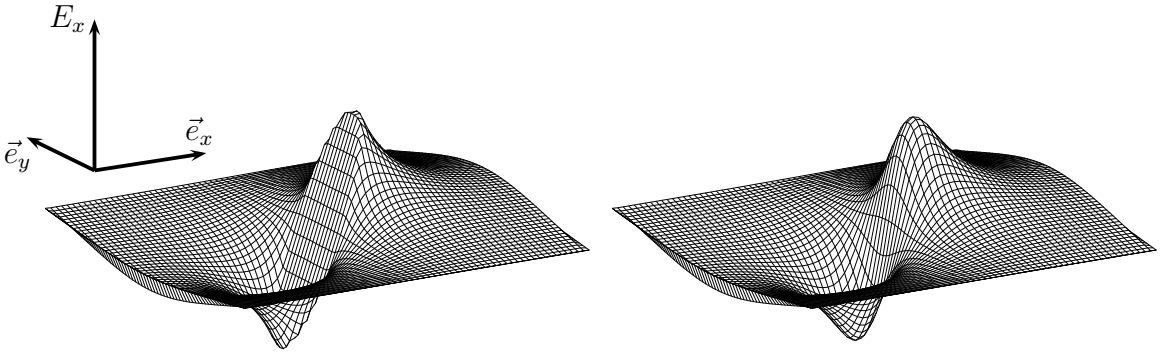

Figure 6.4: Simulated self-field of a K-V and a Gaussian beam. Within the K-V beam, the field is linear. The field of the continuous Gaussian beam is approximately linear close to the center and changes smoothly with increasing radius.

6.3 Settings

The discretization of the variables of interest must be fine enough to resolve the effects under examination. First of all, the target of the simulations, i. e. the Schottky band or BTF, must be resolved well enough to allow a comparison with the model. The number of points N_b within the $2\,\sigma$ width of the Schottky band,

$$w_{sim} = 4 f_0 Q |\xi| \sigma_p, \tag{6.13}$$

is given by

$$N_b = N_s \frac{2Q|\xi|\sigma_p \Delta s}{C}, \tag{6.14}$$

where the *number of time steps* N_s is introduced. The corresponding simulation time $T = N_s \Delta s / v$ is consequently given by $T = N_b/(2Q|\xi| f_0 \sigma_p)$. Note that due to the deformation at high intensity, the band becomes narrower so that Eq. 6.14 is not useful anymore. The simulations were performed with the natural chromaticity of a constant focusing channel $\xi = -1/2$, obtained from Eq. 3.18 using Eq. 3.27 and Eq. 3.24.

A reproduction of the transverse dynamics requires to resolve the betatron oscillation (Eq. 3.26). This is particularly important for the space-charge effect since it depends on the self-field at the position of the particle. The number of steps per oscillation reads

$$N_\beta = \frac{C}{Q \Delta s}. \tag{6.15}$$

From Eq. 6.14 and Eq. 6.15, it follows that $N_s = N_b N_\beta / (2|\xi|\sigma_p)$. Concretely the values $N_b \approx 40$ and $N_\beta \approx 60$ were used in the simulations presented in Chap. 7. With $N_s = 524288$ and $\sigma_p = 5 \cdot 10^{-3}$ the simulation period covers about 8000 betatron oscillations.

For the simulation of space-charge effects, the particle number, N_m, and the number of grid cells, N_g^2, have to be adjusted such that the number of particles per cell is much larger than 1,

$$N_m \frac{\Delta x_g^2}{\pi a^2} \gg 1, \tag{6.16}$$

to keep the noise on a moderate level. For a Gaussian beam this applies only to a part, say $2a$, of the beam. Theoretically a too large N_m would suppress the Schottky noise but in practice N_m is limited by the computation time. On the other hand

$$\frac{\Delta x_g}{a} \ll 1 \tag{6.17}$$

is required to resolve the self-field spatially. Finally

$$\frac{a}{l_g} \ll 1 \tag{6.18}$$

limits the perturbation of the self-field due to the boundaries. However, this effect can be included in our model, as discussed in Sec. 6.4.

In our lattice the transverse planes are decoupled from each other and coupling due to space-charge effects may cause only minor perturbations at the beam intensities studied here. Therefore we may set the horizontal and vertical parameters pairwise equal, including $\hat{\beta}_x = \hat{\beta}_y$. Then each simulation returns two data sets corresponding to the same beam parameters. Statistically the two resulting data sets are uncorrelated, because of the uncorrelated initial distributions. The benefit is that we can take the average of the two data sets to reduce the noise.

Simulations were carried out with different numerical and physical parameters yielding different simulation times, resolutions in time, space and frequency, and noise levels. It was verified that the simulations reproduce the physical properties of transverse Schottky bands and BTFs. The beam was also observed in the time domain and single test particles were tracked. In addition to the considerations discussed in this section, these parameter studies lead to the choice of the final parameters mentioned above.

6.4 Estimation of image charges

As mentioned in Sec. 6.1, the field was computed from the charge density via a sinus transformation, implying a vanishing electric field on the boundaries of the grid. Physically this implies that the beam is surrounded by a perfectly conducting beam pipe with image currents on its surface. For a circular beam pipe with radius b and a circular beam with a rms radius, a, we learned in Subsec. 3.3.2 that ΔQ_{sc} exceeds ΔQ by $4a^2/b^2$.

Since the grid is in fact rectangular, the impedance differs slightly. The impedance of a rectangular beam pipe can not be expressed by means of fundamental functions, but numerically [4]. Tune shifts in circular and rectangular beam pipes are discussed in Ref. [97]. Therein, the impedance attributed to a rectangular beam pipe with an edge length $2b$ is 9 % lower than the impedance of a circular pipe with radius b for a centered beam. Therefore we write

$$\Delta U / \Delta U_{sc} \approx 3.6 \left(\frac{a}{l_g} \right)^2 \tag{6.19}$$

With the simulation parameters $l_g = 5\,\mathrm{cm}$ and $a = 2.65\,\mathrm{mm}$ this yields

$$\frac{\Delta U}{\Delta U_{sc}} = 4\,\%. \tag{6.20}$$

Hence space charge is clearly the dominating collective effect.

Chapter 7

Simulation results

The code discussed in Chap. 6 was written as a part of this work to investigate space-charge effects in transverse Schottky spectra and BTFs by virtue of numerical simulations. Beams with K-V and Gaussian profiles are considered. The comparison of the linear space-charge model with the K-V beam simulations tells us how well the model describes a beam with a linear self-field. In particular the simulation does not rely on the rigid beam approximation mentioned in Subsec. 3.3.2. On the other hand, an agreement between the model and a simulation with a linear space charge verifies the correctness of the code and confirms that the simulation parameters are chosen appropriately. From the simulation of the Gaussian beams we learn how the model complies with a non-linear self-field.

Twenty simulations were run for each macroscopic setting, differing by the random numbers in the initial distributions only. The noise is significantly reduced by taking the average of the resulting spectra or BTFs. Nevertheless, the data were slightly smoothed (range ± 1) afterwards.

Eq. 5.2 was fitted to the simulated Schottky spectra with the fit parameters A, B and ΔU_{sc}^{shape}. The latter was necessary to determine the contribution of the image currents. σ_p, f_β and ΔU_{sc}^{shift} did not need to be fitted because they were defined by the settings of the simulations. $u_{sc}^{\pm}$ was determined using the half of w_{sim} (Eq. 6.13) instead of $\sigma_{lon}^{\pm}$. After the fitting process, the data were normalized by subtracting B and dividing by A. Similarly the amplitudes and phases of the simulated BTFs were fitted to Eq. 5.6a and Eq. 5.6b, respectively.

The simulated Schottky spectra are shown in Fig. 7.1 for $\Delta U_{sc}^{shift} \in [0, 1, 2]$. The BTFs follow in Fig. 7.2 and Fig. 7.3. Finally the corresponding stability diagrams are presented in Fig. 7.4. In all cases the model agrees excellently with the simulations. The deformations due to space charge and the shift of the stability diagrams are clearly visible. The position of the signals is reproduced by the model. No significant difference between K-V and Gaussian beams is observable.

Similarly to the stability diagrams obtained from the measurements (Fig. 5.4 and Fig. 5.5), we find a stronger superposition with noise at high intensity. As discussed in Sec. 5.2 this can be explained with the construction of the stability diagrams. Hence this problem is not attributed to the experimental setup but is a feature of stability diagrams with collective effects.

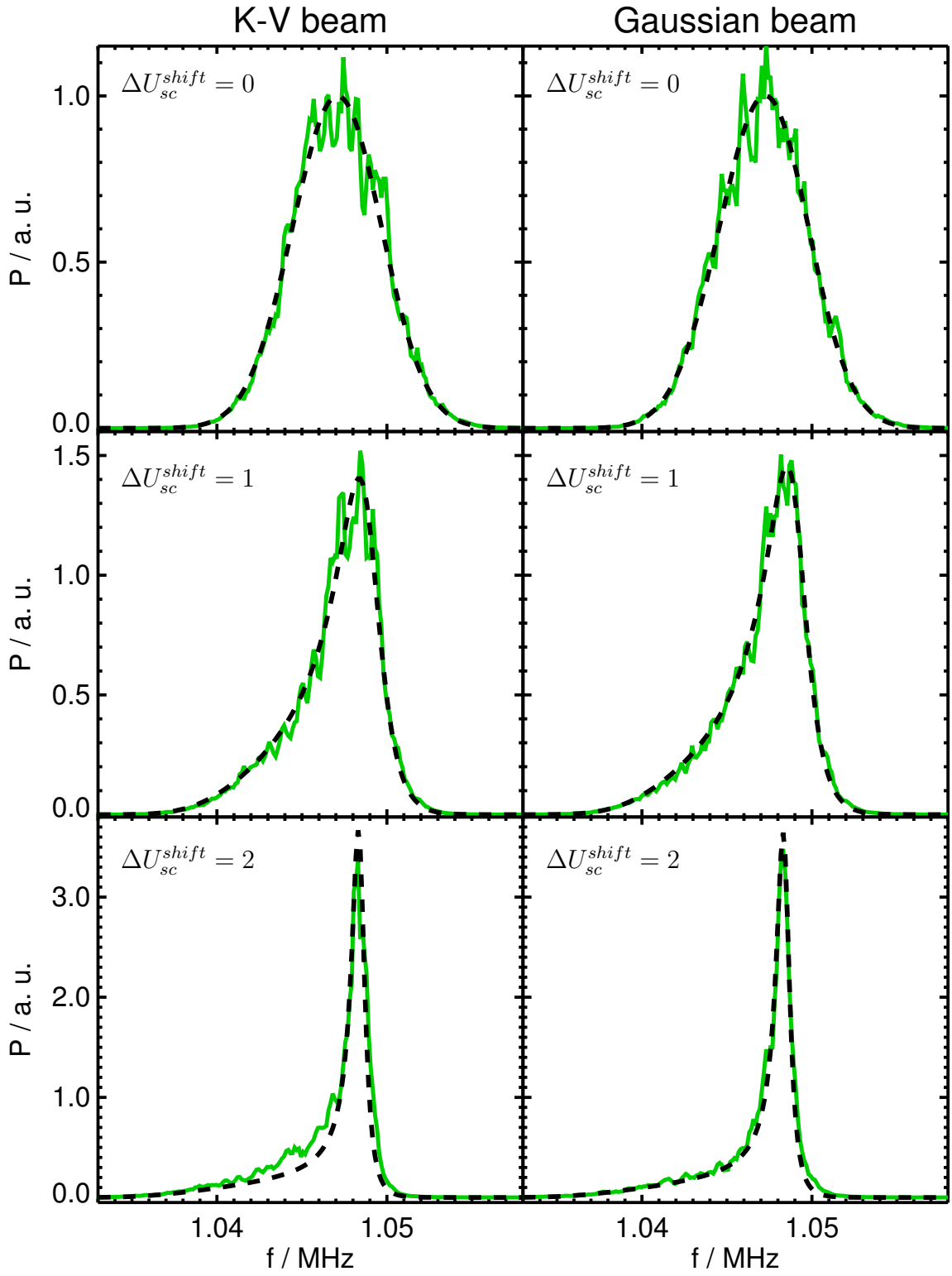

Figure 7.1: Simulated Schottky spectra of K-V and Gaussian beams with different ΔU_{sc}^{shift} (solid) and the fitted model (dashed). All data sets are scaled to $A = 1$.

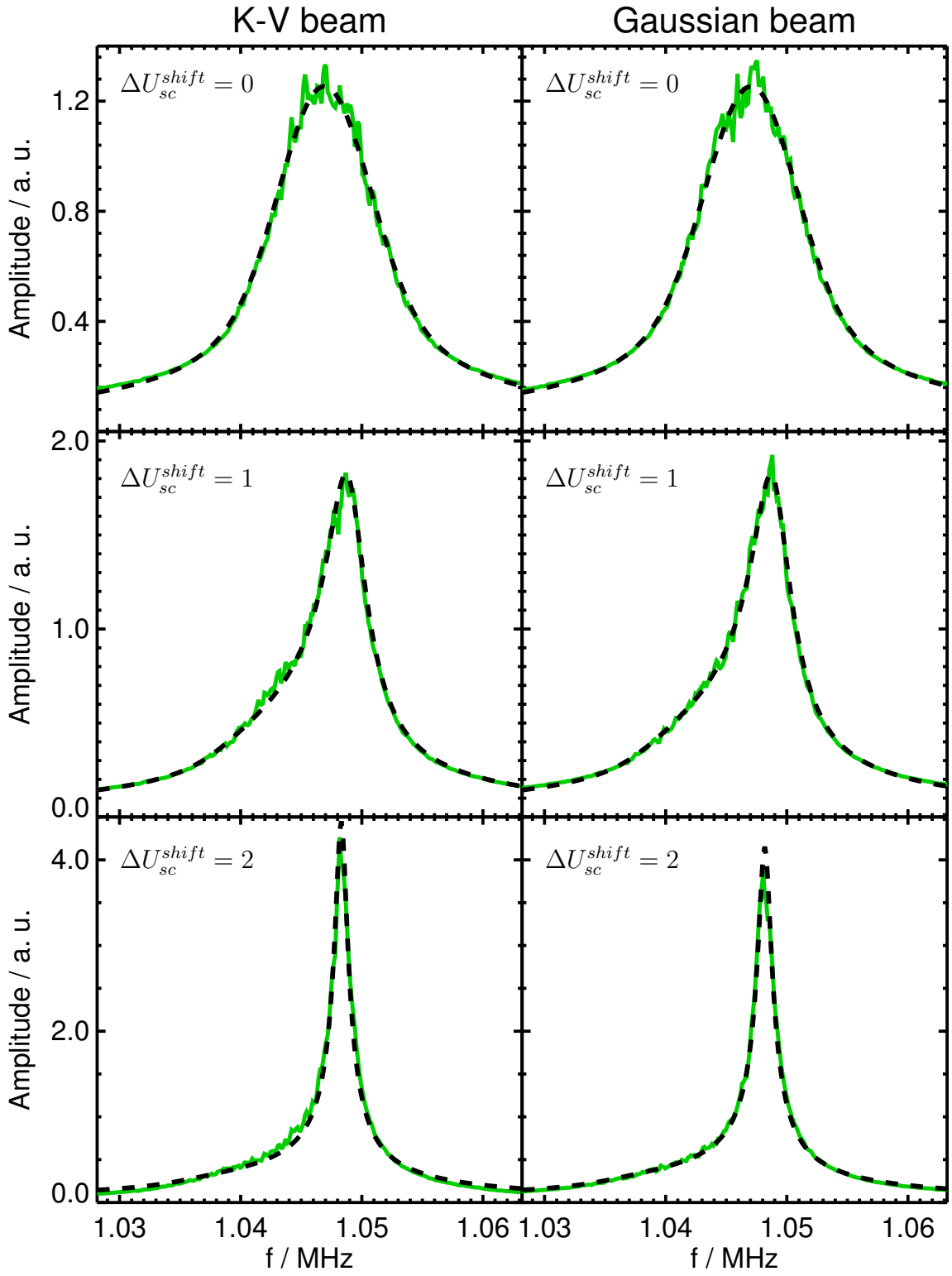

Figure 7.2: Simulated BTF amplitudes of K-V and Gaussian beams with different ΔU_{sc}^{shift} (solid) and fitted model (dashed). All data sets are scaled to $A = 1$.

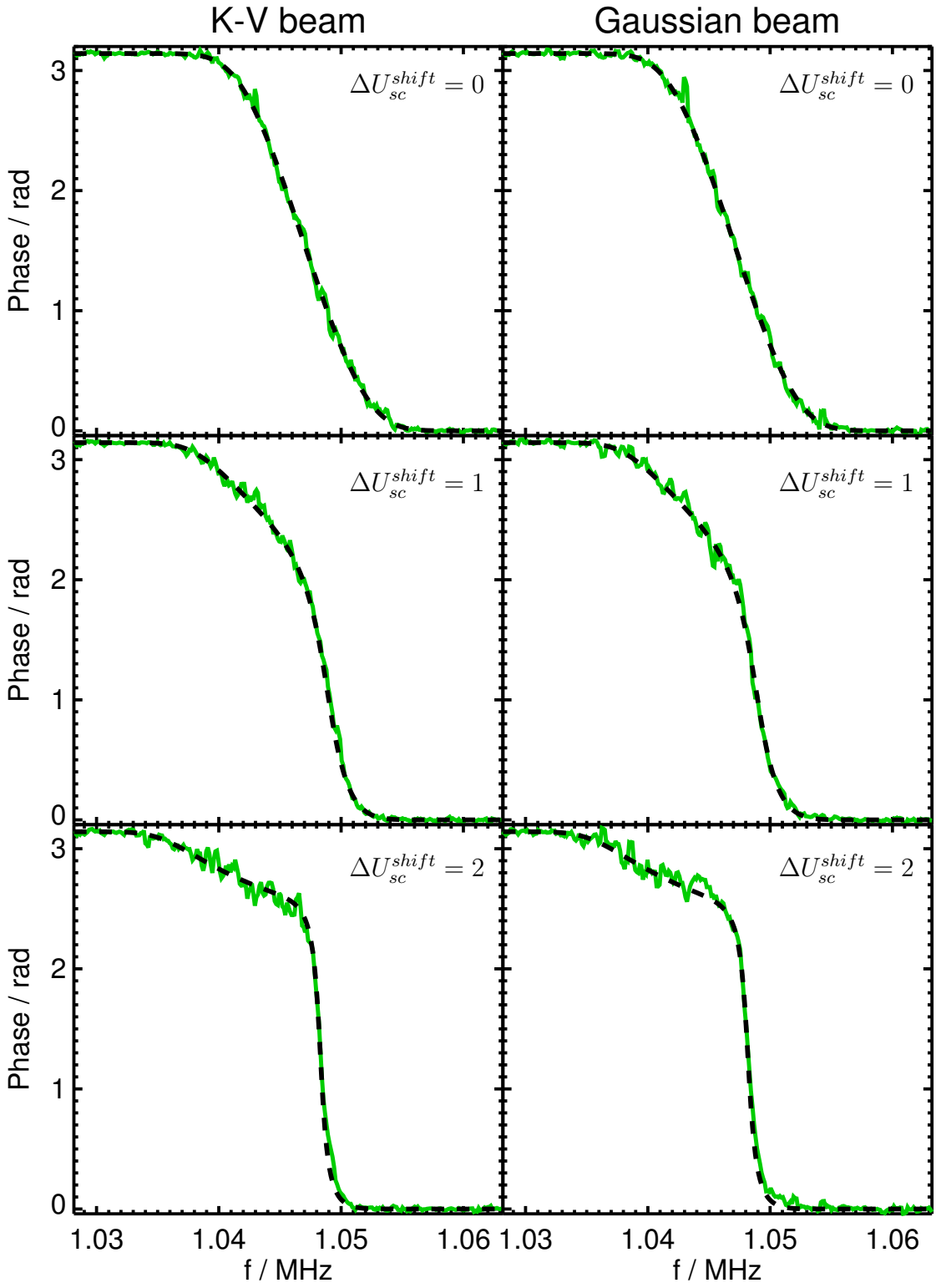

Figure 7.3: Simulated BTF phases of K-V and Gaussian beams with different ΔU_{sc}^{shift} (solid) and the fitted model (dashed).

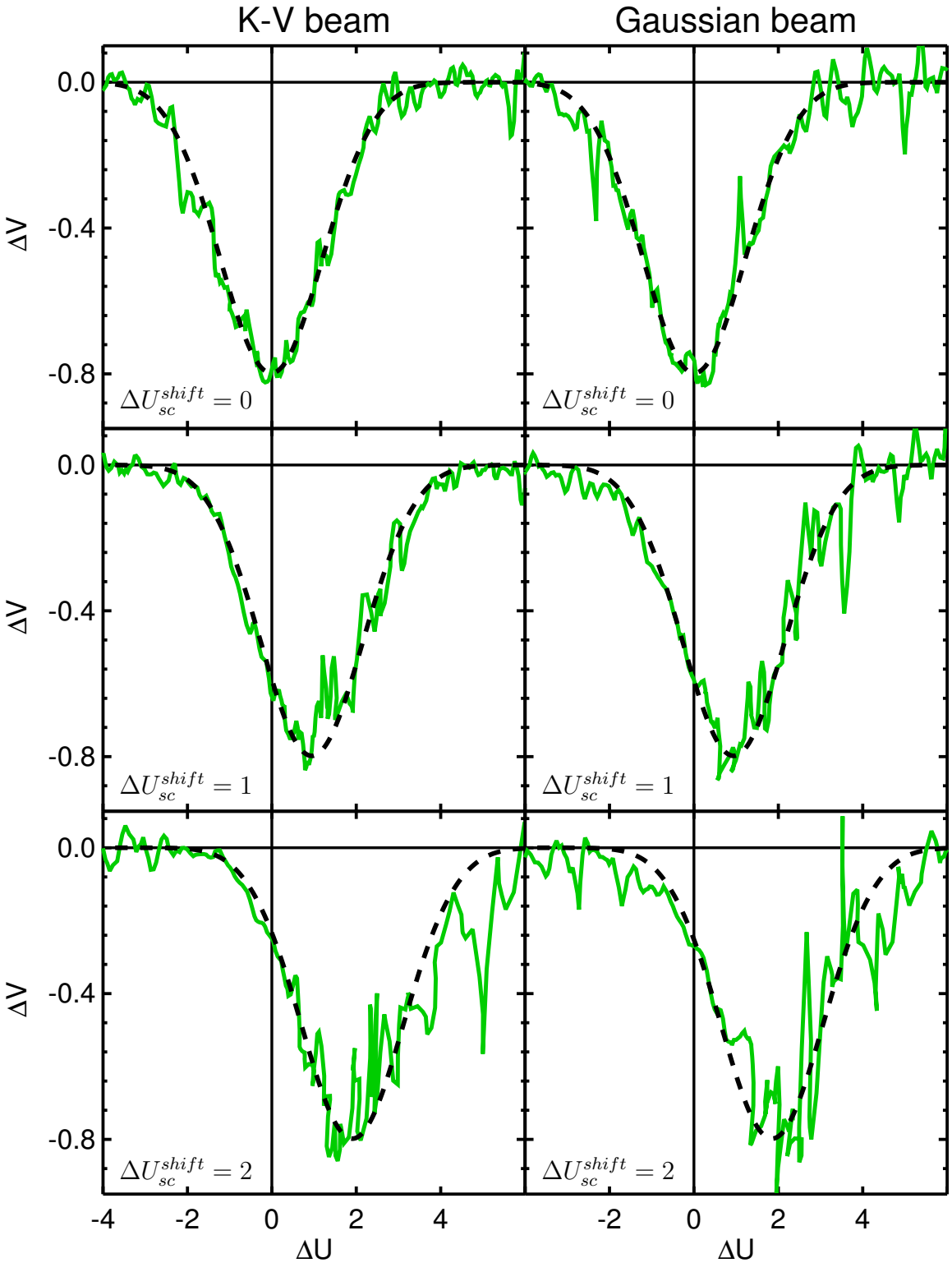

Figure 7.4: Stability diagrams corresponding to the simulated BTFs (solid) and fitted model (dashed).

Table 7.1: ΔU_{sc}^{shape} obtained from the fitted linear space-charge model and the corresponding ratio of image-current effects to those of space charge. The expected values were 0.96 and 1.92 for $\Delta U_{sc}^{shift} = 1$ and $\Delta U_{sc}^{shift} = 2$, respectively.

		$\Delta U_{sc}^{shift} = 0$	$\Delta U_{sc}^{shift} = 1$		$\Delta U_{sc}^{shift} = 2$	
Type	Profile	ΔU_{sc}^{shape}	ΔU_{sc}^{shape}	$\Delta U/\Delta U_{sc}^{shift}$	ΔU_{sc}^{shape}	$\Delta U/\Delta U_{sc}^{shift}$
Schottky	K-V	0.02	0.95	5 %	1.95	3 %
Schottky	Gauss	0.05	1.00	0 %	1.94	3 %
BTF	K-V	-0.01	0.95	5 %	1.91	5 %
BTF	Gauss	0.01	0.94	6 %	1.85	8 %

From the fitted deformation parameter, ΔU_{sc}^{shape}, the impact of the image currents was determined by virtue of Eq. 5.4. A list of ΔU_{sc}^{shape} and $\Delta U/\Delta U_{sc}^{shift}$ is provided in Tab. 7.1. On the average, the image currents reduce the deformation by 4 %, which is in good agreement with the estimation in Eq. 6.20. Only a small difference between Schottky and BTF data was found.

According to the linear space-charge model, space charge deforms a Schottky band or BTF in the mirror inverted way compared to an imaginary impedance of the same sign (see Eq. 3.101). In addition the maximum is moved further away by an impedance, as was demonstrated in Fig. 3.8. It is also shown there that the joint interference of space charge and an impedance with $\Delta U_{sc} = \Delta U$ lets the signal retain its original shape, but with a shift compared to the low intensity signal, due to the incoherent tune shift in $u_{sc}^{\pm}$ (Eq. 5.3).

Experimentally this situation was not studied because the impedance of SIS-18 is too small. The predictions have been verified with simulations, though. Fig. 7.5 displays the simulated Schottky bands and Fig. 7.6 the simulated BTFs with the model. In these plots, only the amplitude factor of the model was fitted. The transverse beam profiles are Gaussian.

The Schottky spectrum with $\Delta U = 2$ is deformed a bit weaker than expected. The fit yields $\Delta U^{shape} = 1.88$. A better agreement is also achieved by adapting the center frequency by 0.2 kHz. The deviation of the fit parameters from the simulation settings are larger in this case than in the other simulations. Nevertheless, the model is confirmed in good approximation. For $\Delta U = \Delta U_{sc} = 2$, the band is shifted and undeformed in agreement with the model. The BTFs and the stability diagrams match the model very well with and without space charge. Both the position and the shape reproduce the model.

Summary of simulation results

Simulations of transverse Schottky spectra and BTFs were performed with beams having Gaussian and homogeneous transverse profiles. The impact of space charge and imaginary impedances was studied separately as well as jointly. The results agree well with Eq. 3.100 and Eq. 3.106 up to $\Delta U_{sc} = 2$ and $\Delta U = 2$. Thus the simulations fully confirm the linear space-charge model for beams with moderate collective effects.

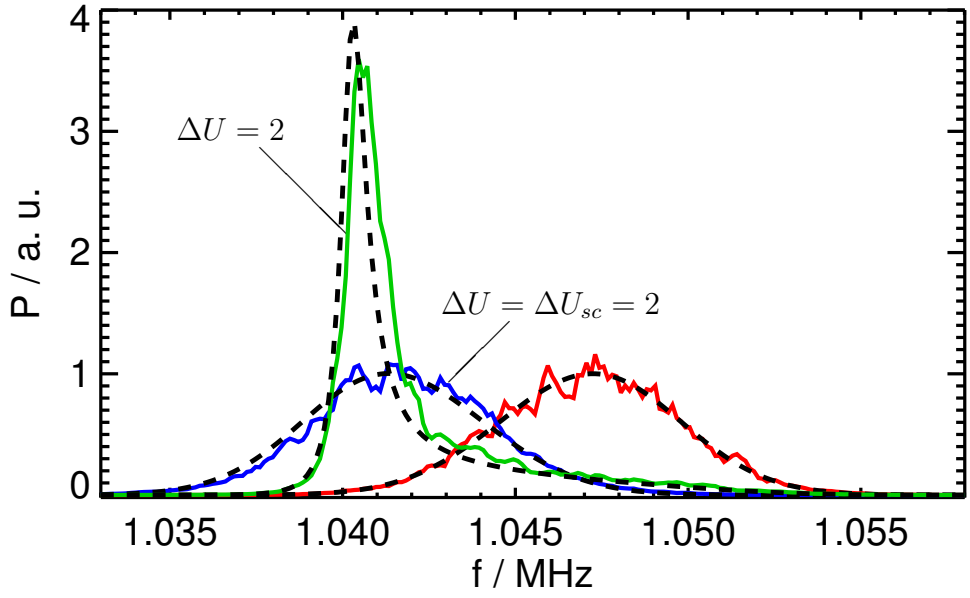

Figure 7.5: Simulated Schottky bands without collective effects, with an impedance corresponding to $\Delta U = 2$, and with $\Delta U_{sc} = \Delta U = 2$. The dashed lines correspond to the model with the simulation settings.

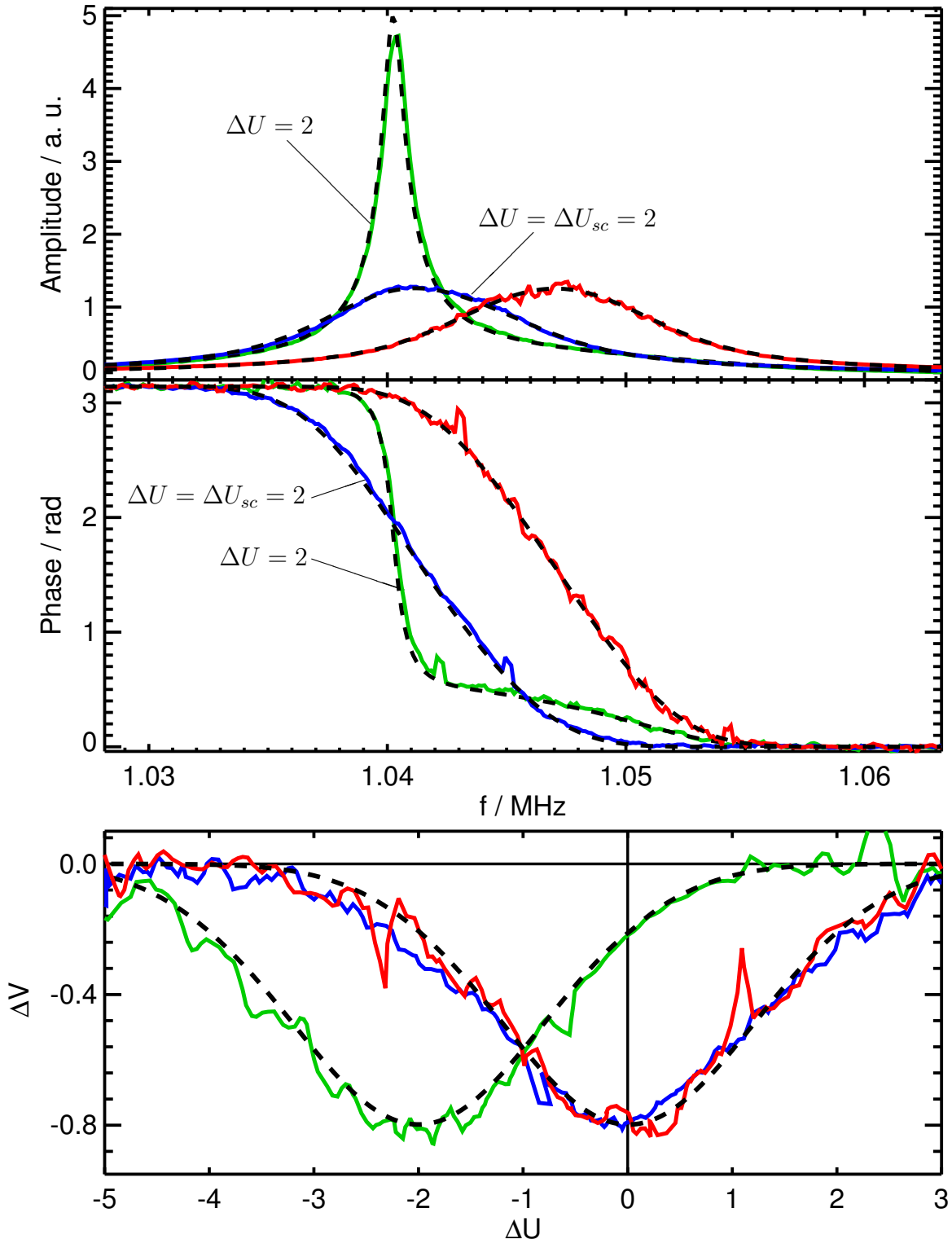

Figure 7.6: Simulated BTFs without collective effects, with an impedance corresponding to $\Delta U = 2$, and with $\Delta U_{sc} = \Delta U = 2$.

Chapter 8

Conclusions

In the present work, investigations of transverse space-charge effects in coasting ion beams are presented. Space charge is important for Landau damping, which prevents coherent dipolar instabilities, and for the diagnostics of intense beams. A model based on a linear space-charge force is used to describe space-charge effects in transverse Schottky bands and BTFs, and to evaluate the stability limits of the beam.

According to the model, both transverse Schottky bands and BTFs are deformed in a characteristic asymmetric way. For the operation of a synchrotron with high-intensity beams, the deformation leads to a problem because it prevents the transverse Schottky bands or BTFs from revealing the working point of the machine. The same deformation is produced by an imaginary dipolar impedance — with an additional shift of the signal. This is because space-charge affects the incoherent betatron oscillation of the particles while dipolar impedances exert a force on the barycenter of the beam. Incoherent higher order impedance-effects are not taken into account because they are negligible compared to the space-charge in the beams considered in this work. Comparing both the shift and the deformation of a signal allows one to distinguish the impact of space charge and an imaginary impedance. Furthermore the model states that the stability diagram is shifted equally, except the sign, by space charge and imaginary impedances.

Dedicated measurements aiming at the observation of space-charge effects were carried out in the synchrotron SIS-18. Transverse Schottky spectra and BTFs were recorded as well as longitudinal Schottky spectra, particle numbers and beam profiles. The beam-intensity dependent deformation of the signals due to space charge was clearly observed.

The space-charge model was fitted to the data. In order to reduce the number of the fit parameters and thus their uncertainty, the momentum spread was determined via longitudinal Schottky measurements. A good agreement with the Schottky data was demonstrated. The BTFs are deformed similarly to the model but deviations were discovered at high beam intensity. The stability diagrams evaluated from the BTF data are clearly shifted by space charge in agreement with the model for the lower side bands. On the upper side the stability diagrams are distorted and less shifted than expected.

The comparison of the fit parameters yields heterogeneous results. Discrepancies

between the Schottky and the BTF data as well as between the upper and the lower side band were found. The deformation of the signals turned out to complicate the analysis of the BTFs. Most importantly the phase converges slowly to its limits so that it becomes difficult to determine its drift and offset. Also spikes in the data from the lower side band limit the use of the time gating procedure to reduce the noise. Finally the incoherent tune shift separates the resonance frequency, where Landau damping occurs, from the maximum of the amplitude, where the noise is the lowest. As a consequence, the interesting part of the stability diagram is formed by a part of the signal with a lower signal-to-noise ratio.

A BTF measurement requires that the beam is in a stationary state after a sufficiently long excitation. It is possible that unconsidered effects, such as the vicinity of a resonance or a real impedance disturbed the beam at high intensity. This can be a reason for the deviations observed in the BTF measurements. The distortion of the momentum distribution with respect to the assumed Gaussian might also contribute. The tails of the momentum distribution become particular important in high-intensity beams because they are emphasized by the deformation of the Schottky spectra and BTFs.

The space-charge parameters calculated from the beam parameters are smaller than the ones indicated by the Schottky and BTF data, particularly for the lower side band. Since the device for the measurement of the beam profiles was in a questionable state, the possible systematic error was estimated with a simple model. The resulting errors do not fully explain the discrepancy. However, it can not be excluded that the estimation does not reproduce the true error. Likely there was discrepancy between the calculated and the actual beta function in the ionization profile monitor, which affects the assessment of the emittance and thus the space-charge parameter.

In future experiments the uncertainty of the results can be reduced by the following improvements: Exchanging the micro channel plates in the ionization profile monitor will provide more reliable beam profiles. A more precise estimation of the emittance can be achieved by a better control of the closed orbit which reduces the uncertainty of the beta function. Recording the beam profile and current synchronously with each Schottky or BTF measurement reduces the impact of the fluctuations of the beam parameters. A more detailed modelling of the actual momentum distribution could further improve the agreement with the model.

Schottky diagnostics was also applied to measure the chromaticity of SIS-18. This parameter needs to be controlled for example in experiments aiming to investigate coherent beam-instabilities. The observed chromaticities do not agree well with the settings, but the measurements helped to find out that one sextupole was polarized wrongly.

A two-dimensional particle tracking code was written and employed to simulate transverse Schottky bands and BTFs with space charge and impedances. The random distribution of a set of particles in phase space gives rise to a fluctuation of the current dipole-moment. The Fourier transform of the dipole moment yields the Schottky spectrum of the beam. The BTF is obtained by exciting the particles with a kick at each time step, where the excitation signal is white noise.

The simulations were carried out for beams with K-V and bi-Gaussian profiles. For both cases a very good agreement with the model was demonstrated up to $\Delta U_{sc} = 2$ and $\Delta U = 2$. No significant difference between the signals of the K-V and the Gaussian beam was found. The stability diagrams are shifted according to the parameters. The Schottky spectra and BTFs affected either by space charge or an imaginary impedance are shifted with respect to each other as expected. The joint simulation of space charge and an impedance yielded shifted Schottky spectra and BTFs without deformation. Thus the simulations fully confirm the analytic model in the regime of moderate space charge.

This work is a first step to the experimental verification of the theory of space-charge affected beams. Despite some discrepancies observed in the experiment, the adequacy of the linear space-charge model is confirmed by the measurements and by the simulations. It is demonstrated that the analysis of Schottky spectra and BTFs of space-charge affected beams is involved with complications. Unless collective effects are studied, measuring Schottky spectra and BTFs at higher frequencies should be considered to avoid complications.

Appendix A

Symbols and abbreviations

Table A.1: List of symbols. Variables subscripted with 0 generally refer either to the nominal value of the physical parameter represented by the variable or to a function excluding collective effects. The superscript $\pm$ labels variables or functions that differ slightly when referred to the upper (+) or lower side (−) band. Δ indicates a shift of the quantity represented by the following parameter. The index j refers to the j^{th} particle in a beam.

Symbol	Explanation
A	mass number of an ion, approximately equal to the number of protons and neutrons in its nucleus
a	rms beam radius or semi axis of an elliptical beam
a_{kv}	full beam radius or semi axis of an elliptical K-V beam
$\hat{\alpha}$	one of the Courant-Snyder parameters
$\vec{B}$	magnetic flux density, $B = \lvert\vec{B}\rvert$
b	radius of a circular beam pipe
β	velocity divided by c
$\hat{\beta}$	amplitude function, one the Courant-Snyder parameters
$\hat{\beta}_{ipm}$	$\hat{\beta}$ at the location of the IPM
$\hat{\beta}_j$	$\hat{\beta}$ in numeric model including error due to momentum deviation Δp_j
C	accelerator circumference
C_I, C_d	auto-correlation function of beam current and current dipole-moment, respectively
c	$= 2.998 \cdot 10^8$ m/s, speed of light in vacuum
d	current dipole-moment of beam in time domain
$\tilde{d}$	$= \mathcal{F}\{d\}$, current dipole-moment in frequency domain
ΔQ_{sc}	incoherent tune shift due to space charge
ΔQ_{sc}^{shape}	tune shift obtained from measured ΔU_{sc}^{shape}, $\sigma_{lon}^{\pm}$ and f_0
ΔQ_{sc}^{shift}	tune shift obtained from measured $f_m^{\pm}$ and Q_{ref}
ΔQ_{sc}^{ϵ}	tune shift estimated from measured beam parameters

$\Delta U^{\pm}$	$= \Delta\omega/\sigma^{\pm}_{m,\omega}$, coherent betatron frequency shift normalized by the width of a side band
$\Delta U^{\pm}_{sc}$	$= \Delta\omega_{sc}/\sigma^{\pm}_{m,\omega}$, incoherent betatron frequency shift due to space charge normalized by the width of a side band
ΔU^{shape}_{sc}	space charge parameter obtained from deformation of measured of Schottky bands or BTFs
ΔU^{shift}_{sc}	space charge parameter obtained from ΔQ^{shift}_{sc}, f_0 and $\sigma^{\pm}_{lon}$
ΔU^{ϵ}_{sc}	space charge parameter obtained from ΔQ^{ϵ}_{sc}, f_0 and $\sigma^{\pm}_{lon}$
$\Delta V^{\pm}$	$= 1/(\tau\sigma^{\pm}_{m,\omega})$, growth rate of a coherent dipolar instability normalized by the width of a side band
Δf_0	deviation of revolution frequency
Δf_{sc}	incoherent shift of f_β due to space charge
Δt	$= \Delta s/v$, time step in simulations
$\Delta\tilde{\omega}$	complex shift of angular betatron frequency due to transverse impedances
Δp	$= (p - p_0)/p_0$, normalized momentum distribution
Δs	step length in simulations
Δx_g	$= l_g/N_g$, grid spacing in simulations
δd	fluctuation of current dipole-moment
δI	fluctuation of beam current
E_0	amplitude of excitation for BTF measurement
E_{btf}	electric field for the simulation of a BTF
E_{imp}	electric field for the simulation of an impedance
E_{kin}	kinetic energy
E_{sc}	electric self-field of a charged particle beam
$\vec{E}$	electric field, $E = \lvert\vec{E}\rvert$
E_p	$= m_p c^2 = 938.3\,\mathrm{MeV}$, energy of a proton at rest
e	$= 1.602 \cdot 10^{-19}\,\mathrm{C}$, elementary charge, charge of proton or electron
$\vec{e}_x$, $\vec{e}_y$, $\vec{e}_z$	orthonormal basis vectors in real space
ϵ	rms emittance
ϵ_0	$= 8.854\,\mathrm{As/Vm}$, electric constant
ϵ_{kv}	full emittance of a K-V beam
$\epsilon^{\pm}$	$= \mp 1 - (\Delta U - \Delta U_{sc} + \mathrm{i}V)\, r_0$, dielectric function
η	$= 1/\gamma_T^2 - 1/\gamma^2$, slip factor
F	force
$\mathcal{F}$, $\mathcal{F}^{-1}$	Fourier transform and its inverse
f	frequency in Hz
$\hat{f}$	$= \mathrm{Re}(r_0)$
f_0	revolution frequency
f_m	$= mf_0$, center frequency of the longitudinal Schottky band at the m^{th} harmonic
$f^{\pm}_m$	frequency of side band next to harmonic m
$f^{\pm}_{m,sc}$	$= f^{\pm}_m \pm \Delta f_{sc}$, frequency of side band including incoherent tune shift
f_β	$= Qf_0$, nominal betatron frequency

$f_{\beta,j}$	$= Q_j f_{0,j}$, betatron frequency of particle j
$f_{\beta,sc}$	$= f_\beta - \Delta f_{sc}$, nominal betatron frequency less incoherent shift due to space charge
$f_{\beta,sc,j}$	$= f_{\beta,j} - \Delta f_{sc}$, betatron frequency of particle j less incoherent shift due to space charge
$\hat{g}$	$= \mathrm{Im}(r_0)$
γ	Lorentz factor
γ_T	transition point of a synchrotron
$\hat{\gamma}$	one of the Courant-Snyder parameters
I	beam current
k	focusing strength of a quadrupole; index on grid
M	transport matrix
$M_{x,x'}$	submatrix of M in horizontal phase space
$M_{j,x,x'}$	$M_{x,x'}$ including momentum deviation Δp_j for beam transport with chromaticity
m	mode number or harmonic in longitudinal Schottky spectrum
m_p	$1.673 \cdot 10^{-27}\,\mathrm{kg}$, proton mass
N_b	number of points within the $2\,\sigma$ width of a simulated Schottky band
N_f	number of exciting frequencies in BTF simulations
N_g	number of grid points in one dimension of the transverse grid in simulations
N_m	number of macro particles in a simulation
N_p	particle number
N_s	number of time steps in a simulation
n	mode number of coherent oscillation modes; index for time steps in simulations
Ω	angular frequency
ω	$= 2\pi f$, angular frequency in rad; analogously with any prefix or subscript
$P_\parallel$	longitudinal Schottky spectrum
$P_{0,\perp}$	transverse Schottky spectrum without collective effects
$P^{\pm}_{0,m}$	Schottky side band next to harmonic m
P_x	simulated horizontal Schottky spectrum
$P_\perp$	transverse Schottky spectrum with collective effects
$P^{\pm}_m$	$= P^{\pm}_{0,m}/\lvert\epsilon^{\pm}\rvert$, Schottky side band next to harmonic m with collective effects
p	momentum
ϕ	phase of betatron oscillation
Ψ	momentum distribution
ψ	betatron phase
R	$= C/2\pi$, mean synchrotron radius
Q	bare tune or working point
$r^{\pm}_{0,m}$	transverse BTF next to m without collective effects
$r^{\pm}_m$	transverse BTF next to m with collective effects
$\vec{r}$	$= (x, x', y, y', z, \Delta p)^T$, phase-space vector describing a position of a particle with respect to the nominal particle
r_0	dispersion integral

r_x	simulated horizontal BTF
ρ	charge density; radius in polar coordinates
$\tilde{\rho}$	Fourier transform of spatial charge density
s	path length of a motion along the nominal orbit
σ	standard deviation of a distribution, also referred to as **r**oot **m**ean **s**quare (rms) width
σ_Q	$= Q\lvert\xi\rvert\sigma_p$, rms chromatic tune spread
$\sigma_{m,f}$	rms width of longitudinal Schottky band at harmonic m in Hz
$\sigma_{m,\omega}$	rms width of longitudinal Schottky band at harmonic m in rad/s
$\sigma^{\pm}_{lon}$	rms width of a side band calculated with the momentum spread determined in a longitudinal measurement in Hz
$\sigma^{\pm}_{m,f}$	rms width of a side band next to harmonic m in Hz
$\sigma^{\pm}_{m,\omega}$	rms width of a side band next to harmonic m in rad/s
σ_p	rms momentum spread normalized by nominal momentum
t	time
τ	growth time of an instability
θ	$= \theta_0 + \omega_0 t$, azimuthal angle
$u^{\pm}$	$= (\Omega - \omega^{\pm}_m)/\sigma^{\pm}_{m,\omega}$, normalized frequency
$u^{\pm}_{sc}$	$= (\Omega - \omega^{\pm}_{m,sc})/\sigma^{\pm}$, frequency including space-charge tune-shift normalized by the width of a side band
v	particle velocity
w_{sim}	$= 4 f_0 Q \xi \sigma_p$, width of simulated Schottky band in Hz
x	horizontal coordinate
x_j	horizontal coordinate of the j^{th} particle in a beam
x'	$= \mathrm{d}x/\,\mathrm{d}s$, slope of horizontal motion with respect to nominal orbit
$\bar{x}$	horizontal position of the beam barycenter
$\dot{x}$	$= \mathrm{d}x/\,\mathrm{d}t$
$\hat{x}_j$	amplitude of betatron oscillation of one particle
$\hat{x}$	amplitude of coherent transverse dipolar beam oscillation
ξ	$= \Delta Q/Q\Delta p$, chromaticity
y	vertical coordinate
y'	$= \mathrm{d}y/\,\mathrm{d}s$, slope of vertical motion with respect to nominal orbit
Z	charge number of an ion, equal to number of protons in nucleus less number electrons in shell
Z_0	$= 377\,\Omega$, impedance of vacuum
Z_m	macro charge applied to scale self-field in simulations
$Z_\perp$	transverse impedance
z	longitudinal coordinate

Table A.2: List of abbreviations.

Abbreviation	Name
ESR	'Experimentier Speicherring'
FAIR	Facility for Antiproton and Ion Research
GSI	'Helmholtzzentrum für Schwerionenforschung GmbH'
IPM	ionization profile monitor
K-V beam	beam with constant transverse particle density
MCP	micro channel plate
SIS-18	'Schwerionensynchrotron 18'

Appendix B

Error estimation

Here the uncertainty of the measured parameters and the those derived from them is estimated. These estimations were employed to calculate the error bars in Fig. 5.6 and Fig. 5.7. The uncertainty of parameters depending on several variables with errors was calculated by the Gaussian sum

$$\delta f(x_1, x_2, \cdots, x_n) = \sqrt{\sum_{i=1}^{n} \left(\frac{\partial f}{\partial x_i} \delta x_i \right)^2}, \tag{B.1}$$

where errors are labelled with δ.

The number of particles fluctuated from injection to injection by about 10 %. Losses of the same order of magnitude during the measuring interval were observed. Therefore the maximal relative error of the particle number is given by

$$\frac{\delta N_p}{N_p} = \frac{\sqrt{2}}{10}. \tag{B.2}$$

The relative variation of the beam size and the uncertainty due to the resolution of the IPM is assumed to be 10 %. The uncertainty of the beam size due to the abrasion of MCPs and space-charge effects was a topic of Sec. 4.3. The MCPs cause a maximal error of 10 % according to Eq. 4.3. The broadening of the beam profile due to space charge is certainly smaller than the maximal deflection estimated in Eq. 4.7, so $\Delta x_{sc}/(2a) = 5\,\%$ is assumed. Taking into account that the latter two errors may only increase the measured value of a, we write

$$\frac{\delta a}{a} \approx \begin{cases} -0.1 \\ +0.15 \end{cases} \tag{B.3}$$

Frequencies can be measured relatively precisely. An accuracy of

$$\frac{\delta f_m^{\pm}}{f_m^{\pm}} = 10^{-4} \tag{B.4}$$

is assumed.

The same applies to δf_m. $\delta f_0 = \delta f_m/m$ is negligible in comparison to all other errors. The deformation parameter can presumably be determined with an uncertainty of

$$\frac{\delta(\Delta\tilde{U})}{\Delta\tilde{U}} = 0.05. \tag{B.5}$$

However, if the momentum distribution is asymmetric the error may become larger.

The momentum spread obtained from the longitudinal and the transverse measurements differs slightly also at low intensity. Furthermore it fluctuated from injection to injection. Therefore a relatively large uncertainty of

$$\frac{\delta\sigma_p}{\sigma_p} = 0.1 \tag{B.6}$$

is assumed.

From Eq. 5.8 it follows

$$\delta Q_{sc}^{shift} = \sqrt{\left(\frac{\delta f_m^{\pm}}{f_0}\right)^2 + \left(\frac{\delta f_m}{f_0}\right)^2} \approx 7.1 \cdot 10^{-3}. \tag{B.7}$$

From Eq. 5.7 it follows

$$\delta Q_{ref} = \sqrt{\frac{1}{N}\sum_{i=1}^{N}[\delta(\Delta Q_{sc}^{shift})]^2} = \frac{\delta Q_{sc}^{shift}}{\sqrt{N}} \approx 2.5 \cdot 10^{-3} \tag{B.8}$$

where the summation extends over the $N = 8$ low intensity measurements serving as reference for Q_f. This error is negligible compared to the others.

From Eq. 5.9 it follows

$$\delta(\Delta Q_{sc}^{shift}) = \sqrt{(\delta Q_{ref})^2 + [\delta(\Delta Q_{sc}^{shift})]^2} \approx \delta Q_{sc}^{shift}. \tag{B.9}$$

From Eq. 5.11 it follows

$$\delta Q_{sc}^{gap} = \sqrt{[\Delta(Q_{sc}^{shift})]^2 + \left(\frac{\sigma_{lon}^{\pm}}{f_0}\delta(\Delta\tilde{U})\right)^2 + \left(\frac{\delta\sigma_{lon}^{\pm}}{f_0}\Delta\tilde{U}\right)^2} \tag{B.10}$$

$$\approx \sqrt{5.1 \cdot 10^{-5} + 5.5 \cdot 10^{-6}(\Delta\tilde{U})^2} \tag{B.11}$$

From Eq. 5.1 it follows

$$\frac{\delta(\Delta Q_{sc}^{\epsilon})}{\Delta Q_{sc}^{\epsilon}} = \sqrt{\left(\frac{\delta N}{N}\right)^2 + \left(\frac{2\delta a}{a}\right)^2} = \left\{ \begin{array}{c} -0.24 \\ +0.33 \end{array} \right\} \tag{B.12}$$

where $\delta\epsilon/\epsilon = 2\delta a/a$ following from Eq. 3.29 was used. So far the error due to the assumption of a circular beam profile was not taken into account yet. It overrates the tune shift by a factor

$$\frac{2\epsilon_y}{\epsilon_y + \sqrt{\epsilon_y\epsilon_x Q_y/Q_x}} \approx 1.05, \tag{B.13}$$

where the tunes of SIS-18 and the measured ratio of the emittances $\epsilon_x \approx 1.4\epsilon_y$ were inserted. As this error has a defined sign it is subtracted from Eq. B.12 to obtain the final uncertainty

$$\frac{\delta(\Delta Q_{sc}^{\epsilon})}{\Delta Q_{sc}^{\epsilon}} \approx 0.29. \tag{B.14}$$

From Eq. 5.12 it follows

$$\delta Q_{sc}^{\epsilon} \approx \delta(\Delta Q_{sc}^{\epsilon}). \tag{B.15}$$

From Eq. 3.56 it follows

$$\frac{\delta\sigma_{lon}^{\pm}}{\sigma_{lon}^{\pm}} \approx \frac{\delta\sigma_p}{\sigma_p}. \tag{B.16}$$

$\delta\xi$ is actually quite large, but with $m = 50$ its contribution to the width is small enough to be neglected.

From $\Delta U_{sc}^{shift} = \Delta Q_{sc}^{shift} f_0/\sigma_{lon}^{\pm}$ it follows

$$\delta(\Delta U_{sc}^{shift}) = \sqrt{\left(\frac{f_0}{\sigma_{lon}^{\pm}}\delta(\Delta Q_{sc}^{shift})\right)^2 + \left(\frac{\delta\sigma_{lon}^{\pm}}{\sigma_{lon}^{\pm}}\Delta U_{sc}^{shift}\right)^2} \tag{B.17}$$

$$\approx \sqrt{0.09 + 0.01(\Delta U_{sc}^{shift})^2}. \tag{B.18}$$

From $\Delta U_{sc}^{\epsilon} = f_0/\sigma_{lon}^{\pm}\Delta Q_{sc}^{\epsilon}$ it follows

$$\frac{\delta(\Delta U_{sc}^{\epsilon})}{\Delta U_{sc}^{\epsilon}} = \sqrt{\left(\frac{\delta(\Delta Q_{sc}^{\epsilon})}{\Delta Q_{sc}^{\epsilon}}\right)^2 + \left(\frac{\delta\sigma_{lon}^{\pm}}{\sigma_{lon}^{\pm}}\right)^2} = 0.31. \tag{B.19}$$

Bibliography

[1] K. Wille. *Physik der Teilchenbeschleuniger und Synchrotronstrahlungsquellen*. Teubner, 1996.

[2] F. Hinterberger. *Physik der Teilchenbeschleuniger und Ionenoptik*. Springer, 1997.

[3] J. D. Cockroft and E. T. S. Walton. Experiments with high velocity positive ions. (I) Further developments in the method of obtaining high velocity positive ions. *Proc. Royal Society A*, 136, 1932.

[4] K. Y. Ng. *Physics of intensity dependent beam instabilities*. Asian Scientific, 2005.

[5] A. W. Chao. *Physics of Collective Beam Instabilities in High Energy Accelerators*. Beam Physics and Accelerator Technology. Wiley, 1993.

[6] H. Wiedemann. *Particle Accelerator Physics, Nonlinear and Higher-Order Beam Dynamics*, volume 2. Springer, 1998.

[7] K. Schindl. Space charge. In *CERN Accelerator School: Basic Course on General Accelerator Physics*, number CERN-PS-99-012-DI. CERN, 1999.

[8] L. J. Laslett, V. K. Neil, and A. M. Sessler. Transverse resistive instabilities of intense coasting beams in particle accelerators. *Review of Scientific Instruments*, 36(4):436–448, 1965.

[9] L. D. Landau. *J. Phys USSR*, 10(25), 1946.

[10] A. Hofmann. Landau damping. In *Proc. of CERN Accelerator School 2003*, number CERN 2006-02, DESY, Zeuthen, 2006.

[11] J. Borer, G. Guignard, A. Hofmann, E. Peschardt, F. Sacherer, and B. Zotter. Information from beam response to longitudinal and transverse excitation. In *Proc. of PAC 1979*, volume NS-26, 3, 1979.

[12] W. Schottky. Über spontane Stromschwankungen in verschiedenen Elektrizitätsleitern. *Annalen der Physik*, 57:541, 1918.

[13] J. Borer, P. Bramham, H. G. Hereward, K. Hübner, W. Schnell, and L. Thorndahl. Non-destructive diagnostics of coasting beams with Schottky noise. Technical Report CERN-ISR-DI-RF-74-23, CERN, 1974.

[14] S. Chattopadhyay. Some fundamental aspects of fluctuations and coherence in charged-particle beams in storage rings. Technical Report CERN 84-11, CERN, 1984.

[15] Uwe Schaaf. *Schottky-Diagnose und BTF-Messungen an gekühlten Strahlen im Schwerionenspeicherring ESR*. PhD thesis, Universität Frankfurt, 1991. GSI-91-22.

[16] K. Beckert, S. Cocher, B. Franzke, and U. Schaaf. The ESR Schottky-diagnosis-system. In *Proc. of EPAC90*, 1990.

[17] N. Angert, W. Bourgeois, H. Emig, B. Franzke, B. Langenbeck, K. D. Leible, T. Odenweller, H. Poth, H. Schulte, P. Spädtke, and B. H. Wolf. The 320-keV ESR-electron cooler. In *Proc. of EPAC90*, 1990.

[18] P. Kienle. Sunshine by cooling. *Naturwissenschaften*, 88(8):313 – 321, 2001.

[19] U. Schaaf, K. Beckert, D. Budicin, H. Eickhoff, B. Franzke, I. Hofmann, G. Kalisch, F. Nolden, P. Spädtke, and M. Steck. Impedances and instability studies at the ESR. In *Proc. of EPAC*, 1992.

[20] I. Hofmann, K. Beckert, S. Cocher, and U. Schaaf. Diagnostics and instability studies of cooled ion beams. In *Proc. of EPAC90*, 1990.

[21] V. Kornilov, O. Boine-Frankenheim, W. Kaufmann, and P. Moritz. Measurements and analysis of the transverse beam transfer function (BTF) at the SIS18 synchrotron. Technical Report GSI-Acc-Note-2006-12-001, GSI, 2006.

[22] P. Moritz, GSI. private communication.

[23] A. Hofmann. Tune shifts from self-fields and images. In *CAS: 5th General Accelerator Physics Course*, number 94-01_v1, Jyväskylä, Finland, 1994.

[24] D. V. Pestrikov. Self-consistent dipole coherent oscillations of a coasting ion beam with strong space charge. *Nucl. Instr. and Methods*, 578(1), 2007.

[25] D. Möhl. On landau damping of dipole modes by non-linear space charge and octupoles. Technical Report CERN/PS 95-08 (DI), CERN, 1995.

[26] V. Kornilov, O. Boine-Frankenheim, and I. Hofmann. Stability of transverse dipole modes in coasting ion beams with nonlinear space charge, octupoles, and chromaticity. *Phys. Rev. ST Accel. Beams*, 11(1):014201, Jan 2008.

[27] M. Blaskiewicz. Transverse stability with nonlinear space charge. *Phys. Rev. ST Accel. Beams*, 4(4):044202, Apr 2001.

[28] D. V. Pestrikov. Dipole coherent oscillations and fluctuations of a coasting ion beam with strong space charge. *Nucl. Instr. and Methods*, 562(1):65 – 75, 2006.

[29] A. Burov and V. Lebedev. Transverse instabilities of coasting beams with space charge. *Phys. Rev. ST Accel. Beams*, 12(3):034201, Mar 2009.

[30] A. W. Chao and M. Tigner. *Handbook of Accelerator Physics and Engineering*. World Scientific, 1998.

[31] K. Y. Ng. Transverse instability at the recycler ring. Technical Report FERMILAB-FN-0760-AD, Fermi National Accelerator Laboratory, June 2004.

[32] P. Kienle and K.-D. Gross. Neue Beschleuniger und Experimentieranlagen bei der Gesellschaft für Schwerionenforschung in Darmstadt. *Naturwissenschaften*, 78(9):385 – 391, 1991.

[33] H. H. Gutbrod, I. Augustin, H. Eickhoff, K.-D. Groß, W. F. Henning, D. Krämer, and G. Walter. FAIR baseline technical report. Technical report, GSI, 2006.

[34] S. Hofmann. Status and prospects of synthesizing superheavy elements. *Eur. Phys. J. A*, 15(1), 2002.

[35] C. Weber et al. Mass measurements in the vicinity of the r p-process and the ν p-process paths with the Penning trap facilities JYFLTRAP and SHIPTRAP. *Phys. Rev. C*, 78, 2008.

[36] B. Franczak. SIS parameter list. Technical report, GSI, 1987.

[37] M. Steck, K. Blasche, W. Bourgeois, B. Franzke, L. Groening, N. S. Dikansky, V. I. Kudelainen V. V. Parkhomchuk, A. I. Sharapa, A. V. Shemyakin, and B. M. Smirnov. Fast beam accumulation by electron cooling in the heavy ion synchrotron SIS. In *Proc. of EPAC96*, 1996.

[38] M. Steck, L. Groening, K. Blasche, B. Franczak, B. Franzke, T. Winkler, and V. V. Parkhomchuk. Beam accumulation with the SIS electron cooler. *Nuclear Instruments and Methods A*, 441(1-2), 2000.

[39] R. Kanungo, C. Nociforo, A. Prochazka, T. Aumann, D. Boutin, D. Cortina-Gil, B. Davids, M. Diakaki, F. Farinon, H. Geissel, R. Gernhäuser, J. Gerl, R. Janik, B. Jonson, B. Kindler, R. Knöbel, R. Krücken, M. Lantz, H. Lenske, Y. Litvinov, B. Lommel, K. Mahata, P. Maierbeck, A. Musumarra, T. Nilsson, T. Otsuka, C. Perro, C. Scheidenberger, B. Sitar, P. Strmen, B. Sun, I. Szarka, I. Tanihata, Y. Utsuno, H. Weick, and M. Winkler. One-neutron removal measurement reveals ^{24}O as a new doubly magic nucleus. *Phys. Rev. Lett.*, 102, 2009.

[40] L. Chen, Yu. A. Litvinov, W. R. Plaß, K. Beckert, P. Beller, F. Bosch, D. Boutin, L. Caceres, R. B. Cakirli, J. J. Carroll, R. F. Casten, R. S. Chakrawarthy, D. M. Cullen, I. J. Cullen, B. Franzke, H. Geissel, J. Gerl, M. Górska, G. A. Jones,

A. Kishada, R. Knöbel, C. Kozhuharov, S. A. Litvinov, Z. Liu, S. Mandal, F. Montes, G. Münzenberg, F. Nolden, T. Ohtsubo, Z. Patyk, Zs. Podolyák, R. Propri, S. Rigby, N. Saito, T. Saito, C. Scheidenberger, M. Shindo, M. Steck, P. Ugorowski, P. M. Walker, S. Williams, H. Weick, M. Winkler, H.-J. Wollersheim, and T. Yamaguchi. Schottky mass measurement of the ^{208}Hg isotope: Implication for the proton-neutron interaction strength around doubly magic ^{208}Pb. *Phys. Rev. Lett.*, 102(12):122503, 2009.

[41] B. Jakob, J. Splinter, M. Durante, and G. Taucher-Scholz. Live cell microscopy analysis of radiation-induced DNA double-strand break motion. *Proc. of the National Academy of Sciences*, 106(9):3172–3177, 2009.

[42] W. Nörtershäuser, D. Tiedemann, M. Žáková, Z. Andjelkovic, K. Blaum, M. L. Bissell, R. Cazan, G. W. F. Drake, Ch. Geppert, M. Kowalska, J. Krämer, A. Krieger, R. Neugart, R. Sánchez, F. Schmidt-Kaler, Z.-C. Yan, D. T. Yordanov, and C. Zimmermann. Nuclear charge radii of ^{7,9,10}Be and the one-neutron halo nucleus ^{11}Be. *Phys. Rev. Lett.*, 102:062503, 2009.

[43] GSI. GSI scientific reports. `http://www.gsi.de/informationen/wti/library/digi.html`.

[44] P. Spiller, K. Blasche, U. Blell, O. Boine-Frankenheim, P. Forck, P. Hülsmann, G. Moritz, H. Ramakers, and S. Ratschow. SIS100/300 Conceptual Design Studies. Technical report, GSI, 2004.

[45] P. Spiller. FAIR at GSI. In *Proc. of HB2006*, 2006.

[46] H. Geissel, H. Weick, M. Winkler, G. Münzenberg, V. Chichkine, M. Yavor, T. Aumann, K. H. Behr, M. Böhmer, A. Brünle, K. Burkard, J. Benlliure, D. Cortina-Gil, L. Chulkov, A. Dael, J. E. Ducret, H. Emling, B. Franczak, J. Friese, B. Gastineau, J. Gerl, R. Gernhäuser, M. Hellström, B. Jonson, J. Kojouharova, R. Kulessa, B. Kindler, N. Kurz, B. Lommel, W. Mittig, G. Moritz, C. Mühle, J. A. Nolen, G. Nyman, P. Roussell-Chomaz, C. Scheidenberger, K. H. Schmidt, G. Schrieder, B. M. Sherrill, H. Simon, K. Sümmerer, N. A. Tahir, V. Vysotsky, H. Wollnik, and A. F. Zeller. The Super-FRS project at GSI. *Nuclear Instruments and Methods B*, 204, 2003.

[47] N. A. Tahir, C. Deutsch, V. E. Fortov, V. Gryaznov, D. H. H. Hoffmann, M. Kulish, I. V. Lomonosov, V. Mintsev, P. Ni, D. Nikolaev, A. R. Piriz, N. Shilkin, P. Spiller, A. Shutov, M. Temporal, V. Ternovoi, S. Udrea, and D. Varentsov. Proposal for the study of thermophysical properties of high-energy-density matter using current and future heavy-ion accelerator facilities at GSI Darmstadt. *Phys. Rev. Lett.*, 95(3):035001, Jul 2005.

[48] J. Ritman. Conceptual design and simulation of the PANDA detector. *Nuclear Instruments and Methods B*, 214, 2004. Low Energy Antiproton Physics (LEAP'03).

[49] W. F. Henning. The future GSI facility. *Nuclear Instruments and Methods B*, 214, 2004. Low Energy Antiproton Physics (LEAP'03).

[50] P. Spiller, GSI. private communication.

[51] P. Huelsmann and W. Vinzenz. The h=2 broadband acceleration RF system for the SIS12/18 upgrade at GSI. Technical Report GSI-Acc-Note-2004-11-001, GSI, 2004.

[52] H. Kollmus, M. C. Bellachioma, M. Bender, A. Krämer, J. Kurdal, and H. Reich-Sprenger. Vacuum issues of SIS18 upgrade at GSI. In *Proc. of EPAC06*, Edinburgh, Scotland, 2006.

[53] C. Omet. *Kollimatorsystem zur Stabilisierung des dynamischen Restgasdruckes im Schwerionensynchrotron SIS18*. PhD thesis, Technische Universität Darmstadt, 2008.

[54] U. Blell, J. Florenkowski, U. Kopf, C. Mühle, M. Petryk, I. Petzenhauser, P. Spiller, A. Batrakov, S. A. Onischenko, and G. E. Ozur. Development of the injection- and extraction systems for the upgrade of SIS18. In *Proc. of PAC07*, Albuquerque, United States of America, 2007.

[55] A. Parfenova. *Linear and nonlinear response matrix and its application to the SIS18 synchrotron*. PhD thesis, Johann Wolfgang Goethe Universität in Frankfurt am Main, 2008.

[56] G. Franchetti, O. Chorniy, I. Hofmann, W. Bayer, F. Becker, P. Forck, T. Giacomini, M. Kirk, T. Mohite, C. Omet, A. Parfenova, and P. Schütt. A proof-of-principle experiment on space charge driven nonlinear resonance trapping in the SIS18 synchrotron. *submitted to Phys. Rev. ST-Accel. Beams*, 2009.

[57] O. Chorniy. *Measurement and interpretation of the bunched beam transfer function in SIS-18 with space charge*. PhD thesis, Technische Universität Darmstadt, 2008.

[58] D. A. Edwards and M. J. Syphers. *An introduction to the physics of high energy accelerators*. Wiley, 1993.

[59] J. Rossbach and P. Schmüser. Basic course on accelerator optics. In S. Turner, editor, *CERN Accelerator School: 5th General Accelerator Physics Course*. CERN, 1994.

[60] E. Wilson. Transverse beam dynamics. In D. Brandt, editor, *CERN Accelerator School - Intermediate accelerator physics*, DESY, Zeuthen, September 2003. CERN.

[61] K. L. Brown, D. C. Carey, C. Iselin, and F. Rothacker. TRANSPORT: A computer program for designing charged particle beam transport systems. Technical Report CERN Report 80-04, CERN, 1980.

[62] M. Reiser. *Design and Theory of Charged Particle Beams*. Beam Physics and Accelerator Technology. Wiley, 1994.

[63] I. M. Kapchinsky and V. V. Vladimirsky. Limitations of proton beam current in a strong focusing linear accelerator associated with strong space charge. In *Proc. of the II. Int. Conf. on High Energy Accel.*, 1959.

[64] I. N. Bronstein, K. A. Semendjajew, G. Musiol, and H. Mühlig. *Taschenbuch der Mathematik*. Verlag Harri Deutsch, 2001.

[65] A. M. Al-Khateeb, R. W. Hasse, O. Boine-Frankenheim, W. M. Daqa, and I. Hofmann. Transverse resistive wall impedances and shielding effectiveness for beam pipes of arbitrary wall thickness. *Phys. Rev. ST Accel. Beams*, 10:064401, June 2007.

[66] U. Blell. Measurement of the kicker coupling impedances in the SIS and ESR at GSI. In *Proc. of PAC 1997*, 1997.

[67] B. Doliwa, H. DeGersem, and T. Weiland. Numerical calculation of coupling impedances for kicker modules. In *Proc. of PAC 2005*, page 1820, Knoxville, Tennessee, 2005.

[68] K. Ohmi and F. Zimmermann. Head-tail instability caused by electron clouds in positron storage rings. *Phys. Rev. Lett.*, 85(18):3821–3824, 2000.

[69] F. Petrov. *Electron clouds in the heavy ion synchrotron SIS-18*. PhD thesis, Technische Universität Darmstadt, in progress.

[70] V. Kornilov, O. Boine-Frankenheim, and I. Hofmann. Collective transverse instabilities in the GSI synchrotrons. In *Proc. of 39th ICFA Advanced Beam Dynamics Workshop HB2006*, pages 131–133, 2006.

[71] V. Kornilov, O. Boine-Frankenheim, and I. Hofmann. Transverse collective instabilities in SIS 100. Technical Report ACC-note-2008-006, GSI, 2008.

[72] N. S. Dikansky and D. V. Pestrikov. *Physics of intense beams and storage rings*. AIP Press, New York, 1994.

[73] Y. L. Klimintovich. *Statistical theory of nonequilibrium processes in plasma*. Moscow University, 1964.

[74] R. E. Shafer. Characteristics of directional coupler beam position monitors. *Transactions on Nuclear Science*, NS-32, 1985.

[75] Tektronix®. *User Manual, RSA3303A & RSA3308A 3 GHz & 8 GHz Real-Time Spectrum Analyzers*. 071-1409-03.

[76] W. Strasser, Tektronix. private communication.

[77] Inc. Wolfram Research. Mathematica®.

[78] F. Caspers, M. Chanel, and U. Oeftiger. A novel method of noise suppression in beam transfer function measurements. In *Proc. of PAC 1993*, 1993.

[79] W. Kaufmann, GSI. private communication.

[80] T. Giacomini, S. Barabin, P. Forck, D. Liakin, and V. Skachkov. Development of residual gas profile monitors at GSI. In *Proc. of Beam Instrumentation Workshop*, Knoxville, United States of America, 2004.

[81] P. Forck, A. Bank, T. Giacomini, and A. Peters. Profile monitors based on residual gas interaction. In *Proc. of DIPAC 2005*, Lyon, France, 2005.

[82] A. Franchi. *Studies and Measurements of Linear Coupling and Nonlinearities in Hadron Circular Accelerators*. PhD thesis, Johann Wolfgang Goethe Universität in Frankfurt am Main, 2006.

[83] T. Giacomini, GSI. private communication.

[84] B. G. Pine, C. M. Warsop, and S. J. Payne. Modelling of diagnostics for space charge studies on the ISIS synchrotron. In *Proc. of EPAC 2006*, Edinburgh, Scotland, 2006.

[85] S. Paret, V. Kornilov, O. Boine-Frankenheim, and T. Weiland. Transverse Schottky noise and beam transfer functions with space charge. In *Proc. of EPAC08*, Genoa, Italy, 2008.

[86] O. Boine-Frankenheim, V. Kornilov, and S. Paret. Measurement and simulation of transverse Schottky noise with space charge. *Phys. Rev. ST Accel. Beams*, 11(7):074202, 2008.

[87] Stefan Paret, Vladimir Kornilov, Oliver Boine-Frankenheim, and Thomas Weiland. Transverse Schottky and beam transfer function measurements in space charge affected coasting ion beams. *Phys. Rev. ST Accel. Beams*, 13(2):022802, 2010.

[88] S. Appel. *Optimization of the injection into SIS-18*. PhD thesis, Technische Universität Darmstadt, in progress.

[89] G. Franchetti, GSI. private communication.

[90] A. Parfenva, G. Franchetti, and S. Sorge. Measurements of β-functions in the SIS18. Technical Report ACC-note-2009-004, GSI, 2009.

[91] S. Paret, V. Kornilov, S. Sorge, and O. Boine-Frankenheim. Chromaticity measurement with electron cooling and Schottky noise. Technical Report ACC-note-2008-008, GSI, 2008.

[92] V. Kornilov and O. Boine-Frankenheim. Transverse coasting beam instability in SIS-18. Technical Report ACC-note-2009-008, GSI, 2009.

[93] B. Stroustrup. *The C++ programming language*. Addison Wesley, 1997.

[94] C. K. Birdsall and A. B. Langdon. *Plasma Physics via Computer Simulation*. Plasma Physics Series. Institute of Physics Publishing, 1991.

[95] W. H. Press, S. A. Teukolsky, W. T. Vetterling, and B. P. Flannery. *Numerical Recipes in C*. Cambridge University Press, 1992.

[96] O. Boine-Frankenheim and V. Kornilov. Implementation and validation of space charge and impedance kicks in the code patric for studies of transverse coherent instabilities in FAIR rings. In *Proc. of ICAP 2006*, 2006.

[97] F. Ruggiero. Single-beam collective effects in the LHC. Technical Report CERN SL/95-09 (AP), CERN, 1995.

Acknowledgement

I thank Prof. Dr. T. Weiland for accepting me as PhD student and giving constructive criticisms on my work. For offering me a position at GSI, wisely supervising my work, giving advice and funding the participation in conferences I thank Prof. Dr. O. Boine-Frankenheim. I am indebted to Dr. V. Kornilov for his cooperation in the experiments, the fruitful discussions and the inspection of my work.

The members of the FAIR accelerator theory group helped me by sharing their knowledge with me where I needed it. By name I wish to thank Dr. S. Sorge, Dr. G. Franchetti, Dr. A. Parfenova, Dr. O. Chorniy and S. Appel. Also people from the FAIR synchrotrons group, in particular Dr. P. Spiller and Dr. J. Stadlmann, provided useful information about the accelerator.

The experiments were supported by various members of the beam diagnostics group. I thank P. Forck, T. Giacomini, Dr. W. Kaufmann and Dr. P. Kowina for providing information about the equipment and fixing technical problems. In this context I also express my gratitude to the former group member P. Moritz. For setting up the synchrotron for the measurements I thank Dr. P. Schütt, Dr. W. Bayer, people from the synchrotrons group and the operators. I acknowledge the support of Dr. M. Steck, Dr. F. Nolden and Dr. C. Dimopoulou during measurements in ESR and for the setup of the electron cooler in SIS-18.

My preceding education enabled me to accomplish this work. Therefore I thank the helpful staff of IKP in the Technische Universität Darmstadt at the time I spent there, including Prof. Dr. A. Richter and his assistants, as well as Dr. M. Hertling, Dr. A. Araz and J. Metz. I thank my family, in particular my parents, and my dear Z. Çay for personal encouragement.

Support in matters of organization and working equipment was given by to me by many staff members of GSI and TEMF not mentioned by name. Naturally I acknowledge also their helpfulness. Generally I thank my colleagues for a good atmosphere at work.

Academic curriculum vitae

Stefan Paret

Born on 30.05.1980 in Darmstadt

Academic education

2000	'Allgemeine Hochschulreife' at the Starkenburg-Gymnasium, Heppenheim; grade: 1.2
2001 – 2006	Enrolled in physics at the Technische Universität Darmstadt
2003 – 2004	Participation in exchange program with the University of Saskatchewan, Saskatoon, Canada
2005 – 2006	Diploma thesis in the institute for nuclear physics, supervised by Prof. Dr. A. Richter: 'Optimierung der Strahlführung in der Extraktion des S-DALINAC'
2006	'Diplom' in physics; grade: *Very good*

Professional experience

2004	Student research assistant at the University of Saskatchewan, Saskatoon, Canada: Simulation of a wiggler spectrum
2004 – 2006	Student research assistant at the Technische Universität Darmstadt: Teaching assistance, supervision of the electron accelerator S-DALINAC
2006 – 2009	Researcher at the GSI Helmholtzzentrum für Schwerionenforschung GmbH: Investigation of transverse dynamics of intense ion beams

Publications and reports

S. Paret, V. Kornilov, O. Boine-Frankenheim, T. Weiland, *Transverse Schottky and BTF measurements in intense ion beams in SIS18*, GSI scientific report 2007, GSI Report 2008-1, 2008

S. Paret, V. Kornilov, S. Sorge and O. Boine-Frankenheim, *Chromaticity measurement with electron cooling and Schottky noise*, Tech. report ACC-note-2008-008, GSI, 2008

S. Paret, V. Kornilov, O. Boine-Frankenheim and T. Weiland, *Transverse Schottky noise and beam transfer functions with space charge*, Proc. of EPAC08, 2008

O. Boine-Frankenheim, V. Kornilov and S. Paret, *Measurement and simulation of transverse Schottky noise with space charge*, Phys. Rev. ST Accel. Beams, 11(7): 074202, 2008

S. Paret, V. Kornilov, O. Boine-Frankenheim and T. Weiland, *Transverse Schottky and beam transfer function measurements in space charge affected coasting ion beams*, Phys. Rev. ST Accel Beams, 13(2): 022802, 2010

Talks

Measurement of transverse collective effects in intense ion beams in the synchrotron SIS18, Seminar 'Physik und Technik von Beschleunigern', Technische Universität Darmstadt, 02.07.2007

Transverse collective effects in intense ion beams in the synchrotron SIS18, Seminar Advances in Electromagnetic Research KWT2007, Riezlern, 22.08.2007

Measurement of transverse Schottky signals and BTF in SIS18, CARE-HHH-APD BEAM'07, CERN-GSI meeting on collective effects, Geneva, 03.10.2007

Noise suppression in transverse beam transfer functions by time gating, 20^{th} Seminar Advances in Electromagnetic Research KWT2008, Riezlern, 14.08.2008

Measurement of transverse space charge effects in intense ion beams, 'DPG Frühjahrstagung', Munich, 11.03.2009

Transverse Schottky spectra and beam transfer functions with space charge, Seminar Advances in Electromagnetic Research KWT2009, Riezlern, 25.08.2009

Erklärung

Gemäß §9 der Promotionsordnung der TU Darmstadt

Ich versichere, dass ich die vorliegende Dissertation selbstständig und nur unter Verwendung der angegebenen Quellen verfasst habe. Die Arbeit hat bisher noch nicht zu Prüfungszwecken gedient.
